Whispering Gallery Mode Optical Resonance and Lasing in Liquid Crystal Microdroplets

A Dissertation submitted to the University of Hyderabad for the award of the degree of

Doctor of Philosophy in Physics

by

Junaid Ahmad Sofi 14phph09



Under the supervision of **Prof. Surajit Dhara**

School of Physics
University of Hyderabad
Hyderabad 500 046, INDIA

June 2020

Declaration

I hereby declare that, this thesis titled Whispering Gallery Mode Optical Resonance and Lasing in Liquid Crystal Microdroplets submitted by me, under the guidance and kind supervision of Prof. Surajit Dhara, is a bonafide research work and is free from plagiarism. I also declare that it has not been submitted previously, in part or in full to this University or any other University or Institution, for the award of any degree or diploma. I hereby agree that my thesis can be deposited in Shodhganga/INFLIBNET.

A report on plagiarism statistics from the University Librarian is enclosed.

Hyderabad

Date: 23/06/2020

(Junaid Ahmad Sofi) Reg. No.:14phph09



Certificate

This is to certify that the thesis titled Whispering Gallery Mode Optical Resonance and Lasing in Liquid Crystal Microdroplets submitted by Junaid Ahmad Sofi bearing registration number 14phph09 in partial fulfilment of the requirements for award of Doctor of Philosophy in the School of Physics is a bonafide work carried out by him under my supervision and guidance.

This thesis is free from plagiarism and has not been submitted previously in part or in full to this or any other University or Institution for award of any degree or diploma.

Further, the student has the following publications before the submission of the thesis for adjudication.

- 1) J. A. Sofi, M. A. Mohiddon, N. Dutta and S. Dhara, Electrical and thermal tuning of quality factor and free spectral range of optical resonance of nematic liquid crystal microdroplets, Physical Review E, 96, (2) 022702, (2017).
- J. A. Sofi and S. Dhara, Stability of liquid crystal microdroplets based optical microresonators, Liquid Crystals, 46, (4) 629-639, (2018).
- J. A. Sofi and S. Dhara, Electrically switchable whispering gallery mode lasing from ferroelectric liquid crystal microdroplets, Applied Physics Letters, 114, (9) 091106, (2019).
- 4) J. A. Sofi, A. Barthakur and S. Dhara, Whispering gallery mode lasing in mesomorphic liquid crystal microdroplets, Soft Matter, 15, 7832-7837, (2019).

Further, the student has passed the following courses towards the fulfillment of coursework requirement for Ph.D:

Course Code	Name	Credits	Pass/Fail
PY801	Advanced Quantum Mechanics	4	Pass
PY803	Advanced Statistical Mechanics	4	Pass
PY804	Advanced Electromagnetic Theory	4	Pass
PY821	Research Methodology	4	Pass

Prof. Surajit Dhara

Thesis Supervisor Professor
School of Physics

University of Whiterabadoo 046, INDIA.
Hyderabadoo 046, INDIA.

Date:

24-06-2020

Prof. Ashok Chatterjee

Dean

School of Physics

University of Hyderabad

DEAN

School of Physics

University of Hyderabad HYDER BAD - 500 040;

"Look up at the stars and not down at your feet. Try to make sense of what you see, and wonder about what makes the universe exist. Be curious."

Stephen Hawking

"There is a perfect brain behind all the natural physical laws."

Albert Einstein

"Indeed, in the creation of the heavens and the earth, and the alternation of the night and the day, there are indeed signs for those of understanding."

Qur'an 3:190

Acknowledgements

To begin with, I would like to express my heartfelt gratitude to my research advisor Professor Surajit Dhara for the patient guidance, time to time encouragement, fruitful advices and all the support that he has provided to me during the course of my entire PhD programme. I would like to acknowledge him for investing his precious time with me in all the scientific discussions and ideas during my research work. I enjoyed to the maximum his objective criticism and scientific freedom that helped me to develop my own ideas and methods. I pay my high respect and regards to his dedication towards scientific research.

Special and sincere thanks to my doctoral committee members, Prof. B.V.R Tata, Prof. S. Srinath and Dr. G. Venkataiah for their valuable suggestions from time to time.

I would like to thank Prof. I. Musevic and their group from University Of Ljubljana and Josef Stefan Institute for their contribution in the collaborative research work.

I am very grateful to Prof. Nirmalkumar Viswanathan and Prof. Ashok Vudayagiri for all the scientific discussions and the instrumental support that I received from their respective laboratories.

I would like to express my heartfelt thanks to Prof. Anantha Lalshmi P. and Prof. Suneel Singh for all the cheerful chats and encouragement that made my working days enjoyable in the school.

I am indebted to all my coworkers, both seniors and juniors, for their pleasant company and positive contribution in maintaining the scientific charm and the cordial atmosphere of our laboratory.

I pay my sincere thanks to all the budding research scholars in the SoP and the ACRHEM for all the healthy scientific discussions and also for helping me in troubleshooting some of my experimental problems.

I thank former Deans, Prof. R. Singh, Prof. Bindu A. Bamba, Dean V. Seshu Bai and present Dean Prof. Ashok Chatterjee for providing the needful facilities in the school. Furthermore, I am grateful to all the other faculties and school staff for their small but important assistance during the course of my PhD duration.

I also thank UGC-BSR for awarding me the JRF and SRF fellowships.

Last but not the least, many thanks to my friends and critics for their all sorts of admiration, criticism and inspiration.

Most importantly, I would like to sincerely thank my parents and my siblings for their never ending selfless support and countless blessings. I took immense inspiration from the life ideals of my late Dad. His honesty, never say die attitude and hard work have always been greatly inspirational to me. I dedicate my PhD dissertation to my beloved parents.

Abstract

Whispering gallery mode resonance phenomenon derives its roots from the famous experiment on acoustic waves by Lord Rayleigh at Saint Paul's Cathedral Church, London in 1878. Over the years, similar phenomenon has been demonstrated in the case of electromagnetic waves for spherical microcavities. In spherical microcavities, the light ray meets in phase upon a complete revolution, as a result of which, the optical resonance takes place which is known as whispering gallery mode (WGM) optical resonance. Ever since the electronic integrated chip came into existence and its applications became wide reaching, the scientists in general and the physicists in particular have initiated huge efforts in emulating the similar idea in the form of an optic chip. Such an optical chip is supposed to incorporate optical micro-components in the form of microlasers, microfilters, microsensors, etc. all of which primarily rely on the optical microcavitiy. Small size, easy manufacturing, real time detection and tunability are some of the crucial features that the scientists are looking for. Despite the fact that the solid resonators possess the highest Q-factor and thus low optical energy loss, these microresonators lack the tunability of the whispering gallery modes. In this thesis, we study some of the promising aspects of the liquid crystal based optical microcavities that could well fit into some of the typical requirements for the future generation optical chip. Various methods like thermal itching, top-down approach, etc have been used to fabricate such optical microcavities in the past. The underlying principle behind such optical microcavities is that they resonantly couple light into small volumes. The resonant modes that are supported by these optical microcavities are basically dependent on the size and the morphology of the microcavity. Any alteration of the size or morphology of the microcavities by means of any external stimuli like electric and magnetic fields, temperature, etc. results in the subsequent changes in the resonant modes, paving the way for optical sensing application. In addition, these microcavities act as high quality factor resonators. When an active material is added to the microcavity, the optical pumping and the subsequent feedback provided by the cavity walls supersedes the cavity losses and gives rise to the whispering gallery mode lasing. Inspired by the solid state based optical microcavities, we tried to emulate the similar ideas on liquid crystal based spherical microdroplets suspended in appropriate medium. The main aim of this thesis is to explore the liquid crystal (LC) microdoplets as promising optical microcavities for soft photonic chip applications. Owing to the basic requirement for the miniaturized micro optical components in a soft photonic chip, we aim to demonstrate the compatibility of the LC spherical microcavities as the prospective contenders for the optical micro components. From the basic and fundamental scientific perspectives, the microdroplet structure of various liquid crystalline materials is of great interest for exploration. Through different externally applied stimuli on the LC based microdroplets, we try to showcase the possible versatile usage of these tiny optical microcavities in sensing and lasing. To begin with, the electrical and thermal tuning of the whispering gallery mode optical resonance in LC microdroplets is studied. Next we try to overcome the challenges faced in the first goal with special attention to the stability and longevity of the LC microdroplets in different media. Once the stable dispersion of the LC microdoplet system is achieved, we study their lasing properties. With special emphasis on switchability feature, the FLC based optical microcavities are studied for demonstrating switchable microlasers. Lastly, owing to the vast existence of liquid crystal mesophases with varying structures, we study the lasing properties from different mesophases.

This PhD dissertation contains a total of seven chapters including introduction and summary.

The first chapter discusses about the concept of whispering gallery resonance and an introduction to the liquid crystalline materials. In the beginning, the general description of the various liquid crystalline phases that have been used in this thesis are explained. The most common types of the liquid crystal microdroplets are discussed. Next, a historical account of the whispering gallery resonance followed by the merits and demerits of the solid and liquid state based optical microcavities are discussed. Subsequently, the potential use of liquid crystal based optical microcavities in lieu of their interesting physical properties as soft photonic components alongside some important properties of the optical resonators are discussed. Towards the end of the chapter, brief theoretical background of whispering gallery mode optical resonance in case of isotropic and anisotropic spherical optical microresonators is discussed. Finally, we talk about the theory of lasing.

The second chapter deals with the experimental techniques that have been employed for performing the optical resonance oriented experiments on the liquid crystal based microdroplets. To begin with, different types of cells are discussed alongside their fabrication and usage. All the processes involving cell preparation, dye doping of the liquid crystal compound, sample preparation, optical polarizing microscopy analysis and optimization of laser optics and laser energy are discussed in detail.

In the third chapter, we present the experimental findings on the electrical and the thermal tuning of quality factor and free spectral range of whispering gallery mode optical resonance in the spherical liquid crystal microdroplets, suspended in polydimethyl silohexanne polymer (PDMS). We started with 5CB liquid crystal compound and formed radial microdroplets in PDMS. The LC molecules are radially anchored in the microdroplet as confirmed by the optical micrograph analysis. Prior to the microdroplet formation, the LC compound was mixed with an optimized amount of fluorescent dye

(DCM). In order to couple light within the microdroplet, an isolated microdroplet was illuminated with a tightly focused laser beam of wavelength 532nm from a continuous wave laser. The laser light lies in the absorption band of the doped dye. Some part of this fluorescence light gets trapped within the microdroplet and thus whispering gallery modes are excited. To explore and demonstrate the fine controlled electrical and thermal tuning of the whispering gallery mode optical resonance, separate experiments are conducted wherein the external electric field and temperature controller is applied to the microdroplet dispersion. Since the LC compound chosen for this work is thermotropic and possesses dielectric anisotropy, thermal and electrical tuning of the quality factor and the free spectral range of the WGM optical resonance are investigated. The effect of the LC microdroplet size reduction on the optical resonance properties is highlighted and accordingly the need for the suitable dispersing medium is discussed.

In the fourth chapter, we investigate several dispersing media for stable nematic LC microdroplets' formation. Special attention is paid towards the radial anchoring of the nematic LCs and the considerable longevity of the microdroplets in the dispersing media. Further, the size stability aspect is studied with respect to both the time and temperature variations. In this chapter, we tried PDMS, Glycerol-Lecithin mixture and Cytop as the supporting media for the LC microdroplets. We used a positive and negative dielectric anisotropy liquid crystals, namely 5CB and MLC-6608, both of which exhibit the nematic phase at room temperature for the microdorplet composition. The size and the texture of the microdroplets suspended in respective surrounding mediums are studied with respect to the time. This time based size study of microdroplets brings out important merits and demerits of different polymers/mixtures used in this work. We observe that the Cytop mixture is found to be one of the most stable dispersing mediums for LC microdroplets due to the greater longevity of the LC microdroplets and also due to its optically lesser lossy character as compared to the PDMS and the Glycerol-Lecithin mixtures. Further, using WGM approximation theory for smaller microdroplets, we labeled TM modes from the WGM spectrum of a small MLC-6608 microdroplet. Once the stable LC microdroplet-polymer system is attained, next, the free spectral range (FSR) of the various sized microdroplets is studied. Towards the end of this chapter, we finally discuss the effect of electric field on the free spectral range and Q-factor of the WGM optical resonance of a negative dielectric anisotropy liquid crystal (MLC-6608) microdroplet.

The fifth chapter sheds light on the comparative lasing studies in the mesomorphic liquid crystal microdroplets. Despite known rich and diverse structures of the liquid crystals, no comparative study has been reported so far with an aim to bring out the relative merits of lasing in the mesomorphic microdroplets. As a part of an effort to figure out the better optical microcavity for WGM lasing from a vast number of known LC

mesophases, this chapter is aimed at exploring and comparing the commonly available LC mesophases viz, Nematic (N), Smectic A (Sm A) and Smectic C (Sm C) of a pyridine derivative LC compound. In this chapter, we discuss the experimental results obtained on the morphology and the WGM lasing of N, SmA and SmC microdroplets dispersed in Cytop solution. The mesomorphic microdroplets are obtained by varying the temperature. From the physical texture analysis, we observe that all the microdorplets exhibit radial director configuration. As far as the mechanical stability is concerned, the SmA microdroplets are found to be highly stable and robust against the mild mechanical stress as compared to the N and the SmC microdroplets. Next, we move on to the WGM lasing study in these mesophases. For many excited WGMs, we observe the occurrence of typical lasing curve between out put intensity and linewidth with respect to the in put pumping energy of the laser beam. Such curves are indicative of attainment of population inversion in dye molecules and hence the onset of stimulated emission. Comparatively, we study lasing properties such as intensity, threshold pump energy and the linewidth of the excited WGMs from the three mesomorphic microdroplets and show that overall SmA microdroplets are superior than N and SmC microdroplets from WGM lasing perspective. In fact, for comparable size mesomorphic microdroplets, it is observed that the output intensity of lasing at fixed pumping energy in SmA phase is five times larger than that in the N and the SmC microdroplets. The experimental results are discussed based on the orientation dipole moment of the dye molecules, director fluctuations and tilting of the director at the interface.

The sixth chapter reports on the experimental studies on the electrically switchable lasing from a room temperature ferroelectric liquid crystal microdroplets. Here, we discuss on the whispering gallery mode lasing from dye-doped ferroelectric liquid crystal microdroplets suspended in a low refractive index and highly transparent perfluoropolymer at ambient temperature. Taking the results from Chapter 1 and Chapter 2 into the due consideration, here we used Cytop as a surrounding medium owing to its greater stability for micrdroplet dispersion. Nile red dye is chosen for fluorescent coupling due to its lower bleaching property than DCM dye. The FLC microdroplets are excited with the help of a pulsed laser beam of 532nm wavelength, which falls in the absorption band of the doped Nile red dye. As the pumping energy is increased, the dye doped microdroplet start to emit multimode laser light beyond certain input energy threshold values. It is observed that, for most of the modes, the emitted intensity starts increasing while the linewidth starts decreasing rapidly after specific pumping energies. The change in slope occurs at the threshold input energy of the beam suggests that the dye molecules acquire population inversion within the microdroplet and marks the onset of the stimulated emission. We show that the lasing threshold pump energy of ferroelectric microdroplets is much smaller than that of the nematic and cholesteric microdroplets.

Towards the end of the chapter, we demonstrate that with increasing electric field, the linewidth increases while the lasing intensity decreases and eventually switches off beyond a particular field. We show that the ferroelectric liquid crystal based WGM lasing could be switched on and off via applied electric field.

The seventh chapter summarizes all the findings of my PhD research work. We put forward future directions of liquid crystal and other soft materials' based photonic research. Further, with huge diversity in LC mesophases and other soft materials, we anticipate interesting lasing and sensing results in different LC mesophase microcavities. Apart from LCs, we also propose the idea of potential photonic application possibilities from biological materials.

Contents

D	eclar	ation	į
C	ertifi	cate	,
A	ckno	wledgments	_
\mathbf{A}	bstra	.ct xi	i
Li	st of	Figures xxi	i
Li	\mathbf{st} of	Abbreviations xxvii	i
Li	st of	Symbols xxix	_
1	Intr	oduction and theoretical background	L
	1.1	Liquid Crystals	L
		1.1.1 Nematic phase	3
		1.1.2 Smectic phase	
		1.1.3 Ferroelectric liquid crystals	l
	1.2	Physical properties of liquid crystals	5
		1.2.1 Refractive index	5
		1.2.2 Dielectric anisotropy	;
		1.2.3 Freedericksz transition	7
	1.3	Liquid crystal microdroplets	7
	1.4	Optical resonators and historical background	3
	1.5	Liquid crystal based optical microresonators)
		1.5.1 Quality factor (Q-factor)	L
		1.5.2 Free spectral range)
		1.5.3 Mode volume	3
	1.6	Whispering gallery mode theory for an isotropic microsphere 13	3
	1.7	Approximate solutions	3
	1.8	Whispering gallery modes in anisotropic microsphere)
	1.0	Theory of lasing	١

Contents xviii

2	\mathbf{Ma}	terials and methods	29
	2.1	Introduction to the chapter	. 29
	2.2	Types of cells and their preparation	. 29
		2.2.1 Cell for studying liquid crystal texture	. 30
		2.2.2 Cell for studying temperature related WGM experiments	. 32
		2.2.3 Electro-optic cells	. 32
		2.2.3.1 Cell with in-plane electrodes	
		2.2.3.2 Cell with parallel plate electrodes	. 33
	2.3	Materials used	. 34
		2.3.1 Liquid crystals	. 34
		2.3.2 Fluorescent dyes	
		2.3.3 Polymers and solutions	
	2.4	Polymer dispersed liquid crystals preparation (PDLC)	
		2.4.1 Phase separation method	
		2.4.1.1 Polymerization induced phase separation (PIPS):	
		2.4.1.2 Thermally induced phase separation (TIPS):	
		2.4.1.3 Solvent-induced phase separation (SIPS):	
		2.4.2 Emulsion method:	
	2.5	Microscopic observation of the PDLC	
	2.0	2.5.1 Optical polarizing microscopy (OPM)	
		2.5.2 Lambda plate imaging	
	2.6	Optical set-up	
	2.7	Polarization set-up and analysis of WGM polarization	
		ctrical and thermal tuning of quality factor and free spectral range optical resonance of nematic liquid crystal microdroplets Introduction	51 . 51 . 52 . 53
4	Sta	bility of liquid crystal based optical microresonators	65
	4.1	Introduction	
	4.2	Experimental	
	4.3	Results and discussion	
	4.4	Conclusion	. 76
5	Wh	nispering gallery mode lasing in mesomorphic liquid crystal micro)-
		plets	7 9
	5.1	Introduction	. 79
	5.2	Experimental	. 80
	5.3	Results and discussion	
	5.4	Conclusion	
c	15/1		
6		ctrically switchable whispering gallery mode lasing from ferroelec : liquid crystal microdroplets	;- 91
	6.1	Introduction	
	6.2	Experimental	
	0.4	- mpointonout	. 02

Contents	xi

	6.3 6.4		s and discussion	
7	Su	mmary	and outlook	103
	7.1	Aim a	nd overview of thesis	103
	7.2	Future	e outlook	105
		7.2.1	Fabrication of micro biolasers	105
		7.2.2	Unknown promise of mesomorphic liquid crystal phases	105
		7.2.3	Diversifying optical microcavity structure	105
Bi	ibliog	graphy		111

List of Figures

1.1	phase and, (c) Isotropic phase	1
1.2	Schematic diagram showing different shape liquid crystal mesogens. (a)	
	Rod-like molecule, (b) Disc-shaped molecule, and (c) Bent core molecule.	2
1.3	Schematic diagram showing nematic phase liquid crystal. Red rods indicate calamitic molecules. Blue arrow represents the director \hat{n}	3
1.4	Schematic diagram showing Smectic-A phase. Red rods indicate calamitic molecules. The blue and red lines indicate the director \hat{n} and the layer	
1.5	normal \hat{z}	4
	molecules. θ is the angle subtended by the director with the layer normal.	4
1.6	The helicoidal structure of ferroelectric liquid crystal. The spontaneous polarisation (\hat{p}) in each layer is always perpendicular to the director \hat{n} and tangential to the circle of intersection of the cone with the boundary plane of the layer. (a) Orientation of the molecule around a cone with respect to the axis of a right cone. (b) Orientation of spontaneous polarization in each layer of the FLC. The red, blue and green lines represent the cone axis, director and the spontaneous polarization direction of the molecules respectively	5
1.7	Types of liquid crystal microdroplets: (a) Radial microdroplet under crossed polarizers. (b) Radial microdroplet without crossed polarizers. (c) Schematic diagram of a radial droplet. (d) Bipolar microdroplet under crossed polarizers. (e) Bipolar droplet without crossed polarizers. (f) Schematic diagram of bipolar droplet. Black dot at the centre of the radial microdroplet and two small black dots at diamterically opposite side	
1.8	of the bipolar droplet represent defects	7
	pering gallery. The yellow and red arrows indicate the paths of an acoustic	
1.9	wave and an optical wave respectively. Different types of optical microresonators: (a) Microbottle, (b) Microsphere, (c) Fabry-Perot, (d) Microring, (e) Microtoroid and (f) Microdisk.	
	Red curves indicate optical resonances in the respective microresonators.	
	This image is adapted from Ref. [29]	9
1.10	(a) Schematic diagram showing the WGM optical resonance of a spherical	
	microresonator using ray and wave optics. n_1 and n_2 are the refractive	
	indices of the respective media. (b) Small ellipsoids represent the electric	
	/ -	11
1.11	Spherical coordinate system: Red wavy loop depicts an arbitrary WGM	1.6
	wave propagating along the circumference of the equatorial plane	16

List of Figures xxii

1.12	Schematic diagram showing the electric field oscillation in radial nematic liquid crystal microdroplet for (a) TE modes, (b) TM modes. (c) The green ellipsoid indicates the uniaxial dielectric tensor of the liquid crystal.	19
1.13	(a) Designation of WGMs for a $10.6\mu \text{m}$ LC microdroplet. The angular mode number l for radial number $q = 1$, varies from 71 to 89	20
1.14	Schematic diagram of a conventional laser. Thick green arrow indicates the transmitted laser beam	21
2.1	Schematic diagram of a typical liquid crystal cell used in optical texture study. (a) Top view, and (b) Side view	31
2.2	Schematic diagram of a thermo-optic cell used for temperature based experiments. (a) Top view of the cell, and (b) Side view of the cell	32
2.3 2.4	Schematics of an in-plane field cell. (a) Top view, and (b) Side view Schematic diagram of an out of plane field cell. (a) Top view, and (b)	33
2.5	Side view	33 35
2.6 2.7	crystal compound	35
2.1	blue and red curves represent absorption and emission spectra of the two dyes respectively	36
2.8	Chemical structure of (a) Polydimethylsiloxane and, (b) Cytop	37
2.9	Chemical structure of lecithin. The fatty acids are indicated by R_1 and R_2 .	38
2.10	Droplet making through micropipette injection	41
2.11	Effect of the retardation plate on the polarized white light passing through it.(a) When no sample is placed in the optical path. (b,c) When the sample is added in the optical path with the ellipsoidal wave front parallel	
2.12	and perpendicular to the retardation plate respectively	42
	plate. Red arrow shows the fast axis of the retardation plate	43
	Schematic diagram of the experimental set up used in the laboratory	44
2.14	Experimental set up used for the whispering gallery optical resonance experiments. The red captions label the essential instruments of the set	45
0.15	up	45
	Laser output energy characteristics of the used pulsed laser as a function of frequency	46
2.16	Experimental set up for polarization identification of WGMs: (a) Actual location for the light coupling in the experimental set up. (b) Schematic diagram of rotator analyzer, and (c) Schematic diagram showing the role of light coupler (analyzer) for WGMs transmission from microscope into the spectrometer. Thick red and green arrows depict different polarization	
	light.	47

List of Figures xxiii

2.17	Polarization characterization of WGMs observed from a nematic droplet of 20.2 μ m at room temperature. WGMs observed when (a) The laser polarization and analyzer axis are parallel to eachother but perpendicular to the droplet surface. (b) The laser polarization is made perpendicular to the analyzer axis in (a) configuration. (c) The analyzer axis is made perpendicular to the laser polarization of (a) configuration, and (d) Both the laser polarization and the analyzer axis are made parallel to each other and tangential to the droplet surface	47
3.1	Schematic diagram of the scanning near-field optical microscope (SNOM) setup	52
3.2	Polarising optical micrograph showing suspended microdroplets of 5CB liquid crystal in PDMS at room temperature	53
3.3	(a) Polarising optical micrograph of a 5CB microdroplet. (b) Schematic diagram showing the molecular orientation inside the microdroplet. Small ellipsoids represent the molecules of the 5CB liquid crytsal compound while the dot at the centre of the sphere show the central point defect. (c) A DCM dye doped microdroplet illuminated by a focused laser beam	
3.4	$(\lambda=\!532\mathrm{nm}).$ The red arrow indicates the irradiation point (a) Representative WGM spectra recorded at two different temperatures namely, at 27.5°C (Black) and 30.5°C (Red). (b) Variation of Q -factor with temperature for the mode with the highest intensity. The continuous	54
3.5	line is the best fit to Eqn.(3.5). Droplet diameter: 9μ m Schematic diagram showing the director field and resonance modes in a microdroplet at (a) zero, (b) small, and (c) large electric fields. The blue,	55
3.6	yellow ellipsoids and red lines represents modes and director respectively. (a) WGM resonance spectra at two different voltages $0.35~V$ (Black) and $6.19~V$ (Red). (b) Variation of Q -factor with the applied voltage for the highest intensity mode. The continuous line is a guide to the eye. Droplet	57
3.7	diameter: $8 \mu \text{m}$	58
	the best fit (linear) with a slope 0.17nm/V. (b) Variation of the FSR with temperature	60
3.8	(a) Variation of diameters of the microdroplets with respect to (a) time and (b) temperature. The lines in (a) are the linear best fits. The slope of the smaller droplet $(33.5\mu\text{m})$ is 9nm/min . The dotted lines in (b) shows	
	the deviation from the linear variation	61
4.1	Variation of diameter of 5CB microdroplets with time, dispersed in (a) PDMS (b) glycerol (90%) lecithin (10%) mixture. The continuous red line in (a) is a best fit to the equation; $D(t) = D(0) + Ae^{-t/\tau}$. Continuous lines in (b) are linear best fits. The measurements are made directly from the optical microscope at room temperature. Polarising optical microscope	67
4.2	images of microdroplets with defects (Inset)	67
	microdroplets are highly stable and used for optical resonance studies	69

List of Figures xxiv

4.3	Variation of diameter of two MLC-6608 microdroplets, $15.14\mu m$ and $18.84\mu m$ with temperature in Cytop	70
4.4	(a) Optical polarising micrograph of an MLC-6608 micro-droplet dispersed in Cytop at room temperature. (b) Droplet as seen without polarisers. (c) A Nile-Red dye-doped LC microdroplet illuminated by a focused 514 nm laser beam. The irradiation point is marked by green ar-	10
	row. (d) Optical resonance spectrum recorded by the spectrometer from an illuminated LC microdroplet with calculated TM modes	71
4.5	(a) Time dependence of FSR of different size LC microdroplets dispersed in Cytop. (b) Variation of FSR with microdroplet size. The red line is the best fit to FSR $\propto 1/D$. The error bar in (a) is almost equal to the	
	point size. All the measurements are made at room temperature	72
4.6	Optical polarising micrographs of elastic distortion in an LC microdroplet at (a) zero electric field (b-c) increasing electric field. Corresponding λ -plate images are shown underneath. (d) Representative WGM spectra of an LC microdroplet below $(0.12\ V/\mu m)$ and above $(0.56\ V/\mu m)$ Freedericksz threshold field. The direction of electric field and the orientation of the slow axis of the λ -plate with respect to the crossed polarisers is shown	
	on the left side	73
4.7	(a) Variation of Q-factor $(\lambda/\Delta\lambda)$ of a few TM modes with applied electric field of an MLC-6608 microdroplet with diameter $10.7\mu m$ using a grating of 300 lines/mm (b) Variation of FSR with applied electric field of a few	
4.8	TM modes. Vertically dotted line represent the Freedericksz threshold field. Optical resonance spectrum recorded by the spectrometer using a high resolution grating of 2400 lines/mm in the absence of external applied	74
4.9	electric field. Droplet diameter $10.6\mu m$	7575
5.1	(a-c) Polarizing optical micrographs (POM) of a microdroplet of diameter $14.5\mu m$ in the N, SmA and SmC phases. λ -plate images of the respective microdroplets are shown underneath. Temperatures of the microdroplets are shown on the λ -plate images. Crossed polarisers and λ -plate orientation are shown on the left side. (d-f) Schematic director profiles in N, SmA and SmC microdroplets. Yellow ellipsoids represent Nile red dye molecules (doped)	81
5.2	(a) Temperature dependent tilt angle (θ) measured from the texture of a SmC microdroplet of diameter 33 μ m. (b) Temperature dependent bire-	
- 0	fringence (Δn) measured in a planar cell	82
5.3	A typical WGM spectra at a pumping energy of 20 nJ (below the lasing threshold) from a SmA microdroplet of diameter $10\mu m$	82
5.4	(a-c) Fluorescence images of illuminated edges of N, SmA and SmC microdroplets with pump energy of 115 nJ. Insets of images (a), (b) and (c) show the respective emission patterns of the whole microdroplets. The N, SmA and SmC microdroplet diameters are 21, 22 and 22.4 μ m respectively. (d-f) Emission spectrum from the respective microdroplets. White	
	arrows indicate the excitation edges of the microdroplets	83

List of Figures xxv

5.5	(a,c,e) Variation of output intensity and (b,d,f) corresponding linewidths as a function of pumping energy. The wavelengths of selected highest intensity modes are 616.4nm, 629.8nm and 629.2nm for the N, SmA and SmC microdroplets respectively. N, SmA and SmC microdroplets' diameters are 21, 22 and 22.4 μ m respectively. Threshold pump energies are marked by arrows. Dotted lines are drawn as guide to the eyes	84
5.6	Variation of lasing intensity of the mode corresponding to emission line $\lambda = 629.2$ nm with tilt angle θ in the SmC phase for a pumping energy of 224 nJ. Dotted line is drawn as a guide to the eye	85
5.7	(a) Dependence of lasing threshold pump energy on microdroplets diameter. Dotted lines are drawn as guide to the eye. (b) Fluorescence intensity measured from a thin film of sample confined between two glass plates at different temperatures. The bandwidth of the excitation filter is 510-560nm. Small oscillations overlaying the emission are due to the finite thickness of the cell	86
6.1	(a) Schematic diagram of the cell made of two indium-tin-oxide (ITO) coated glass plates. Textures of FLC microdroplets of different diameters. (b-g) Images in the top row show polarising optical micrographs of droplets while the bottom row shows images taken using an additional λ -plate. The orientation of the slow axis of the λ -plate with respect to the crossed polarisers is shown on the left side. (h) Schematic diagram of the cross section of a smaller droplet showing concentric smectic layers	
6.2	with radial helical axis. The red ellipsoids represent molecules within the cone rotating along the helical axis	93
6.3	the two illuminated microdroplets	94
6.4	diameter, $D=23.8 \mu\text{m}$	96 97
6.5	underneath. The field direction is out of the plane	91
	strength. The dotted line is drawn as a guide to the eyes	97

List of Abbreviations

5CB 4-pentyl-4'-biphenylcarbonitrile

8CB 4-octyl-4-biphenylcarbonitrile

a.u. arbitary unitsCr crystalline phased cell thickness

 ${f D}$ diameter

DCM 4-(dicyanomethylene)-2-methyl-6-(4- dimethylaminostyryl)-4H-pyran

FLC ferroelectric liquid crystal phase

FP Fabry-Perot

FSR free spectral range

FWHM full width half-maximum

I isotropic phaseITO indium tin oxide

LASER light amplification by stimulated emission of radiation

LC liquid crystals

MDR morphology dependent resonance

 ${f N}$ nematic phase

NA numerical aperture

Nd:YAG neodymium-doped yttrium aluminium garnet

NI nematic-isotropic phase transitionOPM optical polarizing microscopyPDLC polymer dispersed liquid crystal

PDMS polydimethylsiloxane

PIPS polymerization induced phase separation

Q-factor quality factor

SIPS solvent-induced phase separation

SmA smectic-A phaseSmC smectic-C phaseTE transverse electric

TIPS thermally induced phase separation

Abbreviations xxviii

TM transverse magnetic

UV ultraviolet

WD working distance

 \mathbf{WGM} whispering gallery modes

List of Symbols

a, r, Rradius optical absorption decay constant of the material α_{mat} Einstein's coefficient for spontaneous emission A_{21} B_{12} Einstein's coefficient for photon absorption B_{21} Einstein's coefficient for photon induced emission \hat{n} liquid crystal director Sscalar order parameter refractive index nextraordinary refractive index n_e ordinary refractive index n_o n_{\parallel} refractive index parallel to the \hat{n} refractive index perpendicular to the \hat{n} n_{\perp} effective refractive index of resonator n_{eff} refractive index of resonator n_r average refractive index \bar{n} refractive index of surrounding n_s birefringence $\Delta n = n_e - n_o$ dielectric constant parallel to the \hat{n} ϵ_{\parallel} dielectric constant perpendicular to the \hat{n} ϵ_{\perp} dielectric anisotropy $\Delta\epsilon=\epsilon_{\parallel}$ - ϵ_{\perp} vacuum permittivity K_{11}, K_{22}, K_{33} splay, twist and bend elastic constants Kaverage elastic constant Boltzmann constant k_B λ wavelength λ_0, λ_r resonant wavelength $\Delta \lambda$ or $\delta \lambda$ full width half-maximum $\delta \lambda_{SM}$ free spectral range τ time

Symbols xxx

θ	tilt angle
T_{NI}	nematic-isotropic phase transition temperature
p	pitch
\hat{p}	spontaneous polarisation
V	voltage
V_{th}	Freedericksz threshold voltage
ω	angular frequency
\hat{z}	layer normal

Dedicated to my beloved parents

Chapter 1

Introduction and theoretical background

1.1 Liquid Crystals

Liquid crystalline state is a state of matter which is intermediate between the crystalline state and the isotropic liquids. Such a class of material can flow like liquids and in addition, its molecules can order just like solids [1]. Figure 1.1(a), 1.1(b) and 1.1(c) shows a schematic diagram of crystalline phase, liquid crystal phase and an isotropic phase respectively with the constituent molecule in the shape of a rod. Liquid crystal (LC) materials possess both viscosity and birefringence properties. Based on the mode of

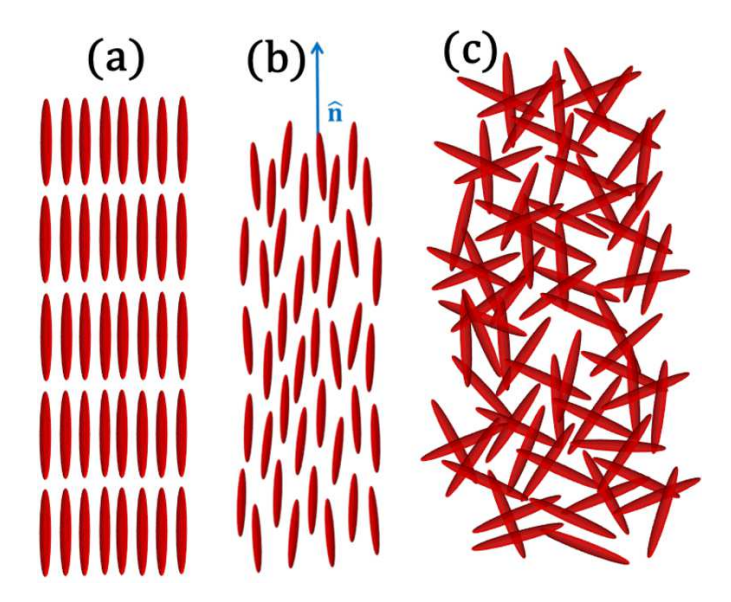


FIGURE 1.1: Schematic diagram showing (a) Crystalline phase, and (b) Liquid crystal phase and, (c) Isotropic phase.

preparation and the physical conditions, liquid crystals can be classified as thermotropic and lyotropic mainly. However, there exist another type of liquid crystals called metallotropic liquid crystals [1-7]. Thermotropic LCs exhibit liquid crystalline character that depends on the temperature. However, lyotropic liquid crystal character is dependent both on the temperature and the typical concentrations involved. In addition to the temperature and the concentration, the metallotropic LC also bear close dependence on inorganic-organic composition ratio. Liquid crystal molecules are anisotropic in shape. Liquid crystal molecules can have variety of shapes like rod shaped molecules, banana shaped molecules, disc shaped molecules, etc. [8-11]. Figure 1.2 shows the schematic

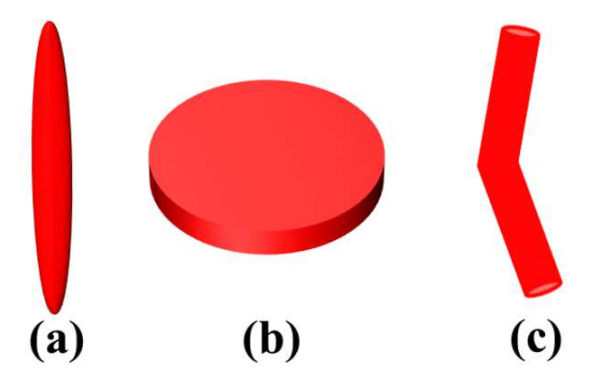


FIGURE 1.2: Schematic diagram showing different shape liquid crystal mesogens. (a) Rod-like molecule, (b) Disc-shaped molecule, and (c) Bent core molecule.

diagram of different shaped liquid crystal mesogens. Figure 1.2(a) shows the most common rod like liquid crystal mesogen and Fig. 1.2(b) represents a disc shaped liquid crystal mesogen and Fig. 1.2(c) represent the banana shaped liquid crystal mesogen respectively.

Liquid crystals composed of rod shaped molecules are also known as calamitic liquid crystals. The average orientation direction in which the LC molecules orient in a particular mesophase is known as director. It is represented by \hat{n} . The liquid crystal director is apolar in nematic i.e. \hat{n} and $-\hat{n}$ are equivalent. Liquid crystal director (\hat{n}) is a dimensionless vector. In case of smectic mesophases, the angle between director \hat{n} and the layer normal \hat{z} varies from one mesophase to another [1,2]. The degree of order across the boundaries in a phase transition system is known as the order parameter. The scalar order parameter for cylindrically symmetric molecules like rod shaped liquid crystal molecules is given by the following scalar equation:

$$S = \frac{1}{2} < 3\cos^2\theta - 1 > \tag{1.1}$$

where <> denotes the ensemble average, θ is basically the angle between the molecular long axis and the director. For the state with long molecular axis perfectly aligned along

the director S=1 and S=0 for disordered isotropic state.

In all the experiments, we have used thermotropic calamitic liquid crystals. Some of the liquid crystal sub-phases namely nematic, smectic and ferroelectric are discussed below.



FIGURE 1.3: Schematic diagram showing nematic phase liquid crystal. Red rods indicate calamitic molecules. Blue arrow represents the director \hat{n} .

1.1.1 Nematic phase

The nematic LC phase is the most common and the simplest phase with just long range orientational order and no positional order. The word "nema" has its origin from the Greek which means "thread like". This term basically relates to the thread like appearance of topological defects that are observed in the nematic phase. In this phase, most of the molecules orient in one direction [1]. The orientational order parameter S varies from 0.3 to 0.8 in the case of nematic phase. Figure 1.3 shows the schematic diagram of nemtaic phase with rod shaped molecules.

1.1.2 Smectic phase

In the case of smectic A (SmA) and smectic C (SmC) phases, there exists an additional quasi one dimensional positional order as the liquid crystal molecules are arranged in layers. These layers could slide over one another due to the relatively weak interlayer attractions. In a mesomorphic liquid crystal compound, smectic phase is usually found at lower temperatures than the nematic phase. Both the smectic phases are more viscous than the nematic phase. The difference between the SmC and SmA lies in the orientation of the director mainly. The director \hat{n} and the layer normal \hat{z} lie parallel to each other in

SmA case whereas in SmC phase, the director is tilted with respect to the layer normal. This tilt angle θ reduces the layer thickness in the SmC phase [2]. In case of SmA, the molecular length is equal to the layer thickness. Figure 1.4 and Fig. 1.5 shows the schematic molecular arrangement of the rod-like molecules in SmA and SmC phases respectively.



FIGURE 1.4: Schematic diagram showing Smectic-A phase. Red rods indicate calamitic molecules. The blue and red lines indicate the director \hat{n} and the layer normal \hat{z} .



FIGURE 1.5: Schematic diagram showing Smectic-C phase. Red rods indicate calamitic molecules. θ is the angle subtended by the director with the layer normal.

1.1.3 Ferroelectric liquid crystals

When the Smectic-C phase is composed of chiral molecules, the chiral interactions among the molecules gives rise to the formation of helical structure. This phase is known as Smectic-C* (SmC*). In such a phase, the LC molecular tilt direction precesses along the surface of a cone. This precession is about an arbitrary axis that is perpendicular to

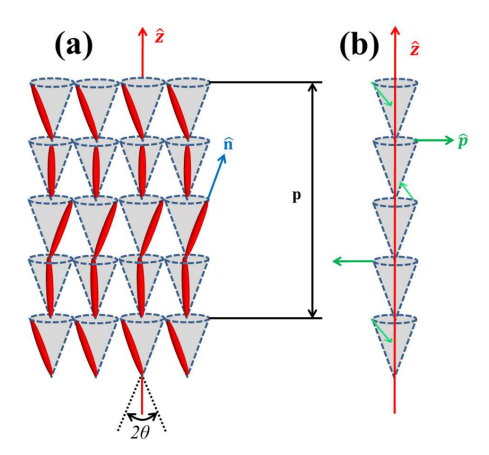


FIGURE 1.6: The helicoidal structure of ferroelectric liquid crystal. The spontaneous polarisation (\hat{p}) in each layer is always perpendicular to the director \hat{n} and tangential to the circle of intersection of the cone with the boundary plane of the layer. (a) Orientation of the molecule around a cone with respect to the axis of a right cone. (b) Orientation of spontaneous polarization in each layer of the FLC. The red, blue and green lines represent the cone axis, director and the spontaneous polarization direction of the molecules respectively.

the constituent layers. This rotation of the molecules around the helix gives rise to the spontaneous polarization of the sample. The distance or number of layers upto which there occurs a 180° phase change in the LC director along the surface of a right cone is called pitch (p). Depending upon the chirality of the constituent molecules, the pitch can either be right handed or left handed. The unwinding of the helix among the molecules could be achieved by the application of strong electric and magnetic fields. Figure 1.6 shows the schematic diagram of FLC phase. As can be seen in Fig. 1.6(a), in each layer the FLC molecules (director, \hat{n}) orient themselves along the cone surface. The pitch of the FLC sample in our case is 2 μ m. The angle θ represents the angle subtended by the director with respect to the right cone axis [10-13]. Figure 1.6(b) shows the direction of spontaneous polarization (\hat{p} , green arrow) with respect to the cone axis represented by red line (\hat{z}).

1.2 Physical properties of liquid crystals

Some of the physical properties possessed by the liquids crystals are discussed below [14].

1.2.1 Refractive index

Refractive index of a material determines the relative speed of light in the material. This property is crucial for the total internal reflection in the optical microresonators [15,16]. Liquids crystals are optically uniaxial. For liquid crystals, the speed of light having polarisation parallel to the director is different from that of the light polarised perpendicular to it. The uniaxial nematic liquid crystal possesses two principal refractive indices namely extraordinary refractive index n_e and ordinary refractive index n_o . The subscripts "e" and "o" stand for extraordinary and ordinary rays of light respectively. Since the optic axis is parallel to the director in case of nematic liquid crystals, therefore $n_e = n_{\parallel}$ and $n_o = n_{\perp}$. The birefringence is given by $\Delta n = (n_e - n_o) = (n_{\parallel} - n_{\perp})$. For nematic liquid crystals, the average refractive index is given by the following equation.

$$\langle n^2 \rangle = \frac{1}{3} (n_{\parallel}^2 + 2n_{\perp}^2)$$
 (1.2)

1.2.2 Dielectric anisotropy

Dielectric constant of any material is an electrical property that determines its response to the external electric field. It depends on the distribution of the electrical charges in the molecules and the intermolecular interactions. For the liquid crystals consisting of apolar molecules, only an induced polarization accounts. However, for the apolar liquid crystal molecules, there exists in addition to the total induced polarization, the orientation polarization. The orientation polarization arises in polar molecules due to the permanent dipole moments' tendency to orient themselves parallel to the applied electric field [2,15,16].

In uniaxial nematic liquid crystals, the dielectric constants ε_{\parallel} and ε_{\perp} are measured with the applied electric field being parallel and perpendicular to the director (\hat{n}) respectively. The dielectric anisotropy of the liquid crystals is given by the following equation:

$$\Delta \epsilon = (\epsilon_{\parallel} - \epsilon_{\perp}) = \frac{4\pi\rho}{M} N_A h F[\Delta \gamma^E - F \frac{\mu^2}{2k_B T} (1 - 3\cos^2 \beta)] S$$
 (1.3)

where M is the molar weight, h is the cavity field factor, F is the reaction field factor for spherical cavity, $\Delta \gamma^E$ is the polarizability anisotropy and μ is the dipole moment of the molecule. When $\beta < 55^{\circ}$, the liquid crystal compound exhibits a positive dielectric anisotropy, whereas it exhibits the negative dielectric anisotropy when $\beta > 55^{\circ}$. Liquid crystal materials that possess larger dielectric anisotropy are desirable for fast response field based applications. When the external electric field is applied, the positive dielectric anisotropy LC try to reorient in the field direction in order to minimise the elastic and electric energy, with their longer axis pointing parallel to the field. However, for negative dielectric anisotropy LC the shorter axis orients in the applied field direction.

1.2.3 Freedericksz transition

When an external electric or magnetic field is applied to an aligned sample of a nematic liquid crystal, the director tends to reorient in the applied field direction. Depending upon the sign of dielectric anisotropy of the aligned nematic liquid crystal, the molecules will orient either parallel or perpendicular to the applied field [1,2,15]. If the applied electric field is orthogonal to the plane containing the homogenously aligned nematic liquid crystal sample with $\Delta\epsilon > 0$, then the director reorients in the direction of the applied field beyond a particular field, called as Freedericksz threshold field. In case of the liquid crystal sample with $\Delta\epsilon < 0$ aligned homeotropically, the director tends to reorient perpendicular to the applied field [1,2]. The threshold voltage which is needed to cause the reorientation of the director from the otherwise pre-aligned orientation is given by the following equation:

$$V_{th} = \frac{\pi}{d} \sqrt{\frac{K_{11}}{\epsilon_0 \Delta \epsilon}} \tag{1.4}$$

where ϵ_0 is the vacuum dielectric permittivity and d is the separation distance between the two electrodes of a conducting cell.

1.3 Liquid crystal microdroplets

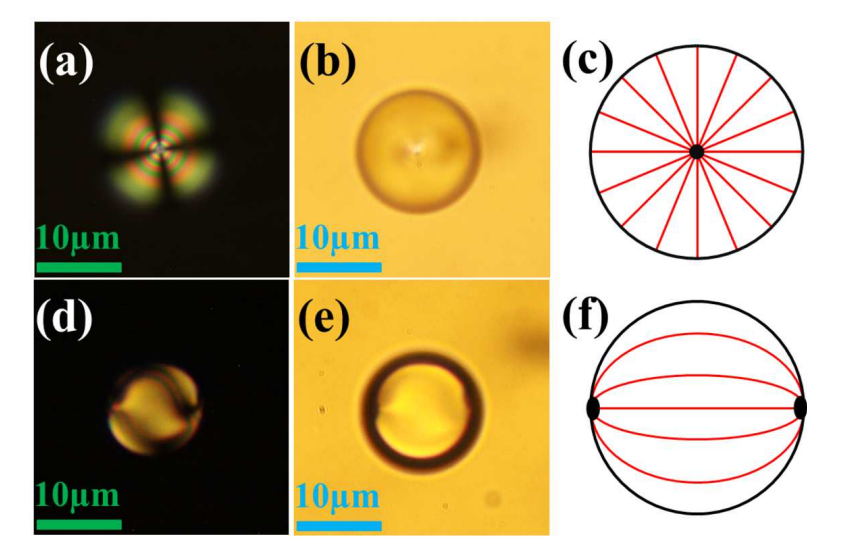


FIGURE 1.7: Types of liquid crystal microdroplets: (a) Radial microdroplet under crossed polarizers. (b) Radial microdroplet without crossed polarizers. (c) Schematic diagram of a radial droplet. (d) Bipolar microdroplet under crossed polarizers. (e) Bipolar droplet without crossed polarizers. (f) Schematic diagram of bipolar droplet. Black dot at the centre of the radial microdroplet and two small black dots at diamterically opposite side of the bipolar droplet represent defects.

The boundary conditions play an important role in the structure of liquid crystal microdroplets [17]. In case of homeotropic anchoring medium, like PDMS a radial droplet with a point defect located at the centre is formed. Under such boundary conditions, the liquid crystal director tend to align perpendicular to the surrounding medium interface. On the other hand, when the surrounding medium is of homogeneous anchoring type, usually a pair of point defects that are diametrically opposite to eachother is formed. In homogeneous anchoring conditions, the liquid crystal director tends to align parallel to the medium interface. Due to the presence of a pair of defects at the periphery, the bipolar liquid crystal microdroplets do not yield well spaced whispering gallery modes often [18,19]. Thus radial liquid crystal microdroplets were chosen for experiments over the bipolar microdroplets. Figure 1.7 shows the radial and bipolar liquid crystal microdroplets suspended in two different mediums. Figure 1.7(a,b,c) shows a radial LC microdroplet under crossed polarisers, without crossed polarisers and the schematics of the director field in the microdroplet respectively. Similarly, Fig. 1.7(d,e,f) shows the bipolar LC microdroplet under the crossed polarisers, without crossed polarisers and the schematics of the director field respectively.

1.4 Optical resonators and historical background

An optical resonator is a physical structure which gives rise to the standing wave pattern of electro-magnetic wave field within the cavity. These microresonators are composed of higher refractive index materials and suspended in a medium having lesser refractive index like air, water, polymer, etc [20-23]. When a ray of light strikes the interface within the cavity at an incident angle which is greater than the critical angle $(\theta_i \geq \theta_c)$, the ray of light is reflected back into the denser medium and it circumnavigates along the periphery of the cavity by virtue of total internal reflection. If the reflected ray of light meets in phase at the point where it originated from, optical resonance takes place and the phenomenon is known as whispering gallery mode (WGM) optical resonance [20,21]. This phenomenon is also called morphology dependent resonance (MDR) owing to the excited mode's dependence on the morphology of the microcavity. Whispering gallery mode optical resonance phenomenon derives its roots from the famous experiment on acoustic waves by Lord Rayleigh at Saint Paul's Cathedral Church, London in 1878 [24]. Similar sound resonance phenomenon is observed in Gol Gumbaz, Bijapur, India [25]. In fact, many structures with curve-linear design within, support the sound resonant phenomenon. Inside all such structures, the sound whispers are audible across the galleries but not at any intermediate position [26,27]. Figure 1.8(a,b) depicts the schematics of an acoustic whispering gallery and an electromagnetic whispering gallery. As shown in Fig. 1.8(a), the whisper (yellow arrowed lines) produced by a talker is

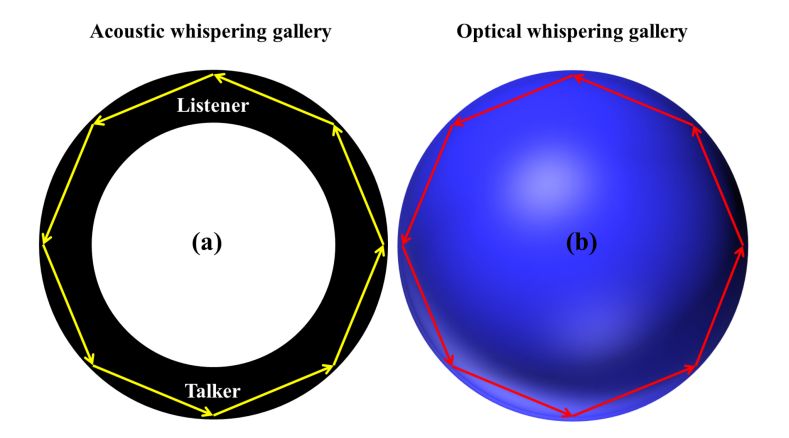


FIGURE 1.8: Schematics of an (a) Acoustic whispering gallery and, (b) Optical whispering gallery. The yellow and red arrows indicate the paths of an acoustic wave and an optical wave respectively.

reflected back into the cavity by means of boundary walls. In the similar fashion in Fig. 1.8(b), a ray of light (the red arrow lines) originating at a point on the edge of the WGM resonator is guided and reflected back multiply at the resonator interface by virtue of total internal reflection.

Over the passage of time, the whispering gallery mode resonance phenomenon has been reported in the case of electromagnetic waves for different curved morphologies [28]. Figure 1.9 shows the common types of optical microresonators. The optical microresonators could be divided into two categories: Fabry-Perot (FP) microresonators and whispering gallery mode (WGM) microresonators [29]. WGM microresonators exist in

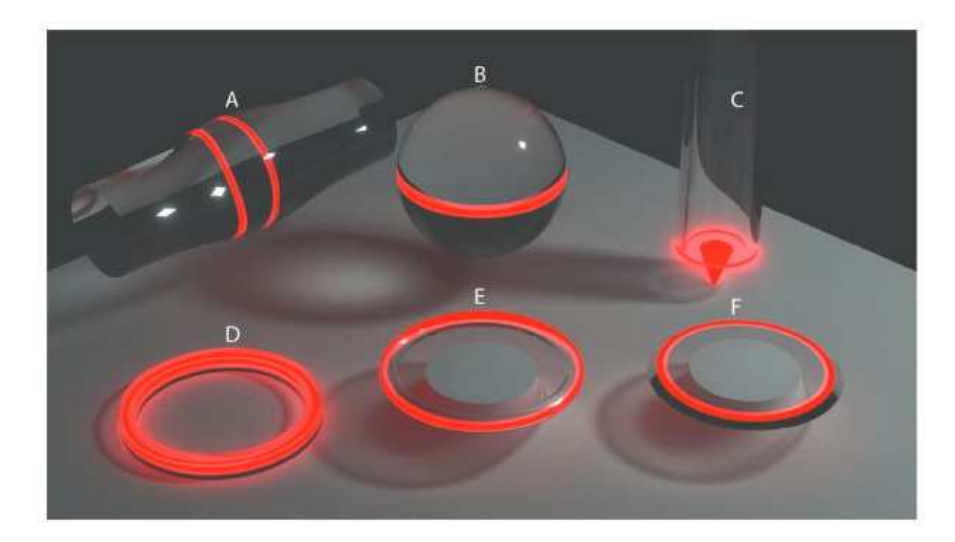


FIGURE 1.9: Different types of optical microresonators: (a) Microbottle, (b) Microsphere, (c) Fabry-Perot, (d) Microring, (e) Microtoroid and (f) Microdisk. Red curves indicate optical resonances in the respective microresonators. This image is adapted from Ref. [29]

multiple shapes. Figure 1.9(a,b,d,e,f) shows the five commonly studied shapes for WGM microresonators which are bottle, sphere, ring, toroid and disk shapes respectively. In the case of WGM optical microresonators possessing azimuthally symmetric geometries, the light is confined via total internal reflection. In case of FP microresonators shown in Fig. 1.9(c), the light is trapped between a pair of parallel mirrors. Both the mirrors may either be flat or curved in design and the resonator volume is the empty space between the pair of reflecting mirrors.

1.5 Liquid crystal based optical microresonators

Solid dielectric based spherical microresonators have high quality factor and have been studied to a great extent [20]. However, due to their rigid structure they are not easily tunable by external fields such as electric and magnetic. In this context, very recently liquid crystal based microresonators have drawn significant attention [21]. Humar et al. first reported WGM optical resonance in nematic LC microdroplets [30]. In the case of liquid crystal based optical microresonators, the WGMs can be changed easily by varying the temperature, external electric and magnetic fields. The evanescent field that exists upto a few hundreds of nanometres and lies outside the microcavity makes these tiny resonators efficient sensors. Any modulation in the evanescent field domain of these microdroplets is strongly reflected in their optical resonance. Based on this, surfactant sensing by nematic microdroplets was reported through boundary change mechanism by Humar et al. [31]. Subsequently they showed three dimensional lasing ability of the microdroplets [32]. Detection of subtle phase transition among the liquid crystal mesophases has also been demonstrated from the optical WGM study [33]. Yan Wang et al. have studied the dve doped cholesteric liquid crystal microdroplet based microcavities [34].

We confined our research interest on the liquid crystal based spherical optical microresonators mainly due to their relative ease of formation, availability and morphology assisted tunability of the optical WGMs. A schematic representation of WGM optical resonance from a spherical microresonator using ray optics and wave optics is shown in Figure 1.10(a,b). Various methods like thermal itching, top-down approach, etc. have been used to fabricate such optical microresonators in the past [20,35]. The underlying principle behind such optical microresonators is that they resonantly couple light into small volumes. The resonant modes that are supported by these optical microresonators are basically dependent on the size and the morphology of the microresonator. Any alteration of the size or morphology of the microresonator by means of any external stimuli like electric and magnetic fields, temperature, etc. results in the subsequent changes in the resonant modes, paving the way for optical sensing application. In addition, these

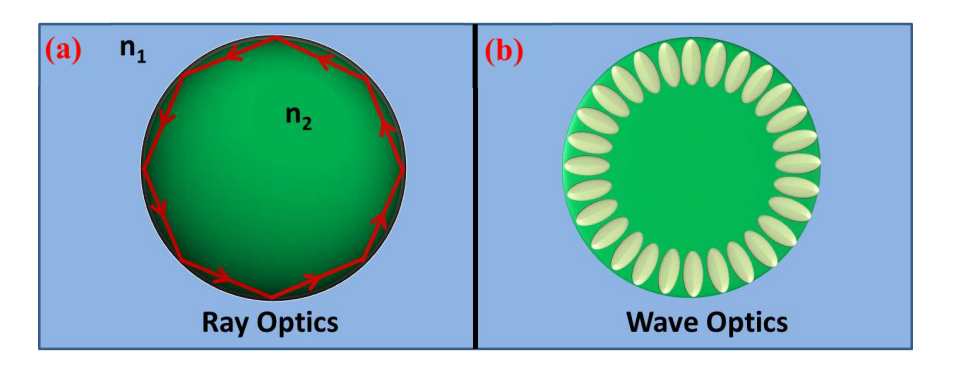


FIGURE 1.10: (a) Schematic diagram showing the WGM optical resonance of a spherical microresonator using ray and wave optics. n_1 and n_2 are the refractive indices of the respective media. (b) Small ellipsoids represent the electric field distribution of resonant mode, q = 1.

microresonators act as high quality factor resonators. When an active material is added to the microresonators, the optical pumping and the subsequent feedback provided by the cavity supersedes the cavity losses and gives rise to the whispering gallery mode lasing [22,35].

The general properties based on which an optical resonator is characterized are discussed below.

1.5.1 Quality factor (Q-factor)

The quality factor of a spherical optical microresonator defines the relation between the total optical energy that is stored in the resonator and the total optical loss incurred by the resonator. The Q-factor actually characterizes the capacity of the resonator for holding the optical resonant energy within it. It is both a unitless and a dimensionless quantity. Theoretically, it is defined as 2π times the ratio of the stored optical energy to the optical energy dissipated per cycle of the light. Experimentally, the q-factor is meant as the ratio of the resonance frequency λ_0 and the line width which is basically the full width at half-maximum (FWHM) $\delta\lambda$ of the resonant mode and is given as below:

$$Q = \left(\frac{\lambda_0}{\delta\lambda}\right) = \omega\tau\tag{1.5}$$

where Q, λ_0 , $\delta\lambda$, ω and τ denotes q-factor, resonant wavelength, FWHM corresponding to the resonant wavelength, optical frequency and life time of photon in the resonator respectively. Apart from this relation, the net q-factor of an optical resonator can be divided into two broad categories viz. $Q_{intrinsic}$ and $Q_{coupling}$. The $Q_{intrinsic}$ includes the

contributions from the resonator material, radiation loss, resonator surface imperfections scattering and inner and outer impurities to the resonator while the $Q_{coupling}$ represents the loss that occurs on account of the coupling of light into or out of the resonator [36-38]. The over all q-factor for a spherical optical microresonator can be written as:

$$1/Q_{tot} = 1/Q_{mat} + 1/Q_{rad} + 1/Q_{LC} + 1/Q_{ss} + 1/Q_{coupling}$$
(1.6)

where Q_{mat} refers to the intrinsic material loss due to the absorption and scattering in the dielectric medium of the resonator. It is given by

$$Q_{mat} = 2\pi n_r / \lambda \alpha_{mat} \tag{1.7}$$

where α_{mat} is the absorption decay constant and n_r is the refractive index of the resonator. The radiation loss Q_{rad} is due to the curvature of the spherical microcavity. Q_{ss} refers to the surface scattering loss due to either roughness or impurities, Q_{LC} refers to the loss due to the thermal fluctuations of the director and $Q_{coupling}$ refers to the optical losses involved in light coupling into the external optical devices like prism, fibre, etc. The higher Q-factor indicates sharper peaks and thus lower energy losses in the cavity and vice versa. Till now, the highest q-factor reported in liquid crystal based spherical microcavities is 1.2×10^4 [39].

1.5.2 Free spectral range

The free spectral range (FSR) of an optical resonator is defined as the distance between the two consecutive WGM peaks of a resonance spectrum. For spherical optical microresonator, FSR depends on the radius and the refractive index of the microresonator. The FSR is inversely proportional to both the radius and the refractive index of the optical microresonator and is given by the following equation [19,40]:

$$\delta\lambda = \frac{\lambda_r^2}{2\pi \times n_{eff} \times R} \tag{1.8}$$

where $\delta\lambda$, λ_r , n_{eff} and R denote FSR, resonant wavelength, effective refractive index and radius of the resonator respectively. Smaller size microdroplets are preferred for optical studies due to their large FSR.

1.5.3 Mode volume

This is one of the most important properties that lays the actual foundation for WGM sensing applications. This is defined as the volume occupied by a resonant mode within the resonator. For an optical microresonator, the physical volume occupied by a mode field typically ranges from hundred to few thousand cubic microns. Small mode volumes are more desirable in optical resonators. The mode field existing just outside the optical resonator could be altered easily by means of various external stimuli and thus easily detected [18]. In a cavity, the spontaneous decay rate is dependent on the spectral density of the modes. Unlike in vacuum, the density of modes is larger at resonant frequencies in a cavity. Consequently, enhanced emission of light occurs at the modes. In addition to the larger decay rate at the modes, the light is directionally emitted to the mode itself. As a result, larger intensity peaks are observed instead of the dips at the resonant frequencies. This alteration of the spontaneous emission of light in a cavity is known as Purcell effect [20]. Purcell factor defines the enhanced emission at a given resonant frequency and is given by:

$$P = \frac{3}{4\pi^2} \left(\frac{\lambda}{n}\right)^3 \left(\frac{Q}{V}\right) \tag{1.9}$$

Where Q, V, λ and n are the quality factor, mode volume, resonant wavelength and refractive index of the cavity respectively.

1.6 Whispering gallery mode theory for an isotropic microsphere

In order to calculate the linewidths and the wavelength corresponding to the excited WGMs on the spectrum recorded from a spherical dielectric microcavity, the Maxwell's equations are solved in spherical coordinate system with appropriate boundary conditions [41-44]. The general solutions to the electric field inside and outside a small particle is calculated using Mie scattering theory [45]. To start with, we write the set of Maxwell's equation for non conducting and charge free isotropic medium as following:

$$\nabla \cdot \mathbf{E} = 0 \tag{1.10}$$

$$\nabla . \mathbf{B} = 0 \tag{1.11}$$

$$\nabla \times \mathbf{E} = -\frac{\partial \mathbf{B}}{\partial t} \tag{1.12}$$

For a material, the relative permeability and relative permittivity are given by $\mu_r = \frac{\mu}{\mu_0}$ and $\epsilon_r = \frac{\epsilon}{\epsilon_0}$ respectively. Here, μ and ϵ denote the permeability and the permittivity of the material and μ_0 and ϵ_0 are the permeability and the permittivity of the free space respectively. Thus, we can write:

$$\nabla \times \mathbf{B} = \mu \mu_0 \epsilon \epsilon_0 \times \frac{\partial \mathbf{E}}{\partial t}$$
 (1.13)

Since for any vector $\vec{\mathbf{A}}$,

$$\nabla \times \nabla \times \mathbf{A} = \nabla(\nabla \cdot \mathbf{A}) - \nabla^2 \mathbf{A} \tag{1.14}$$

Using the vector identity equation (1.14) and taking the curl of the equation (1.12) and equation (1.13), we get the following:

$$\nabla \times \nabla \times \mathbf{E} = -\frac{\partial(\nabla \times \mathbf{B})}{\partial t} = -\mu \mu_0 \epsilon \epsilon_0 \times \frac{\partial^2 \mathbf{E}}{\partial t^2}$$
 (1.15)

$$\nabla \times \nabla \times \mathbf{B} = -\mu \mu_0 \epsilon \epsilon_0 \times \frac{\partial (\nabla \times \mathbf{E})}{\partial t} = -\mu \mu_0 \epsilon \epsilon_0 \times \frac{\partial^2 \mathbf{B}}{\partial t^2}$$
 (1.16)

Both of the equations (1.15) and (1.16) upon further simplification reduces to the following:

$$\nabla^2 \mathbf{E} = -\mu \mu_0 \epsilon \epsilon_0 \times \frac{\partial^2 \mathbf{E}}{\partial t^2}$$
 (1.17)

$$\nabla^2 \mathbf{B} = -\mu \mu_0 \epsilon \epsilon_0 \times \frac{\partial^2 \mathbf{B}}{\partial t^2}$$
 (1.18)

Fixing $c = 1/\sqrt{\mu\mu_0\epsilon\epsilon_0}$ in the above equations, we get after the rearrangement:

$$\frac{\partial^2 \mathbf{E}}{\partial t^2} - c^2 \nabla^2 \mathbf{E} = 0 \tag{1.19}$$

$$\frac{\partial^2 \mathbf{B}}{\partial t^2} - c^2 \nabla^2 \mathbf{B} = 0 \tag{1.20}$$

Let us assume an oscillating field in the form $\mathbf{E} = \mathbf{E}_0 \exp i(\mathbf{k}.\mathbf{r} - \omega t)$ and $\mathbf{B} = \mathbf{B}_0 \exp i(\mathbf{k}.\mathbf{r} - \omega t)$, where $\mathbf{k} = \omega/c$, be the solutions of the above two equations. Upon using these solutions in these equations, the wave equations (1.19) and (1.20) take the forms as below.

$$k^2 \mathbf{E} + \nabla^2 \mathbf{E} = 0 \tag{1.21}$$

and

$$k^2 \mathbf{B} + \nabla^2 \mathbf{B} = 0 \tag{1.22}$$

Equations (1.21) and (1.22) are the Helmholtz equation for electric and magnetic field respectively [18]. Let us create a vector function \mathbf{M} which has got zero divergence (i.e $\nabla .\mathbf{M} = 0$) with the help of a scalar function ψ , and a constant vector function \mathbf{c} , such that.

$$\mathbf{M} = \nabla \times (\mathbf{c}\psi) \tag{1.23}$$

Since ψ satisfies the Helmholtz equation i.e.

$$\nabla^2 \psi + k^2 \psi = 0 \tag{1.24}$$

therefore \mathbf{M} also satisfies the general vector wave equation i.e.

$$\nabla^2 \mathbf{M} + k^2 \mathbf{M} = 0 \tag{1.25}$$

Similarly another vector function \mathbf{N} with zero divergence (i.e $\nabla \cdot \mathbf{N} = 0$) can be constructed, such that

$$\mathbf{N} = \frac{\nabla \times \mathbf{M}}{k} \tag{1.26}$$

while using vector identity equation (1.14) and equation (1.26) together result in

$$\nabla \times \mathbf{N} = \frac{(\nabla \times \nabla \times \mathbf{M})}{k} = \frac{(\nabla \cdot (\nabla \cdot \mathbf{M}))}{k} - \frac{(\nabla^2 \mathbf{M})}{k} = 0 - (-\frac{k^2 \mathbf{M}}{k}) = k\mathbf{M}$$
 (1.27)

Since \mathbf{M} and \mathbf{N} satisfy the vector equation and their respective divergence equals to zero and also the curl of \mathbf{M} is directly proportional to the \mathbf{N} and the curl of the \mathbf{N} is directly proportional to the \mathbf{M} , hence \mathbf{M} and \mathbf{N} represent harmonic functions of an electromagnetic field and ψ , a generating scalar function. Thus, it is more convenient to solve the scalar wave equation rather than vector equation [46,51]. For the sake of spherical symmetry of our microcavity, we solve the scalar wave equation (1.24) in spherical coordinate system. Figure 1.11 shows an arbitary WGM wave propagating

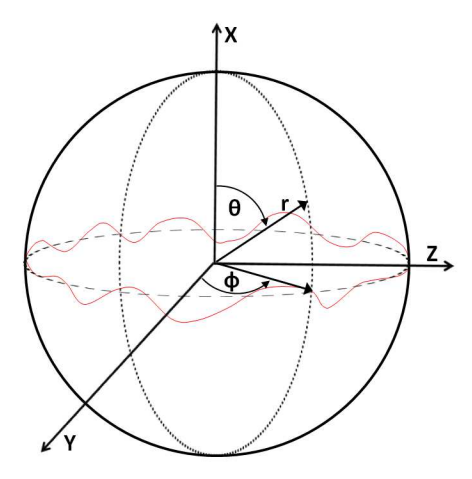


FIGURE 1.11: Spherical coordinate system: Red wavy loop depicts an arbitrary WGM wave propagating along the circumference of the equatorial plane.

along the equatorial plane with respect to the spherical coordinate system. Thus

$$\frac{1}{r^2}\frac{\partial}{\partial r}(r^2\frac{\partial\psi}{\partial r}) + \frac{1}{r^2\sin\theta}\frac{\partial}{\partial\theta}(\sin\theta\frac{\partial\psi}{\partial\theta}) + \frac{1}{r^2\sin^2\theta}(\frac{\partial^2\psi}{\partial\phi^2}) + k^2\psi = 0 \tag{1.28}$$

Since the solution ψ involves three coordinates, we can separate the variables as below

$$\psi(r,\theta,\phi) = R(r)\Theta(\theta)\Phi(\phi) \tag{1.29}$$

Upon substituting $\Psi(r, \theta, \phi)$ in equation (1.28) and dividing by Ψ , we obtain the following set of three separate differential equations in three variables

$$(\frac{d^2\Phi}{d\Phi^2}) + m^2\Phi = 0 (1.30)$$

$$\frac{1}{\sin\theta} \frac{d}{d\theta} (\sin\theta \frac{d\Theta}{d\theta}) + (l(l+1) - \frac{m^2}{\sin^2\theta}) = 0$$
 (1.31)

and

$$\frac{d}{dr}(r^2\frac{dR}{dr}) + (k^2r^2 - l(l+1))R = 0$$
(1.32)

The separation constants l and m are integers and the solutions for equation (1.30) and (1.31) are

$$\Phi = \frac{1}{\sqrt{2\pi}} e^{\pm im\Phi} \tag{1.33}$$

and the associated Legendre functions of the first kind

$$\Theta = P_l^m(\cos \theta) \tag{1.34}$$

l and m represent polar mode number and azimuthal mode number and satisfy ${-}l{\le}m$ ${\le}{+}l$

The solutions of Θ and Φ can be merged together to obtain the spherical harmonics part of the entire solution.

$$\Theta\Phi = \mathbf{N}P_l^m(\cos\theta) \times e^{im\Phi} = Y_l^m(\theta, \phi)$$
 (1.35)

where **N** is a normalization constant of the spherical Harmonics function $Y_l^m(\theta, \phi)$. The solutions to the equation (1.32) are the spherical Bessel functions of first and second kind and are given as

$$y_l(kr) = \sqrt{\frac{\pi}{2kr}} Y_{l+\frac{1}{2}}(kr)$$
 (1.36)

$$j_l(kr) = \sqrt{\frac{\pi}{2kr}} J_{l+\frac{1}{2}}(kr)$$
 (1.37)

Where Y and J represent ordinary Bessel functions The whole solutions becomes then

$$\Psi_{lm} = Y_l^m(\theta, \phi) z_l(kr) \tag{1.38}$$

 z_l is either j_l or y_l or could be any linear combination of both j_l and y_l . Two special linear combinations of j_l and y_l are called *spherical Bessel functions of the third kind*. Such linear combinations are also known as *spherical Hankel functions* and are given below:

$$h_l^{(1)} = j_l(kr) + iy_l(kr) (1.39)$$

and

$$h_l^{(2)} = j_l(kr) - iy_l(kr) (1.40)$$

The optical whispering gallery modes emanating from a spherical optical microcavity can be characterized and distinguished by a set of four mode numbers viz. q which represents the radial mode number, l which tells the polar mode number, p which indicates the polarization of the wave and m signifies the azimuthal mode number of the circulating wave respectively. The radial mode number q actually signifies the number of maxima in the radial direction of the microcavity that appears as a light ring wrapping the circumference of the optical microcavity. The polar mode number l signifies the number of wavelengths for one circulation of each light ring denoted by q. As the name azimuthal indicates, the mode number m shows the inclination of the circumnavigating

light orbit with respect to the reference frame [41,47].

1.7 Approximate solutions

For an isotropic optical microcavity, both the transverse electric (TE) and the transverse magnetic (TM) polarizations see the same refractive index during their propagation. Using analytical solutions of Mie type theories, the resonant frequencies for spherical birefringent microresonators can be calculated [18,30]. It has been shown that for the TE mode in the radial anisotropic microsphere is equivalent to the TE mode in an isotropic microsphere with the ordinary refractive index, whereas the TM mode couples to both the ordinary and extraordinary refractive indices. However for a spherical resonator with small radial mode numbers q the resonant WGM frequencies can be obtained from the following equation [48,49]:

$$n_s ka = l - \alpha_q \left(\frac{l}{2}\right)^{1/3} - \frac{\chi n_r}{\sqrt{n_r^2 - 1}} + \frac{3\alpha_q^2}{20} \left(\frac{l}{2}\right)^{-1/3} - \frac{\alpha_q n_r \chi(2\chi^2 - 3n_r^2)}{6(n_r^2 - 1)^{3/2}} \left(\frac{l}{2}\right)^{-2/3} + O(l^{-1}) \quad (1.41)$$

where k is the wavenumber, a is the radius of the microdroplet, l >> 1, q = 1, 2, 3... are mode numbers and $\chi = 1/n_r^2$ for TM modes while $\chi = 1$ for TE modes. α_q are negative q-th zeros of the Airy function and $n_r = n_s/n_a$ is the relative refractive index, where n_a is the index of the surrounding medium and n_s is the refractive index of the microdroplets.

In order to understand the physics behind WGMs, only the first term l can be taken into consideration from the equation (1.41) for the sake of simple approximation. Substituting $k = \frac{2\pi}{\lambda}$ we get,

$$2\pi an \approx l\lambda \tag{1.42}$$

The left side of this equation (1.42) represents the optical path around the microdroplet which is circumference multiplied by the refractive index. The integer multiple of wavelengths is approximately equal to the optical path traveled by the light around the optical microsphere. It is noteworthy that the above obtained expression under simple approximation is valid for the first radial modes where q = 1.

1.8 Whispering gallery modes in anisotropic microsphere

In case of an anisotropic sphere like liquid crystal microdroplet with homeotropic anchoring, the radial axis and the optical axis is in the same direction. In such LC microresonators, the TE and TM modes are separated from each other owing to the presence of the two refractive indices (n_e and n_o). Consequently, the electric and magnetic fields in the radial direction are not same as in the case of isotropic microsphere. The extraordinary dielectric permittivity ε_e is in the radial direction while as the ordinary dielectric permittivity ε_o is in the tangential direction of the anisotropic sphere. Upon performing the similar derivations as in Sec. 1.6 for the radial dependence of the electric and magnetic field for TE and TM modes, the respective differential equations obtained are [50]:

$$\frac{d}{dr}\left(r^2\frac{dR^{(1)}(r)}{dr}\right) + (k^2r^2 - l(l+1))R^{(1)}(r) = 0$$
(1.43)

and

$$\frac{d}{dr}\left(r^{2}\frac{dR^{(1)}(r)}{dr}\right) + (k^{2}r^{2} - l(l+1)\frac{\varepsilon_{0}}{\varepsilon_{e}})R^{(1)}(r) = 0$$
(1.44)

Where $\varepsilon_e = \varepsilon_o$, both these equations are essentially the same and thus yield to the isotropic case (equation (1.32)). Therefore, the solutions to equation 1.43 are the same as for the isotropic sphere, that is the spherical Bessel $j_l(kr)$ and spherical Hankel functions $h_l(kr)$. However for equation (1.44) of TM mode, the solutions are found to be spherical Bessel $j_{\bar{l}}(kr)$ and spherical Hankel functions $h_{\bar{l}}(kr)$ also, but with a non-integer order [30].

$$\tilde{l}(l) = \frac{1}{2} \left[-1 + \sqrt{1 + 4\left(\frac{n_o}{n_e}\right)^2 l(l+1)} \right]$$
(1.45)

Where $n_o = n_e$, $\tilde{l}(l) = l$. The equation for the TE mode is dependent only on the

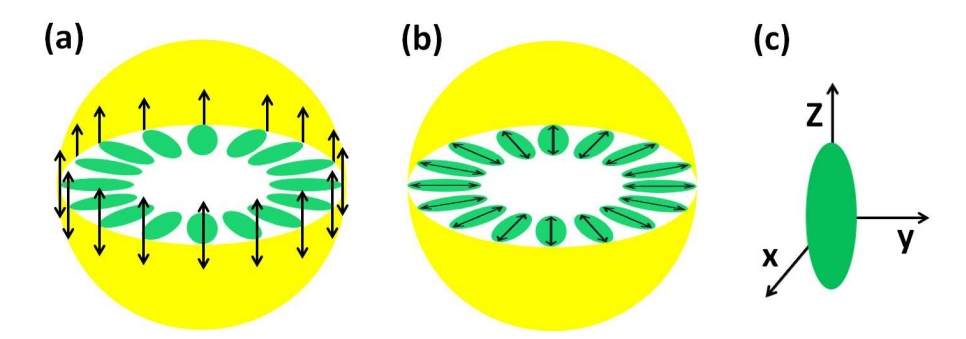


FIGURE 1.12: Schematic diagram showing the electric field oscillation in radial nematic liquid crystal microdroplet for (a) TE modes, (b) TM modes. (c) The green ellipsoid indicates the uniaxial dielectric tensor of the liquid crystal.

ordinary refractive index of the cavity. However, TM mode couples to both the ordinary and the extraordinary refractive indices of the cavity. Depending upon the surrounding medium index supporting the LC microdroplets, only TM modes are supported as a result of large refractive index contrast experienced by it in case of smaller microdroplets [30]. Figure 1.12(a,b) shows the schematic diagram indicating the oscillation of electric field for TE and TM modes in a nematic liquid crystal microdroplet respectively. The green ellipsoid in Fig. 1.12(c) represents the uniaxial dielectric tensor for calamitic liquid crystal. Figure 1.13 shows the WGM spectrum of a 10.5 μ m nematic droplet with designated angular mode numbers. For a microdroplet of diameter 10.6 μ m, we find that only TM modes with radial mode number q=1 are supported. The angular mode numbers (l) for the same microdroplet are calculated using $n_s=1.557$ and $n_a=1.34$. In the wavelength range of 540-680nm, l varies from 71 to 89.

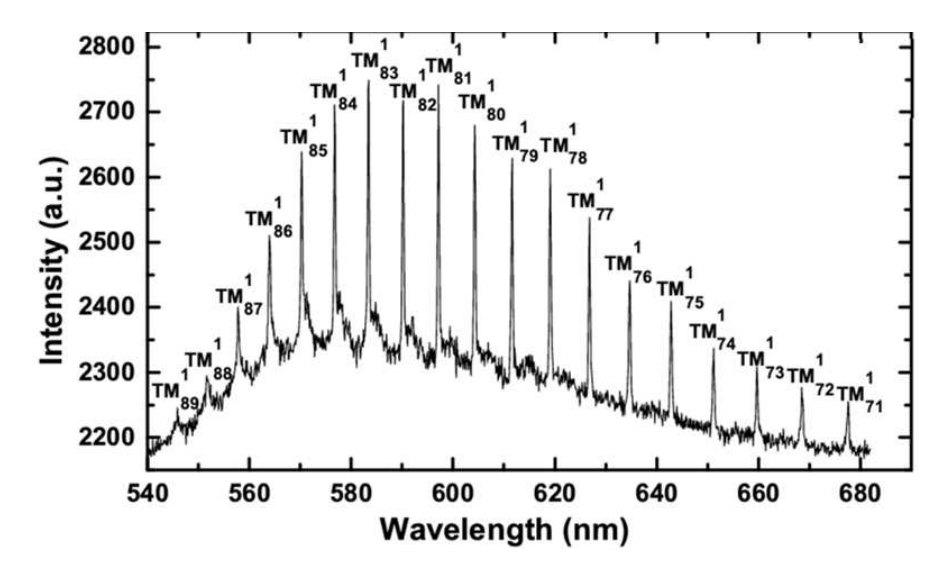


FIGURE 1.13: (a) Designation of WGMs for a $10.6\mu\mathrm{m}$ LC microdroplet. The angular mode number l for radial number q=1, varies from 71 to 89.

1.9 Theory of lasing

LASER stands for light amplification by stimulated emission of radiation. A laser is constructed by three parts viz gain medium, pump source and optical resonator. The role of the pump source is to provide energy to the laser system [20,22]. For instance, some of the commonly used pump sources include electrical discharges, light from another laser, etc. The gain medium is also known as lasing medium or active medium. The gain medium of the laser is the source of optical gain within the laser. The gain is attained in the laser from the stimulated emission which itself is achieved on account of the population inversion through a suitable pump source. Gain medium could be the

dyes mixed with liquid solutions, solids doped with impurities like chromium, gases like carbon dioxide, etc. [22]. A schematic diagram of a conventional laser is shown in Fig. 1.14. The dark green arrow represents the laser beam transmitting out of the output light coupler, which basically has lesser reflectivity than the other parallel reflector. The lighter shade of green represents the active medium and the yellow zig-zag arrow represents the pumping energy source. The optical resonator has been conventionally a set of mirrors with varied transmission properties. The function of the optical resonator is to provide the feedback to the circulating or reflecting light. The trapped light inside the resonator may reflect hundreds of times by the resonator walls before finally exiting from the optical resonator. The optical amplification of the light achieved is an outcome of multiple energy levels of the gain medium, different transition probabilities and the associated various optical losses incurred in the cavity [22,51]. In order to understand

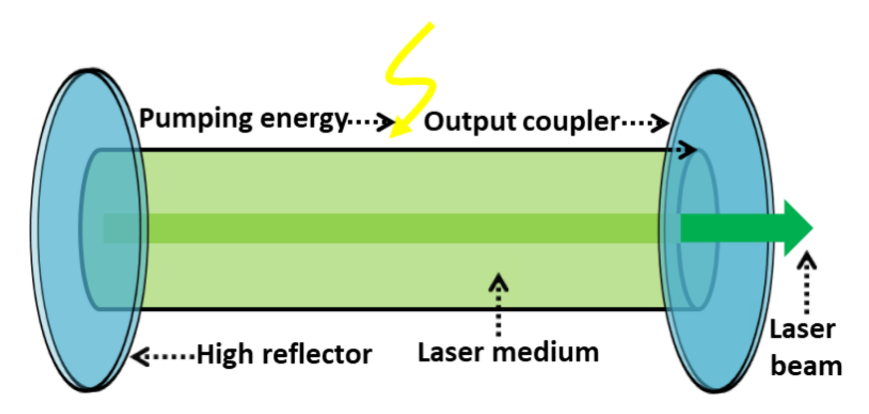


FIGURE 1.14: Schematic diagram of a conventional laser. Thick green arrow indicates the transmitted laser beam.

the optical amplification phenomenon in the laser, let us assume a two energy level system like $| 1 \rangle$ and $| 2 \rangle$ with E_1 being the lower energy level and E_2 the higher energy level respectively. Further, let the corresponding electron number density in the two levels be N_1 and N_2 with total electrons in the system, $N = N_1 + N_2$ and $E_2 - E_1 = hv$.

According to Boltzman law, at thermal equilibrium for the non interacting particles, the ratio of the populations of these two energy levels can be written as following:

$$\frac{N_2}{N_1} = \exp\frac{-(E_2 - E_1)}{k_B T} \tag{1.46}$$

At infinite temperature, all the electrons are equally occupied by N_2 and N_1 levels respectively, while at the zero temperature, all the electrons are filled in N_1 level. For the sake of optical gain, population inversion is a prerequisite needing $N_2 > N_1$. In a two level energy system, since the probability of pumping atoms/molecules into higher energy

level is equal to the probability of stimulating back down the atoms to the lower energy level, a two level system is not feasible for lasing action due to the non occurrence of population inversion. Therefore, a minimum of three energy level system viz |1>, |2>and | 3 > respectively, is necessary to achieve the population inversion for lasing action to occur. An atom resides in an excited energy level for a time interval of 10^{-8} seconds while as in the metastable state, an atom stays for a time range of 10^{-3} to 10^{-6} seconds before falling down to ground state energy level. In such a system, population inversion could be achieved either between $|1\rangle$ and $|2\rangle$ provided transition of atoms/molecules is faster from |2> to |3> or else between |2> and |3> if the transition is faster from |1> to |2>. Well known Einstein coefficients are used to describe the probabilities of transitions in any two level energy system. Accordingly, three types of processes are possible in that system. Firstly, when the system is in a state of excited energy level and is perturbated by an applied electric field of frequency " ω ", in that case a photon with the same phase and the same frequency as that of the external field may be emitted. Such a process of emission is known as stimulated emission. The rate of stimulated emission is given as below:

$$\frac{\partial N_1}{\partial t} = B_{21} u(\omega) g(\omega) N_2 \tag{1.47}$$

where B_{21} is the Einstein B coefficient, $g(\omega)$ is the lineshape of the involved transition and $u(\omega)$ is the spectral energy density. The transition rate for this process is directly proportional to the number of excited states and the incident photon density. Similarly, the another process involved in a three level system is absorption. The rate of absorption is given as:

$$\frac{\partial N_2}{\partial t} = B_{12}u(\omega)g(\omega)N_1 \tag{1.48}$$

In the absorption process, the absorption rate is directly proportional to the incident photon density and also to the number of available ground states. Finally, the third process is called spontaneous emission which is independent of the number density of independent photons. The rate of such a process is given by *Einstein A coefficient* as

$$\frac{\partial N_2}{\partial t} = -A_{21}N_2 \tag{1.49}$$

For such a system, it can be shown [51] that

$$B_{21} = B_{12} = B \tag{1.50}$$

and

$$\frac{A}{B} = \frac{(\hbar^3 \omega^3)}{\pi^2 c^3} \tag{1.51}$$

The laser output power for a microresonator can be written as [22]

$$P = (1 - R_2) \frac{c}{2L} W ag{1.52}$$

Bibliography

- [1] P. J. Collings and M. Hird, *Introduction to liquid crystals chemistry and physics*, Taylor and Francis, (1997).
- [2] P. G. de Gennes and J. Prost, The Physics of Liquid Crystals, 2nd Ed., Clarendon Press, Oxford, (1993).
- [3] S. Chandrashekhar, *Liquid crystals*, Cambridge University Press, Cambridge, (1992).
- [4] S. Singh, *Phase transitions in liquid crystals*, Phys. Rep. **324**, (2000).
- [5] K. Binnemans, *Ionic Liquid Crystals*, Chem. Rev. **105**, (2005).
- [6] P. Oswald, P. Pieranski, Nematic and Cholesteric Liquid Crystals Concepts and Physical Properties Illustrated by Experiments, CRC Press (2005).
- [7] E. F. Gramsbergen, L. Longa and W. H. de Jeut, Landau Theory of the Nematic-Isotropic Phase Transition, The Netherlands, (1986).
- [8] S. Chandrasekhar, B. K. Sadashiva, and K. A. Suresh., Liquid crystals of disc like molecules, Pramana, 9, (1977).
- [9] R. A. Reddy and C. Tschierske, Bent-core liquid crystals: polar order, superstructural chirality and spontaneous desymmetrisation in soft matter systems, J. Mater. Chem. 169 (2006).
- [10] D. M. Walba, D. J. Dyer, T. Sierra, P. L. Cobben, R. Shao and N. A. Clark, Ferroelectric liquid crystals for nonlinear optics: orientation of the disperse red 1 chromophore along the ferroelectric liquid crystal polar axis, J. Am. Chem. Soc., 118 (1996).
- [11] S. Sergeyev, W. Pisula, and Y. H. Geerts, Discotic liquid crystals: a new generation of organic semiconductors, Chem. Soc. Rev., 36, (2007).
- [12] S. T. Lagerwall, Ferroelectric and Antiferroelectric Liquid Crystals, Wiley-VCH Verlag GmbH, Weinheim, Germany (1999).

- [13] C. Bahr, Ferroelectric Properties and Electroclinic Effect, Springer, New York (2001).
- [14] Toralf Scharf., Polarized light in liquid crystals and polymers, Wiley and Sons, New Jersey (2007).
- [15] Paladugu Sathyanarayana, Investigation on the Physical Properties of Unconventional Nematic Liquid Crystals., PhD Dissertation, University of Hyderabad, India (2012).
- [16] Zuhail K. P., Topological Defects Transformation and Structural Transition of Two Dimensional Colloidal Crystals across Nematic to Smectic-A Phase transition., PhD Dissertation, University of Hyderabad, India, (2017).
- [17] P. S. Drzaic, Liquid Crystal Dispersions, World Scientific Publishing: Singapore, (1995).
- [18] Matjaž Humar, Liquid Crystal Microdroplets as Optical Microresonators and Lasers., PhD Dissertation, Jožef Stefan International Postgraduate School Ljubljana, Slovenia, (2012).
- [19] J. A. Sofi, M. A. Mohiddon, N. Dutta, and S. Dhara, Phys. Rev. E, 96, 022702, 477, (2017).
- [20] Kerry Vahala, Optical Microcavities, World Scientific (2004).
- [21] D.K. Yang and S.T. Wu, Fundamentals of Liquid Crystal Devices, Wiley and Sons, (2006).
- [22] Bahaa E. A. Saleh and Malvin Carl Teich, Fundamentals of Photonics, John Wiley and Sons, Inc., (1991).
- [23] S. Arnold, S. Holler, and S. D. Druger, Optical Processes in Microcavities.
- [24] Lord Rayleigh, Theory of Sound, vol. II, 1st edition, London, (1878).
- [25] Raman, C. V. Proceedings of the Indian Association for the Cultivation of Science, "XV. On Whispering Galleries". 7,(1921–1922)
- [26] J. Tyndall, The Science of Sound, New York, Philosophical Library, (1867).
- [27] G. B. Airy, On Sound and Atmospheric Vibrations, with the Mathematical Elements of Music, London, 1871.
- [28] Oraevsky, Anatolii N., Whispering-gallery waves, Quantum Electronics. IOP Publishing. 32,(2002)

- [29] K. D. Heylman, K. A. Knapper, E. H. Horak, M. T. Rea, S. K. Vanga, R. H. Goldsmith, Optical Microresonators for Sensing and Transduction: A Materials Perspective, Adv. Mater. 29, (2017).
- [30] M. Humar, M. Ravnik, S. Pajk and I. Musevic, Nat. Photon., 3, 595 (2009).
- [31] M.Humar and I. Musevic, Opt. Express 18, 26995 (2010).
- [32] M.Humar and I. Musevic, Opt. Express 19, 19836 (2011).
- [33] T. Arun Kumar, M. A. Mohiddon, N.Dutta, Nirmal K, Viswanathan, and Surajit Dhara, Appl. Phys. Lett. 106, 051101 (2015).
- [34] Y. Wang, H. Li, L. Zhao, Y. Liu, S. Liu and J. Yang, Appl. Phys. Lett., 109,231906 (2016).
- [35] John Heebner, Rohit Grover, Tarek Ibrahim, Optical Microresonators Theory, Fabrication, and Applications, Springer Series in optical Sciences, (2008)
- [36] A. B. Matsko and V. S. Ilchenko, Quantum Electronics, 12, 3 (2006).
- [37] S. Arnold, S. I. Shopova, and S. Holler, Opt. Express, 18, 281 (2010).
- [38] M. L. Gorodetsky, A. A. Savchenkov, and V. S. Ilchenko, Opt. Lett. 21, 453 (1996).
- [39] J. A. Sofi, and S. Dhara, Liq. Cryst., 46, 4, 629-639, 477, (2018).
- [40] S. Arnold, S. I. Shopova, and S. Holler, Opt. Express, 18, 281 (2010).
- [41] R. K. Chang, A. J. Campillo, Optical Processes in Microcavities, World Scientific, Singapore, (1998).
- [42] S. M. Spillane, Fiber-coupled Ultra-high-Q Microresonators for Nonlinear and Quantum Optics Thesis, California Institute of Technology, Pasadena, (2004).
- [43] M. Tona, Study on Spherical Microlasers Levitated in an Ion Trap Thesis, Kochi University of Technology, (2002).
- [44] L. Novotny, B. Hecht Principles of Nano-Optics, Cambridge University Press, Cambridge, (2006).
- [45] C. F. Bohren, D. R. Huffman, Absorption and Scattering of Light by Small Particles Wiley Science, New York, (1998).
- [46] Venkata Subba Rao Jampani, Chiral nematic colloidal interactions and photonic properties of nematic colloids, PhD Dissertation, Ljubljana, Slovenia, (2013).

- [47] B. E. Little, J. P. Laine and H. A. Haus, Analytic theory of coupling from tapered fibers and half-blocks into microsphere resonators, Journal of Lightwave Technology, 17(4), (1999).
- [48] C. C. Lam, P. T. Leung, K. Young, Explicit asymptotic formulas for the positions, widths, and strengths of resonances in Mie scattering. J. Opt. Soc. Am. B 9, (1992).
- [49] S. Schiller, Asymptotic expansion of morphiological resonance frequencies in Mie scattering. Appl. Optics **32**, (1993).
- [50] D. K. Cohoon, An exact solution of Mie type for scattering by a multilayer anisotropic sphere, J. Electromagnet. Wave. 3, (1989).
- [51] E. Hecht, Optics Addison Wesley, San Francisco, (2002).

Chapter 2

Materials and methods

2.1 Introduction to the chapter

The characterization of the liquid crystal (LC) microdroplets based microresonators, involves different processes. In this chapter, we discuss about the experimental techniques and methods that have been employed for performing various experiments including the optical resonance studies on the dye doped liquid crystal microdroplets. To begin with, different types of cells in which LC microdroplets are confined are discussed alongside their fabrication and usage. All the processes involving cell preparation, dye doping of the liquid crystal compound, sample preparation, optical polarizing microscopy analysis and optimization of laser optics and the optical set up are discussed in detail.

2.2 Types of cells and their preparation

Liquid crystal microdroplets are usually dispersed in another immiscible or polymer medium and are quite vulnerable to the thermal and the mechanical disturbances. Stabilizing the LC microdroplets is a challenging task. The cells enclosing the film can be made either through capillary action or by using an appropriate spacer. In case of cells made with the help of spacers, one of the important aspects especially for the electro-optic cell with a film containing liquid crystal microdroplets and the polymer is its thickness. In those cells, the electric field required to create the structural distortion in the liquid crystal microdroplets depends on the thickness of the cell. Since all the cells in our experiments bear the analogy of a parallel plate capacitor, therefore the electric field is given as:

$$E = \frac{V}{d} \tag{2.1}$$

E, V and d denote the electric field, applied voltage and the thickness of the cell.

The cell thickness (typically greater than $300\mu\text{m}$) requires larger voltage to initiate field response from the microdroplets. Also, the larger thickness cells add to the scattering and absorption losses as a consequence of larger density of the microdroplets and higher quantity of the supporting medium in the film. Further, larger cell thickness cells promote microdroplet motion upon mild temperature fluctuations. Cells with thickness less than $100\mu\text{m}$, constraint the ease of microdroplet formation as well as filling of the cell. In addition, cells with smaller thickness containing microdroplets are vulnerable to the mechanical damage of the microdroplets at the time of enveloping the cell with a cover slip. From our experience, we found that a spacer between $150-250\mu\text{m}$ thickness is optimum to overcome the shortcomings of microdroplet morphology damage, larger microdroplet density and unwanted motion of the microdroplets. Below we discuss the different types of cells that have been used in the experiments.

2.2.1 Cell for studying liquid crystal texture

The capillary action based cell essentially has a very small thickness. Such cells are used to study the thermotropic texture of the liquid crystal compounds. However, such capillary action based cells are not good for performing the optical experiments with liquid crystal microdroplets. Firstly, these cells do not allow the bigger microdroplets to get into the active area without the cost of any physical damage to their morphology. Secondly, the open ends adhere to the microdroplet motion at elevated temperatures and thus sample spillage. Thirdly, such cells restrict the polydispersity of the microdroplets very strictly. The cell construction is as following:

A glass plate of 0.7 mm thickness is cut into the units of 1.5 cm \times 1.1 cm dimensions. Since the liquid crystals are very sensitive to foreign entities like dirt, grease or oil etc., the glass plates are rigorously cleaned up through a proper protocol involving various steps. Initially, the glass plates are cleaned with detergent and rinsed in order to remove any oily impurities. Next, the baking soda, a mild alkali is applied to the glass plates and each plate is gently rubbed with the help of a bare finger on both sides to ensure scratch free removal of dissoluble impurities like grease and dirt from the glass surfaces. The just washed glass plates are then ultra sonicated in acetone and water alternatively twice for a time period of around 15 minutes each. The second time sonication with water is the end of the cleaning process and the glass plates are transferred one by one from the ultrasonic bath to a pre-cleaned petridish. For the removal of water drops from the glass surface, each glass plate is tangentially flushed with fast flowing nitrogen gas jets. The cleaned glass plates are then stored in a petridish. Next, the glass plates are mounted on a spin coater. Depending on the desired alignment of the liquid crystal molecules, the

glass plates are spin coated either with AL-1254 polyimide for planar alignment or with JALS-204 for homeotropic alignment. To ensure uniform coating, a drop of particular alignment solvent, typically around 100μ l is applied at the center of the glass plate and spread over the surface with the help of a microtip. The greater rpm speed deposits thinner films as compared to lower rpm speed. Soon after the spin coating, the freshly deposited polyimide solutions' hardening by cross-linking of polymer chains on glass plates is achieved by heat curing them at 180 °C in an oven for one hour time period. In case of planar coating, the cured glass plates are rubbed unidirectionally with the help of velvet cloth wrapped on the rotor of the rubbing machine. Finally, two glass plates with antiparallel rubbing direction are stuck together through UV adhesive (NOA-81) mixed with silica beads of specific size. The silica beads together with the mixed adhesive determine the thickness of the cell. The assembled pair is then UV exposed for curing while the silica beads ensure typical cell thickness. The central region of the overlapped glass plates serves as an active area. The liquid crystal sample is then filled into the active area through the capillary action. This constitutes the basic liquid crystal cell for the phase transition studies and the optical texture analysis of a given liquid crystal sample [1,2].

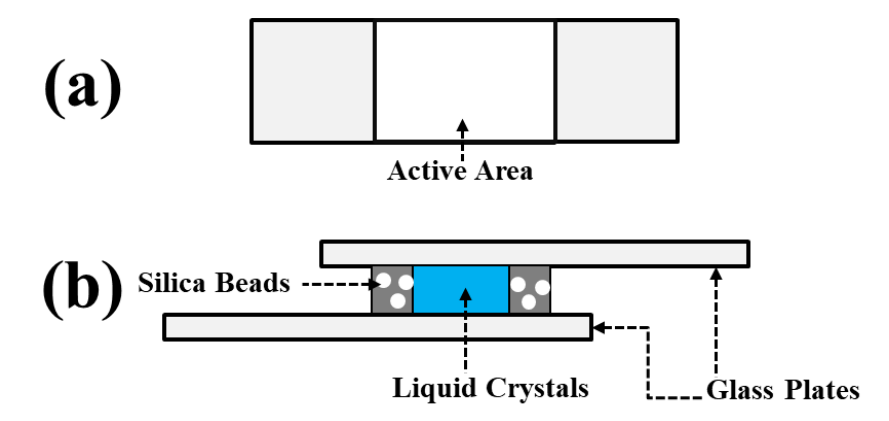


FIGURE 2.1: Schematic diagram of a typical liquid crystal cell used in optical texture study. (a) Top view, and (b) Side view

Figure 2.1 shows a schematic diagram of a commonly used liquid crystal cell. This cell is mostly used to study the textures of liquid crystals and their respective phase transitions. Figure 2.1(a) shows top view of the cell while the Fig. 2.1(b) shows the side view of the cell with blue color representing the filled liquid crystal sample. A standard interference technique involving a high resolution spectrometer (Ocean Optics HR4000CG-UV-NIR) is used to measure the empty cell thickness. A spectrum of the thin air film contained between the two glass plates shows series of interference fringes. The interference of reflected light from the two respective interfaces produces the fringes.

The cell thickness is calculated using the formula:

$$d = \frac{\lambda_m \times \lambda_n}{\lambda_n - \lambda_m} \times \frac{n - m}{2} \tag{2.2}$$

where λ_m and λ_m are m^{th} and n^{th} maxima or minima in the interference spectrum of the cell.

2.2.2 Cell for studying temperature related WGM experiments

This cell consists of a quadrilateral macro-cavity, preferentially square in shape which acts as an active area. It is pruned down out of a double sided tape of 220 μ m thickness which is fixed to one of the two glass plates. To avoid the motion of sample during the experiments, the air channels underneath the tape are closed by pressing the tape firmly. A schematic diagram of a thermo-optic cell is shown in Fig. 2.2. Figure 2.2(a)

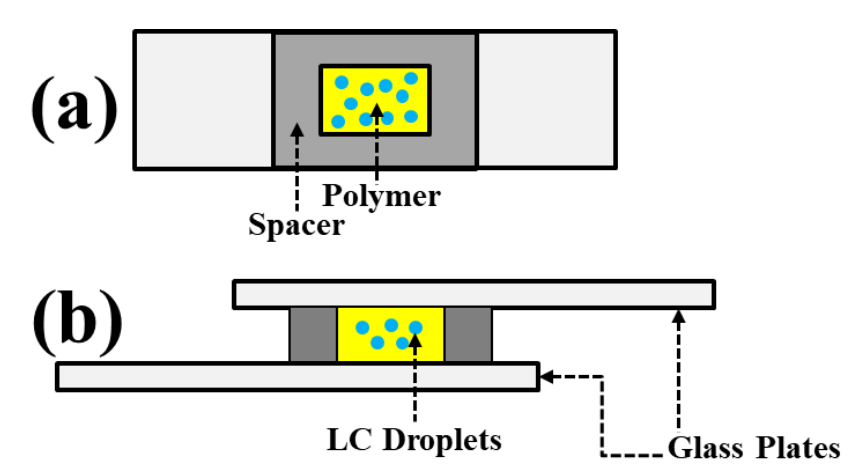


FIGURE 2.2: Schematic diagram of a thermo-optic cell used for temperature based experiments. (a) Top view of the cell, and (b) Side view of the cell.

depicts the top view of the cell while the Fig.2.2(b) shows the side view of the cell. Blue circles represent the LC microdroplets and the yellow region indicates the surrounding polymer medium.

2.2.3 Electro-optic cells

2.2.3.1 Cell with in-plane electrodes

We used a copper tape supplied with adhesive on one side. Stripes of the copper tape of thickness around 60μ m each are placed one over another and are attached to a cleaned glass plate of around 4 cm \times 2 cm dimensions. Usually, 3-4 strips of copper tape are optimum for a standard in-plane field cell. The top stacked copper stripes are painted

with black color in order to hide the lustre of the copper electrodes. Unpainted cell is not only detrimental to the LC microdroplets' survival but it also hinders in their imaging due to the multiple reflections from their lustrous surfaces. Using surgical blade, a very fine and narrow cut is made through the stacked copper stripes and, hence separating them into two parallel copper electrodes. This cut between the electrodes determines the cell thickness and the active area of the cell. The active area is then filled with the polymer dispersed liquid crystal microdroplets and is sealed on the top with a transparent cover slip.

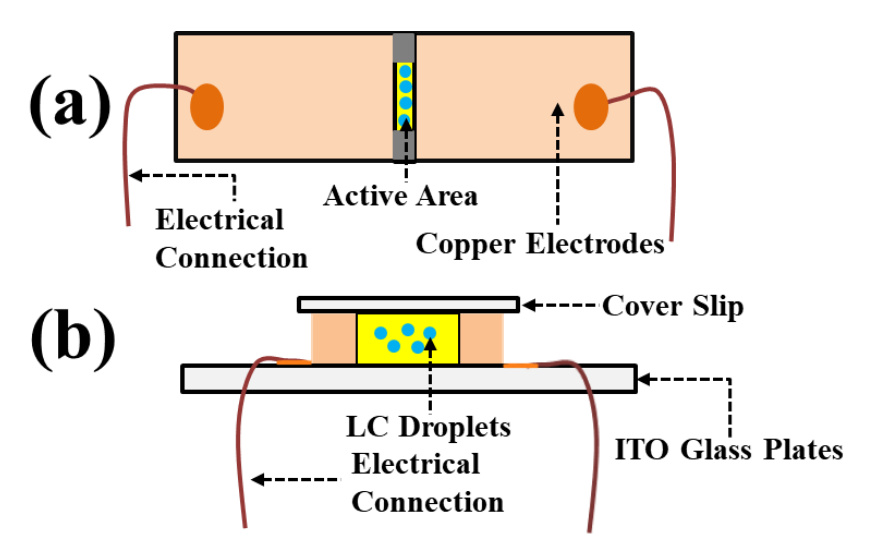


FIGURE 2.3: Schematics of an in-plane field cell. (a) Top view, and (b) Side view

Figure 2.3 shows a schematics of an in-plane field cell. Top view of the cell is shown in Figure 2.3(a), while as the side view of the cell is shown Fig. 2.3(b). Blue colored circles depict LC microdroplets dispersed in the surrounding medium (yellow color).

2.2.3.2 Cell with parallel plate electrodes

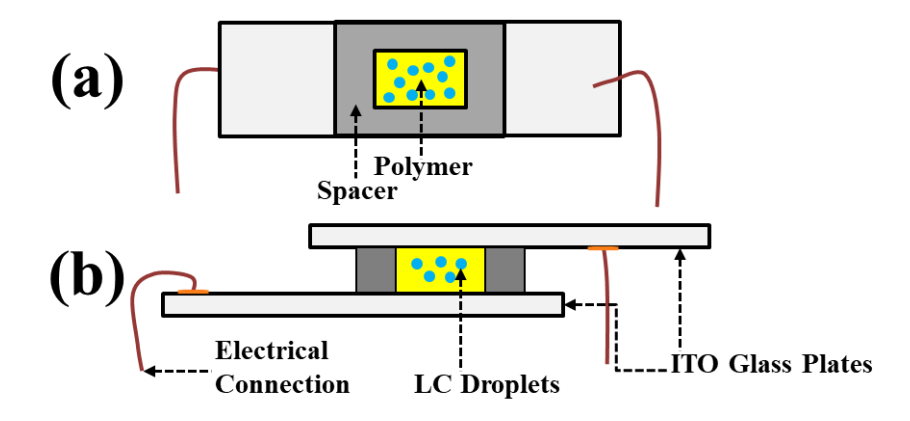


FIGURE 2.4: Schematic diagram of an out of plane field cell. (a) Top view, and (b) Side view

In our experiments, we used glass plates having a coating of around 10Å thickness ITO on them. For the sake of electrical connections, the ITO glass plates are either soldered (Sunbonder USM-IV) with copper wires or else the copper wires are affixed with the conducting surface with the help of the adhesive copper strips. The active area is filled with the polymer dispersed LC microdroplets and sandwiched between the ITO glass plates. Figure 2.4 shows the schematic diagram of a cell with parallel plate electrodes. Fig.2.4(a) shows the top view while the Fig.2.4(b) shows the side view of the cell. Blue circles depict LC microdroplets suspended in the surrounding medium (yellow color). Brown color lines represent the electrical connections.

2.3 Materials used

2.3.1 Liquid crystals

In our work, we have used the calamitic liquid crystals as the material for the optical microcavity fabrication. The optical microcavity cum microdroplets were prepared in nematic, smectic A and smectic C and smectic C* phases. In the experiments, we used 5CB (4-cyano-4'-pentylbiphenyl), 8CB (4-octyl-4-biphenylcarbonitrile), MLC-6608, ferroelectric liquid crystal (FLC) and a pyridine derivative liquid crystal as the building material for the microdroplets [3-6]. For the electrical and thermal tuning of the whispering gallery optical resonance properties, 5CB liquid crystal was used in the experiments [3]. It exhibits 12°C nematic phase with the following phase transitions: Cr 22 °C N 35°C I. It also shows positive dielectric anisotropy ($\epsilon_{\parallel} > \epsilon_{\perp}$). Further 8CB liquid crystal was used to optimise the experimental set up for lasing experiments. 8CB is a positive dielectric anisotropy liquid crystal and it exists in smectic A phase at the room temperature. It shows the following phases: Cr 21.5 °C SmA 33.5°C N 40.5°C I. The molecular structures of 5CB, 8CB and the Pyridine derivative compound that were used in our experiments are given in Fig.2.5(a), Fig.2.5(b) and Fig.2.5(c) respectively.

To address and establish the size stability of the liquid crystal microdroplets, MLC-6608 which is a multicomponent mixture of nematic liquid crystals was used [4]. It possesses negative dielectric anisotropy ($\epsilon_{\parallel} < \epsilon_{\perp}$) and exhibits a very wide range of nematic phase. The phase transitions of the MLC-6608 are: Cr -30°C N 90°C I. For demonstrating electrically switchable lasing, we used a ferroelectric liquid crystal compound named KCFLC7S [5]. Its phase transitions are: Cr 5°C SmC* 73°C SmA* 100.5°C N 114.5°C I, and its room temperature helical pitch is around 2.8 μ m. In order to study the lasing properties across various mesophases of a liquid crystal compound, a pyridine derivative

(a)
$$CH3(CH_2)_3CH_2$$
 CN (b) $CH3(CH_2)_6CH_2$ CN C_5H_{11} CN C_5H_{11} CN

FIGURE 2.5: Molecular structure of (a) 5CB, (b) 8CB and (c) Pyridine derivative liquid crystal compound.

was used [6]. This liquid crystal compound exhibits the following phase transitions: I 68° C N 64.5° C SmA 57.7° C SmC 33.2° C Cr.

2.3.2 Fluorescent dyes

N C C N (a)
$$CH_3$$

$$CH_3$$

$$CH_3$$

$$O$$

$$CH_3$$

$$O$$

$$O$$

$$O$$

FIGURE 2.6: Molecular structure of (a) DCM and, (b)Nile red dye.

Though the liquid crystal based optical microcavities have high q-factors, however, the light coupling via either direct coupling or evanescent wave coupling is not viable easily. The direct laser coupling is found to be ineffective in the case of LC microdroplets. Also, the light coupling with the help of an external coupler like prism or fiber is not possible in case of liquid crystal microdroplets. Hence, in order to sustain the whispering gallery

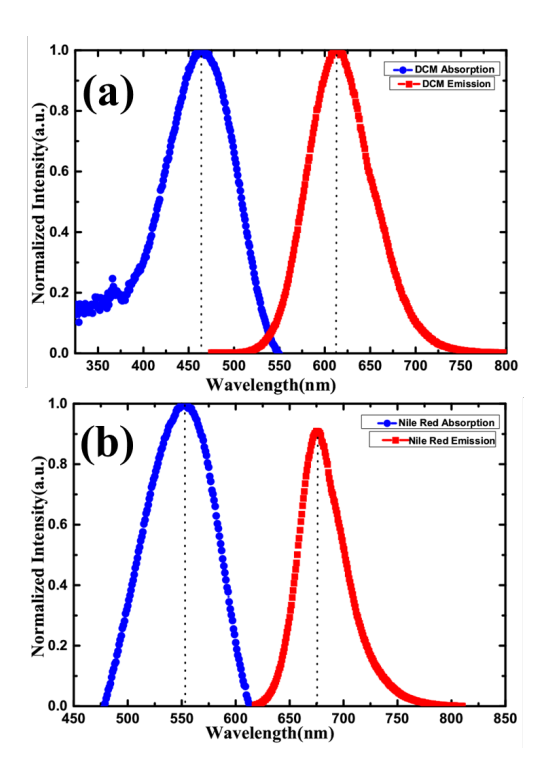


FIGURE 2.7: Absorption and emission spectra of (a) DCM and, (b)Nile red dye. The blue and red curves represent absorption and emission spectra of the two dyes respectively.

modes, the fluorescent light coupling method was employed to trap the light within the microdroplets. In the experiments, we have used 4-dicyanomethylene-2-methyl-6-(p-dimethylaminostyryl)-4H-pyran and 7-dimethylamino-3, 4-benzophenoxazine-2-one commonly known as DCM and Nile Red, respectively as the fluorescent materials. The chemical structures of the two dyes are given in the Fig.2.6(a) and Fig.2.6(b) respectively. Figure 2.7(a) and Fig.2.7(b) shows the absorption and emission profiles of the DCM and Nile red dye respectively. Blue curves indicate normalized absorption intensity spectra while the red curves show the normalized emission intensity spectra. These two dyes were used specially due to their easy solubility in liquid crystals. In addition, we tried using Rhodamine 6G also, but due to its poor solubility with the liquid crystals, it did not serve our purpose effectively. Nile Red is found to be the best dye for fluorescent coupling in LC microdroplets, mainly due to its easy solubility with LCs, resistance to photobleaching, greater quantum yield and non diffusion with the surrounding polymer during the course of the experiments.

(a)
$$F_{3}$$
 F_{4} F_{5} F_{2} F_{2}

FIGURE 2.8: Chemical structure of (a) Polydimethylsiloxane and, (b) Cytop.

2.3.3 Polymers and solutions

The nature of the surrounding polymer or solution plays a crucial role in the ultimate structure of the liquid crystal microdroplets. Hydrophobic interaction between the surrounding medium and the liquid crystal compound plays a crucial role in the formation of radial microdroplets. Figure 2.8(a) and Fig. 2.8(b) shows the chemical structure of the polydimethylsilohexane (PDMS) and poly[perfluoro(4-vinyloxy-1-butene)] commonly known as Cytop [7]. These two polymers were used as supporting media in most of the experiments. As can be seen from the figure, all the chemical bonds in PDMS are not coplanar while as in the Cytop, all the bonds are coplanar. It is found that the LC microdorplets survive for shorter time periods in PDMS than in cytop [9]. Hence, the usage of PDMS was discarded after the procurement of the cytop. Thermotropic liquid crystal molecule generally contains a flexible chain and a rigid core. The flexible chain is non polar and the rigid core may exhibit weak polarity, and as such, much depends on the surrounding medium for their interaction. For instance, if the rigid core of the liquid crystal molecule is negatively charged in nature and the solution is of negative polarity too, upon dispersion, the liquid crystal molecules will tend to repel away from the surrounding solution and in the process different types of droplet configurations are formed [8]. The molecular structure of lecithin is shown in Fig. 2.9. Lecithin is amphiphilic and contains both lipophilic and hydrophilic ends. It is yellowish in appearance. It is mostly extracted from seeds like soya bean and is also present in egg yolk. It is used as a surfactant in glycerol solution. Upon adding around 5 to 10 % of lecithin by weight to the glycerol, radial liquid crystal microdroplets are formed.

 R_1 , R_2 = Fatty acid residues

FIGURE 2.9: Chemical structure of lecithin. The fatty acids are indicated by R_1 and R_2 .

2.4 Polymer dispersed liquid crystals preparation (PDLC)

Polymer dispersed liquid crystal films containing LC microdroplets can be formed in a number of ways. The most general methods for PDLC formation are discussed as following:

2.4.1 Phase separation method

In this process, a single uniform phase of the liquid crystal material mixed with the miscible polymer is formed. Doane and his coworkers has pioneered this phase separation method [8,9]. Once the mixture is formed, many of the methods could be then used to phase separate the uniform film into the liquid crystal rich phase and the polymer rich phase respectively. Some of the methods put forward by Doane alongside their acronyms are listed below:

2.4.1.1 Polymerization induced phase separation (PIPS):

In this process, the liquid crystal compound is mixed with monomer of a particular polymer or oligomers which act as solvents. The liquid crystal material is dissolved in these oligomers. Next, the polymerization of the monomers or oligomers is achieved by virtue of light, heat or radiation. Upon such treatment, the polymer chains start growing and thereby causing the liquid crystal phase to separate while forming a matrix. Temperature, presence of impurities, the solubility and the molecular weight of the starting materials, light intensity in photo cured systems are some of the important

factors that control and affect the phase separation process. Usually, the PIPS process is irreversible.

2.4.1.2 Thermally induced phase separation (TIPS):

In this process, a thermoplastic polymer is melted by heating at high temperatures. Next, the liquid crystal is mixed with the molten polymer. The heated mixture forms a single phase solution. Upon cooling the mixture to the room temperature, the polymer solidifies separating out the liquid crystal phase from the mixture. Rate of cooling determines the microdroplet size. Usually, rapid cooling of the mixture results in smaller size microdroplet formation. If the liquid crystal material and the polymer have mutual solubility at higher temperature, such PDLCs can not be used.

2.4.1.3 Solvent-induced phase separation (SIPS):

As the name indicates, the solvent induces the phase separation. Here, the liquid crystal compound and a polymer are mixed with a third party organic solvent. In this way, a single phase mixture is obtained. The role of the solvent is to solubilize both the thermoplastic polymer and the liquid crystal. Once the solvent evaporation initiates, the separation of the liquid crystal and the polymer takes place and in the process, the liquid crystal microdroplets are formed in the polymer matrix. The rate at which the solvent evaporation takes place determines the liquid crystal microdroplet size.

These methods of phase separation discussed above are undesirable in our experiments as they often lead to various unwanted microdroplet morphologies which are often unfit for the optical experiments. Depending on the nature of the polymer type, polymer concentration and the kind of phase separation process utilized in the PDLC preparation, various morphologies of the liquid crystal microdroplet are formed. The breakage of the microdroplets as a result of constant shrinkage of the polymer chains renders them unfit as optical microcavities. Further, this method yields unwantedly and uncontrollably larger number of microdroplets in the PDLC that actually hinder in the reflection and transmission of the excited WGMs emanating from an illuminated microdroplet owing to the scattering and absorption losses to the modes. As a result of higher probability of microdroplet breakage, larger number density of microdroplets, uncontrolled scattering and absorption losses, we switched over to the emulsion methods to better address those issues.

2.4.2 Emulsion method:

This method is employed in the cases where the liquid crystal material and the aqueous solution forming the polymer are immiscible to each other. In this process, the liquid crystal microdroplets are dispersed into the polymer. This PDLC film is allowed to dry. Subsequently a solid phase of polymer is formed. This solid phase not only contains the liquid crystal microdroplets but also supports the microdroplets dispersed in it. However, as the film undergoes drying process, significant change in volume of the film occurs. Consequently, this shrinkage causes deformation of the microdroplets from spherical morphology in the solution to the oblate spheroids in the solidified PDLC film. Subsequently, the typical alignment of the LC molecules gets disturbed and may result in change in the optical resonance properties of the microdroplets. In most of our works, we employed emulsion method with some vital modifications in order to serve our experimental requirements.

In the modified emulsion method, the LC microdroplet formation is performed either in the microcentrifuge tube of 1.5μ l or in the active area of a typical cell. In the former case, around tens of thousands of micro liters of the polymer or else a suitable solution is transferred into a centrifuge tube. Next, around 10-20 micro liters of the dye doped liquid crystal with the help of a fine tip of micropipette is dispersed into the polymer manually. At the time of dispersing the liquid crystals, simultaneous and irregular motions of the micro tip are made into the centrifuge tube that gives rise to well spaced microdroplet formation across the polymer. However, it is worth notable that the rate at which the micro tip motions and the liquid crystal release is made, determines the polydispersity of the liquid crystal microdroplets. As a matter of fact, for fixed liquid crystal sample release rate, slow micro tip motion yields bigger droplets while the faster motion yields smaller droplets. Next, with the help of a sterilized spatula a small volume of the PDLC (roughly around 1000 micro liters) is transferred into the active area of the cell. The cell is either closed with a cover slip for temperature based experiments or else with an ITO glass plate for electric field related experiments. In the latter case, to avoid the sample wastage, for instance Cytop, an optimized volume of the Cytop solution is poured into the active area. Next, 1-2 microliters of dye doped liquid crystal is then directly dispersed into the solution with the help of the micropipette while following the non repeating circular motions of the tip during the liquid crystal release.

A diagram showing the LC microdroplet formation through this method is shown in Fig.2.10. A controlled quantity of polymer or solution (shown yellow) is taken in a spatula near a heater containing the liquid crystal compound and maintained preferably at its isotropic temperature. Unlike the other PDLC methods, this modified emulsion



FIGURE 2.10: Droplet making through micropipette injection

method is most suitable for our experiments. This method yields liquid crystal microdroplets that are very well spaced from each other and also the microdroplets are not in queue to shield and add to scattering and absorption losses of the WGMs. The disadvantage of this method is that it yields LC microdroplets of non uniform size. Since we study a single LC microdroplet in the whole experiment, we search and select the desired size microdroplet and thus the method works fine in our experimental studies.

2.5 Microscopic observation of the PDLC

In this section of the chapter, we discuss the characterization of the liquid crystal microdroplets dispersed in the dispersing medium through the optical polarizing microscopy. For the room temperature liquid crystal compounds, the cell containing liquid crystal microdroplets is directly mounted on the microscope stage of an optical polarizing microscope. The optical polarizing microscope allows an additional insertion of lambda plate between the crossed polarizers and is also fitted with a camera for recording the optical micrographs. However, for the above room temperature experimental studies especially in case of liquid crystals exhibiting multiple mesophases, the LC cell containing PDLC, is mounted inside the hot stage of a temperature controller. Next the temperature controller is mounted on the microscope stage and subsequently the temperature is raised to the desired liquid crystalline phase of the sample in order to analyze the liquid crystal microdroplets.

2.5.1 Optical polarizing microscopy (OPM)

A direct look on the OPM images of the microdroplets reveals the type of anchoring that the dispersing medium enforces on the LC molecules. In case of homeotropic anchoring medium, microdroplets with hedge-hog point defect is found right at the centre as a consequence of radial director. The presence of four extinction brushes verifies the radial order of the calamitic liquid crystal director. Due to homogeneous anchoring medium like water, glycerol, etc., the LC microdroplets are found to exhibit bipolar defects located diametrically opposite to eachother.

2.5.2 Lambda plate imaging

In the experiments with the LC microdroplets, we basically try to visualize the effect of change in liquid crystal director with respect to the temperature and electric field. To find the director orientation in the liquid crystal microdroplets, we make use of retardation plate or lambda plate (530nm). A retardation plate when inserted in the path of a polarized light beam resolves it into two orthogonal components. As the name retardation suggests, it induces a relative retardation in the phase of one component relative to the other. During the transmission of the two components, it recombines them into a single beam having different polarization characteristics from that of the original light beam. Consequently, a ray of polarized light passing through such anisotropic materials faces different refractive index in different directions of propagation and polarization orientations. Figure 2.11 shows the working of the first order retardation plate. As seen in the Fig. 2.11 (a), when the first order wave plate is inserted in the optical path of the linearly polarized beam such that its orientation is 45° with respect to the analyzer and the polarizer each, it introduces a fixed optical path difference between 530-560nm region to all the ordinary and extra ordinary wavefronts passing through it. This optical path difference does not alter the polarization characteristic of green component

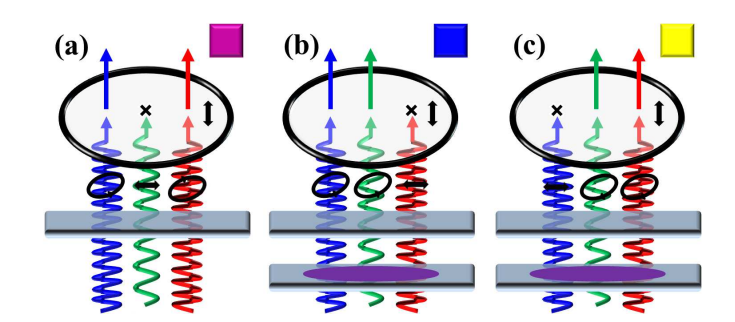


FIGURE 2.11: Effect of the retardation plate on the polarized white light passing through it.(a) When no sample is placed in the optical path. (b,c) When the sample is added in the optical path with the ellipsoidal wave front parallel and perpendicular to the retardation plate respectively.

and as such gets blocked by the analyzer which is placed perpendicular to the polarizer. Simultaneously, the rest of the wave fronts are able to pass their respective component vectors through the analyzer. As per the colour mixing rules, when the green colour is subtracted from the white light, the resulting light that emerges out is bright magentared colour. In the similar way, as shown in Fig.2.11 (b) and Fig.2.11 (c) with ellipsoidal wavefront when the fixed optical path differences are added to the red and blue colours respectively, the emerged light that results are blue and yellow respectively. In the experiments, the outcome colour of the microdroplet under retardation plate is a consequence of director distortion. Wherever the director is radially parallel to the polarizer, the bright magenta colour is observed. However, if the director is tilted clockwise or anticlockwise with respect to the fast-axis of the full wave retardation plate, blue and yellow colours are observed in those regions of a microdroplet. Figure 2.12 shows the relationship between the observed colours of a microdroplet under full wave retardation plate and the director orientation. In the case of LC microdroplets, the bright magenta colour corresponds to either perpendicular or parallel orientation of the director in a plane. However, the yellowish and the bluish colours in the liquid crystals indicate the anticlockwise and the clockwise rotation of the liquid crystal director respectively [10,11].

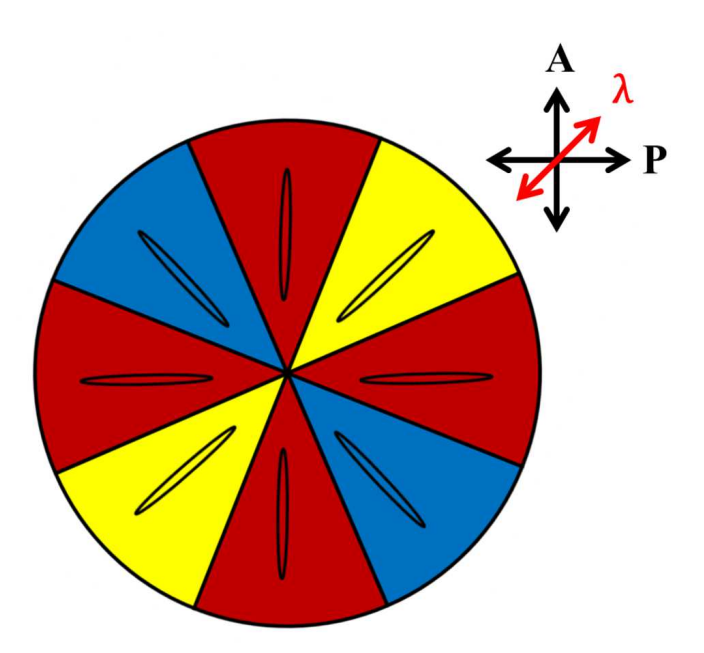


FIGURE 2.12: Identification of the liquid crystal director orientation from the observed colors under optical polarizing microscope with an inserted retardation plate. Red arrow shows the fast axis of the retardation plate.

2.6 Optical set-up

The optical set up is mainly constituted of inverted polarizing microscope, a high resolution spectrometer and a pair of lasers aligned through optical circuit involving beam expander assembly, intensity attenuator, variable round aperture and flip mirror. The schematic diagram of the whole optical set up that was used in the experiments is shown in Fig. 2.13, while as the actual view of the experimental setup is shown in Fig. 2.14.

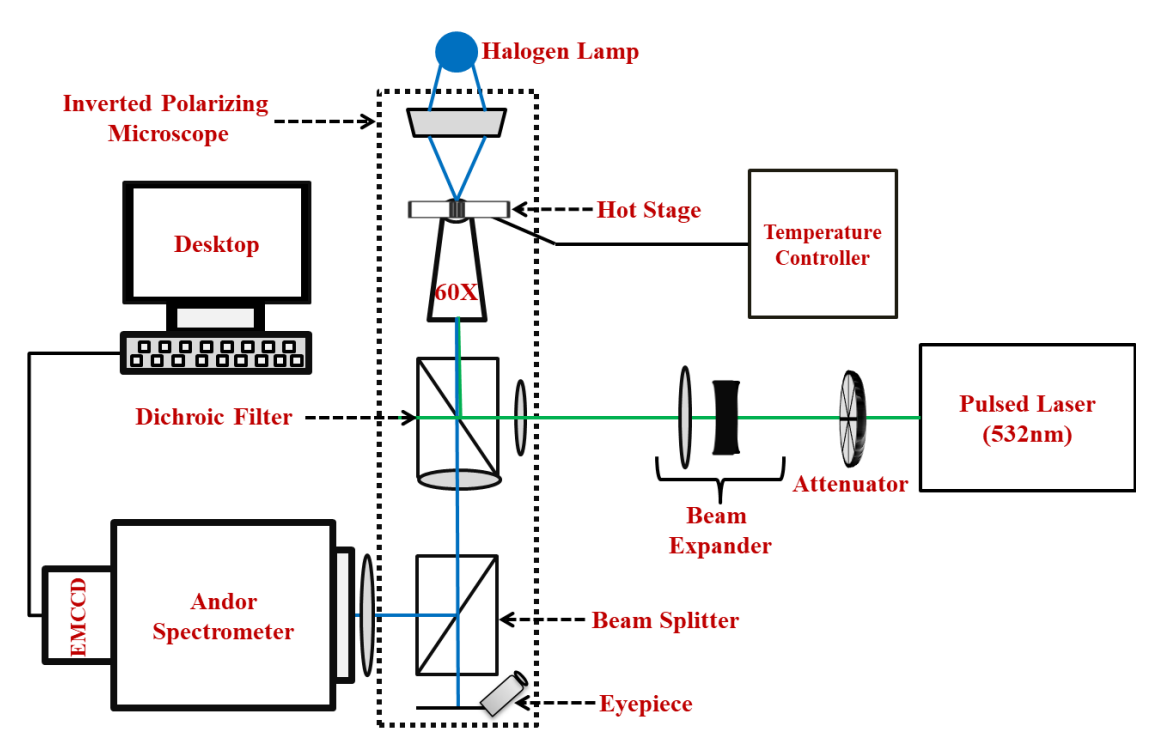


FIGURE 2.13: Schematic diagram of the experimental set up used in the laboratory.

An inverted polarizing microscope (Nikon Eclipse Ti-U) is used. This inverted polarizing microscope is equipped with a halogen lamp as light source, two polarizers, microscope sample stage and multiple ports for connecting cameras and spectrometer. The sample is illuminated by the halogen lamp in transmission mode with the lamp located on the top and the sample mounted on the xyz motorized stage (Prior optiscan) above the objective. With the help of the joystick, the stage can be used for the precise control of the sample movement in the focal plane. We used a water immersion objective with the magnification of 60X, numerical aperture NA = 1 and working distance WD = 2.8mm in our experiments. As an essential part of the beam focusing, the back aperture of the objective lens is filled to the maximum. The microscope bears two ports on the left side and the one on the lower right side (see Fig. 2.14). Out of the two left side ports, the lower left side port is connected with the high resolution Andor Spectrometer and the other left side port is connected to the color camera (Nikon, Eclipse Ti-U). The spectrometer is supplied with three different gratings. The gratings are 2400 lines/mm,

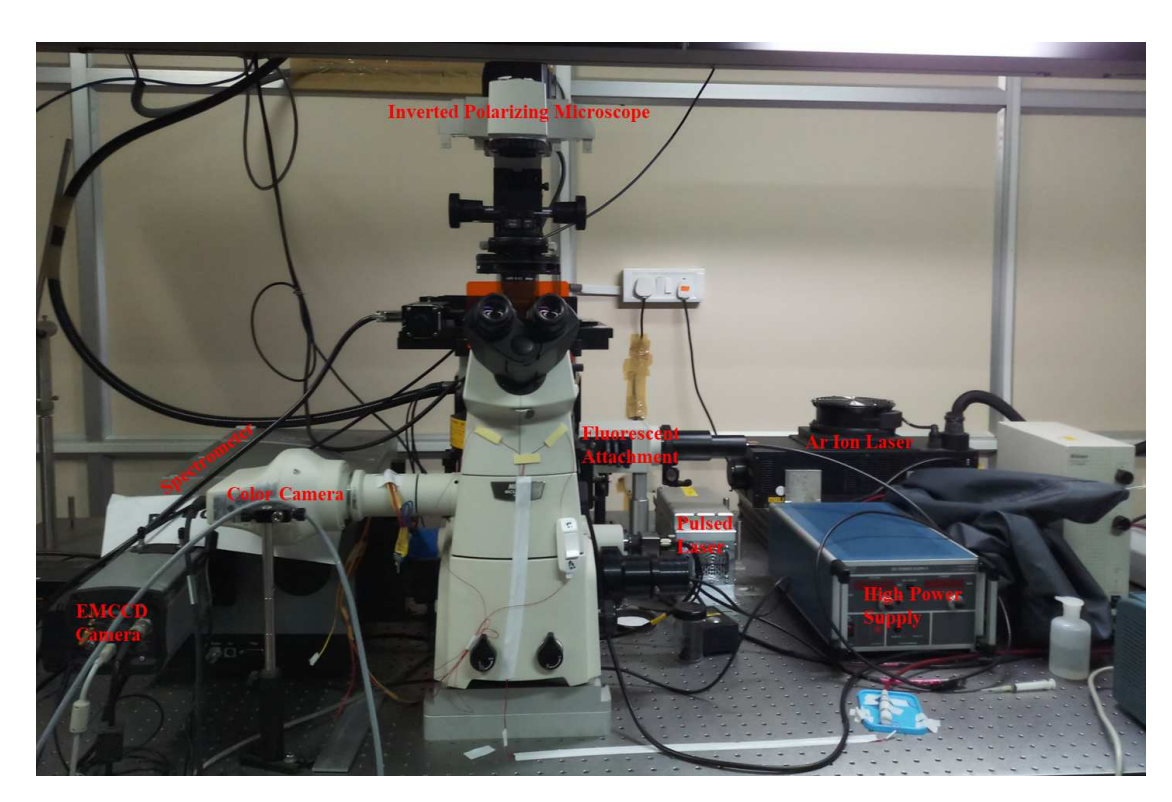


FIGURE 2.14: Experimental set up used for the whispering gallery optical resonance experiments. The red captions label the essential instruments of the set up.

1200 lines/mm and 300 lines/mm respectively. Since the resolution of a grating depends inversely on the number of lines, each grating has different resolution. Among these gratings, for a fixed central wavelength of 550nm, the 2400 lines/mm grating has the highest spectral resolution of 0.02nm. The 300 lines/mm grating has the least spectral resolution of 0.2nm. The grating with 1200 lines/mm has 0.06nm spectral resolution. The laser light is used to induce fluorescence in an isolated and focused dye doped microdroplet. The excited WGMs emanating from the illuminated microdroplet are sent back through the reflection by the glass cell into the spectrometer for recording the spectrum. The Nikon camera attached to the microscope is connected with the desktop through a suitable adapter and is operable under the NIS software. Through manual zooming in and precise focusing, good images and videos are recorded and are saved on the desktop. This software is pre-calibrated for different objective lenses to minimize the measurement errors. The lower right side port of the microscope is meant for the high speed CCD camera connection, which is linked with the optical tweezer. This camera and the optical tweezer were not used in any of our experiments. On the optical table, right side to the microscope is a pair of lasers. Black colored assembly is a tunable Argon ion continuous wave laser. The small steel box as shown on the right side of the microscope is that of Q-switched double pulsed laser of 532nm wavelength (Teem Photonics, Model: PNG-M02010–130). The pulse width of the pulsed laser is 400ps. At a time, the laser light from one of the lasers is made to pass through the common optical path via flip mirror. In order to fine tune the beam spot size and control the intensity of the laser beam, the laser light is made to pass through a round beam aperture and intensity attenuator respectively, before entering into the beam expander assembly. The beam expander is employed to expand the laser beam spot such that the back aperture of the objective lens is illuminated completely with the laser beam. The light from both the continuous laser and the pulsed laser finally enters into the objective lens via back port with the help of multiple inclined mirrors.

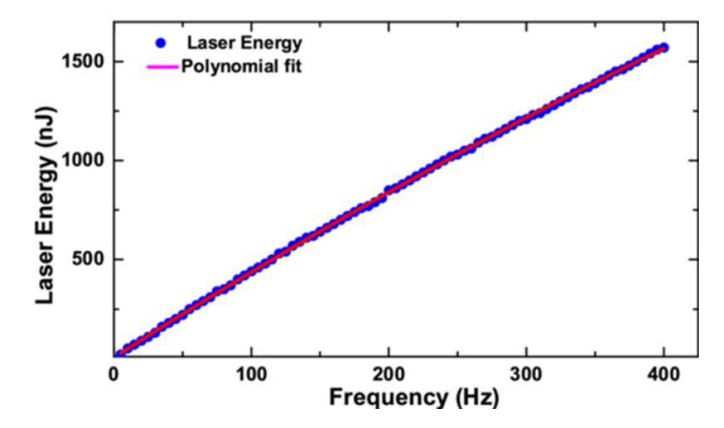


FIGURE 2.15: Laser output energy characteristics of the used pulsed laser as a function of frequency.

Figure 2.15 shows the out put calibration of laser energy of the pulsed laser used in the WGM lasing experiments. It shows the output energy of the laser pulses as a function of frequency just at the exit from the objective lens. Blue colored circles represent measured energy values at the objective lens while as, the red line is the best polynomial fit to the equation:

$$y = a + b_1 x + b_2 x^2 (2.3)$$

where a, b_1 and b_2 are constants and are 5.29981, 4.4473 and -0.00137 respectively. The variable x is the external triggering frequency.

2.7 Polarization set-up and analysis of WGM polarization

In order to characterize the polarization of the excited whispering gallery modes, a pair of additional analyzers was used in the experiments. One analyzer was fixed inbetween the spectrometer and the microscope port while as the other analyzer was fixed in the path of the exciting laser beam. Figure 2.16 shows the actual and schematic arrangement of the analyzer in the set up. With the help of these two analyzers, the state of polarization recorded by the spectrometer could be altered in four possible configurations. Figure 2.17 shows the set of WGMs recorded for a microdroplet of $20\mu m$

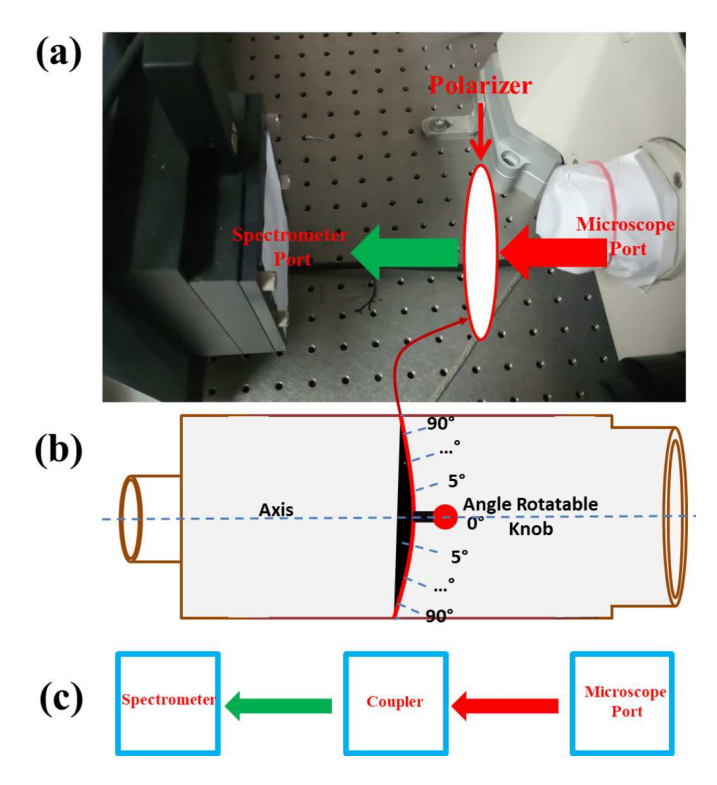


FIGURE 2.16: Experimental set up for polarization identification of WGMs: (a) Actual location for the light coupling in the experimental set up. (b) Schematic diagram of rotator analyzer, and (c) Schematic diagram showing the role of light coupler (analyzer) for WGMs transmission from microscope into the spectrometer. Thick red and green arrows depict different polarization light.

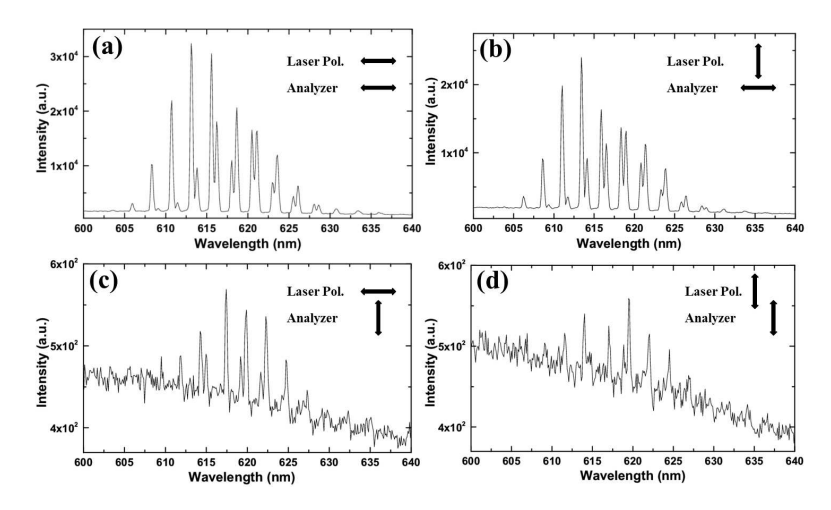


FIGURE 2.17: Polarization characterization of WGMs observed from a nematic droplet of 20.2 μm at room temperature. WGMs observed when (a) The laser polarization and analyzer axis are parallel to eachother but perpendicular to the droplet surface. (b) The laser polarization is made perpendicular to the analyzer axis in (a) configuration. (c) The analyzer axis is made perpendicular to the laser polarization of (a) configuration, and (d) Both the laser polarization and the analyzer axis are made parallel to each other and tangential to the droplet surface.

in different polarizer-analyzer configurations. When the poalrization of the excitation laser was changed parallel to the analyzer but perpendicular to the droplet surface, the

highest intensity TM modes are recorded (see Fig. 2.17 (a)). When the laser polarization is made perpendicular to the analyzer, small decrease in the intensity of the WGMs is observed (see Fig. 2.17 (b)). However, when the laser polarization is kept perpendicular to the droplet surface but the analyzer is fixed perpendicular to the laser polarization, a drastic reduction in the intensity of the modes is observed in Fig. 2.17 (c). Also, many modes disappear from the spectrum. When both the laser polarization and analyzer axis are set parallel to eachother and also parallel to the droplet surface, the least intensity TE modes are observed as shown in Fig. 2.17 (d). It is observed that for most of the liquid crystal microdroplets with diameter size $d \leq 15~\mu\text{m}$, the 2.17(c) and 2.17(d) configurations display almost no or very weak intensity WGMs.

Bibliography

- [1] Paladugu Sathyanarayana, Investigation on the Physical Properties of Unconventional Nematic Liquid Crystals., PhD Dissertation, University of Hyderabad, India (2012).
- [2] Zuhail K. P., Topological Defects Transformation and Structural Transition of Two Dimensional Colloidal Crystals across Nematic to Smectic-A Phase transition., PhD Dissertation, University of Hyderabad, India, (2017).
- [3] J. A. Sofi, M. A. Mohiddon, N. Dutta and S. Dhara, Phys. Rev. E, 96, 022702, 477, (2017).
- [4] J. A. Sofi, and S. Dhara, Liq. Cryst., 46, 4, 629-639, 477, (2018).
- [5] J. A. Sofi, and S. Dhara, Appl. Phys. Lett., 114, 091106 (2019).
- [6] J. A. Sofi, A. Barthakur and S. Dhara, Soft Matter, 15, 7832-7837, (2019).
- [7] M. V. Rasna, K. P. Zuhail, R. Manda, P. Paik, W. Haase and S. Dhara, Phys. Rev. E, 89, 052503, (2014).
- [8] P. S. Drzaic, *Liquid Crystal Dispersions*, World Scientific Publishing: Singapore, (1995).
- [9] J. W. Doane, N. A. Vaz, B.G. Wu and S. Zumer, Appl. Phys. Lett., 48, 269-71, (1986).
- [10] U. Tkalec, M. Škarabot, I. Muševič, Soft Matter, 4, 2402, (2008).
- [11] I. Muševič, Liquid Crystal Colloids, Springer: Cham, Switzerland, (2017).

Chapter 3

Electrical and thermal tuning of quality factor and free spectral range of optical resonance of nematic liquid crystal microdroplets

3.1 Introduction

Solid dielectric based spherical microresonators have large quality factor. They are very rigid and it is difficult to tune the WGM optical resonance emanating from them by means of external fields such as electric or magnetic [1-14]. In this context liquid crystal based microresonators have drawn significant attention. Humar et al., first reported the WGM resonance in nematic liquid crystal microdroplets [15]. Kumar et al., showed that the WGM resonance can be a diagnostic tool for detecting subtle phase transition in liquid crystals [16]. Thermal applications based on the WGMs of the cholesteric liquid crystal microdroplets have been reported by Wang et al. [17]. We have shown the effect of magnetic field on the structure of the ferromagnetic nematic liquid crystal microdroplets [18].

In this chapter, we present the experimental findings on the effect of electric field and temperature on the optical resonance properties viz. quality factor (q-factor) and free spectral range (FSR) of an LC optical microcavity in the form of a spherical LC microdroplet.

3.2 Experimental

We used 5CB liquid crystal compound obtained from Sigma-Aldrich. It exhibits the following phase transitions: Cr 23.65°C N 33.5°C I. It shows positive dielectric anisotropy and positive birefringence. The LC microdroplets were suspended in Polydimethylsiloxane by using a micropipette through modified emulsion method (Sec. 2.2, Chapter 2). PDMS is a visco-elastic polymer with a refractive index of 1.43. Prior to the droplet formation, a small quantity (2 wt%) of DCM fluorescent dye was doped into the liquid crystal compound. The LC-polymer mixture containing polydisperse microdroplets is confined between two indium-tin-oxide (ITO) coated glass plates (Sec. 2.2.3.2). Microdroplets of desired size were excited with a focused laser light of wavelength 532 nm (Nd:YAG second Harmonic). The absorption peak of the DCM dye coincides with the wavelength of the laser light (see Fig. 2.7 in chapter 2) and thus fluorescence is emitted by the DCM dye molecules upon laser excitation. Over laser light exposure of the dye doped microdroplet causes fluorescence to inhibit. Also the constant local heating of the microdroplet caused by the laser beam was found to cause unwanted deformation to the microdroplet morphology. Such deformations cause inhomogeneity of the refractive index of the microdroplet. Consequently, the resonance condition is compromised because of which the light leaks out of the microcavity. All the WGM experiments presented in this chapter were conducted using scanning near-field optical microscope (WiTec, Alpha-200) fitted with a spectrometer at Centre for Nanotechnology. The minimum spectral resolution of the spectrometer is 0.09 nm. The schematic diagram of the experimental setup is shown in Fig. 3.1. To study the effect of electric field, a sinusoidal voltage

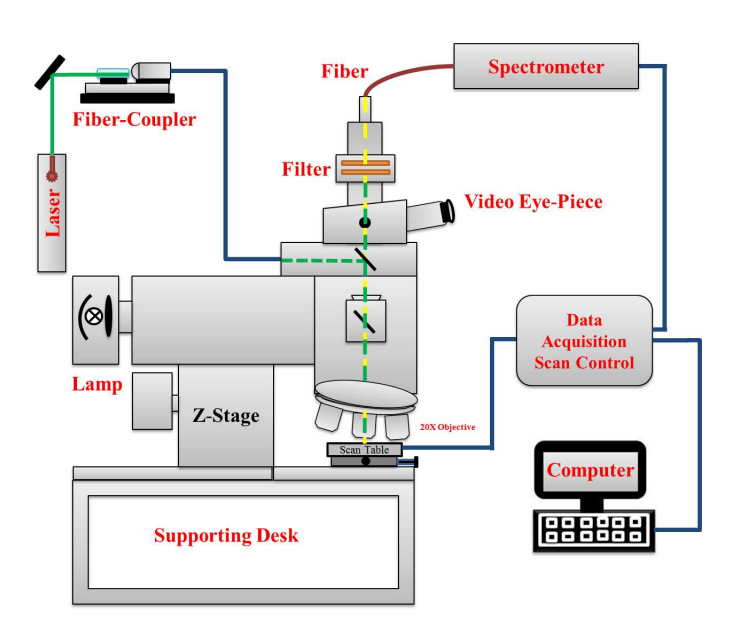


FIGURE 3.1: Schematic diagram of the scanning near-field optical microscope (SNOM) setup.

was applied across the cell with the help of a function generator (Tektronix-AFG 3102) connected to a voltage amplifier (TEGAM-2350). The sinusoidal voltage was applied at a fixed frequency of 5kHz. A temperature controller (Instec Inc., mk1000) with the temperature accuracy of 0.01°C was used to vary the sample temperature.

3.3 Results and discussion

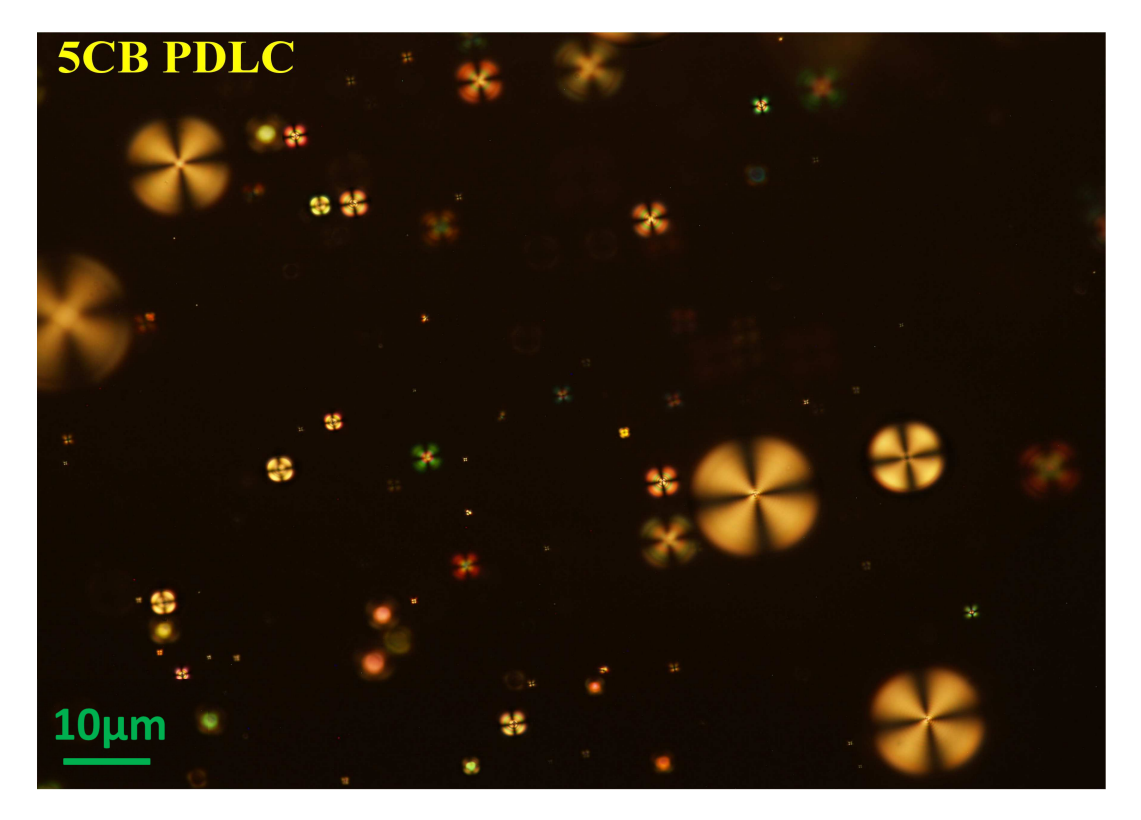


FIGURE 3.2: Polarising optical micrograph showing suspended microdroplets of 5CB liquid crystal in PDMS at room temperature.

A polarized optical micrograph of PDMS film with 5CB liquid crystal is shown in Fig. 3.2. The film is of 220μ m thickness. A large number of spherical microdroplets with various size are formed as can be seen in the Fig. 3.2. Some of the microdroplets are seen out of the focus in the figure. Figure 3.3(a) shows an isolated microdroplet under polarizing optical microscope across a fixed plane of observation. As evident, the colorful rings appear due to the varying optical retardation from the center to the periphery. The colorful concentric rings reveal spherical symmetry of the microdroplets. Four extinction brushes originating from the centre of each microdroplet are oriented along the polarizer axes. The appearance of extinction brushes is a consequence of incident light polarization being parallel or perpendicular to the local optic axis. This suggests that

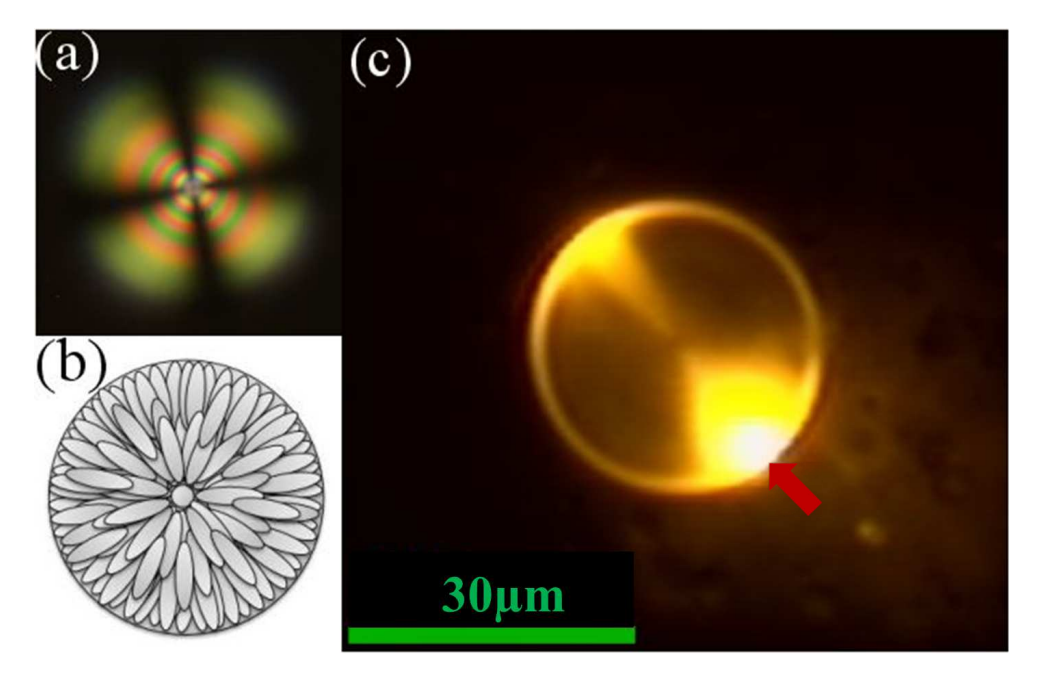


FIGURE 3.3: (a) Polarising optical micrograph of a 5CB microdroplet. (b) Schematic diagram showing the molecular orientation inside the microdroplet. Small ellipsoids represent the molecules of the 5CB liquid crytsal compound while the dot at the centre of the sphere show the central point defect. (c) A DCM dye doped microdroplet illuminated by a focused laser beam (λ =532nm). The red arrow indicates the irradiation point.

the director is radially symmetric and the long molecular axes are orthogonal to the liquid crystal-PDMS interface. Figure 3.3(b) shows the schematic diagram of the director orientation in the microdroplet with a radial hedgehog defect at the center. We focused on an isolated microdroplet and excited it with the laser light (532 nm) of fixed energy just inside the polymer-liquid crystal microdroplet interface as the resonant modes are formed inside. The irradiation point is indicated by a red arrow in Fig. 3.3(c). The dye molecules emit fluorescence and a thin light ring around the circumference of the microdroplet is observed. The appearance of this thin light ring demonstrate the excitation of the WGMs within the microdroplet. The DCM dye molecules do not diffuse into the surrounding polymer during the course of the experiment. The restricted fluorescence within the microdroplet further suggests and validates that the dye molecules are not diffused across the interface as there is no excited fluorescence outside the illuminated microdroplet's periphery. The emitted light from the microdroplet is collected by the same objective through reflection mode and is sent to the spectrometer through dichroic lens fitted into the optical path within the optical polarizing microscope. Figure 3.4(a) shows the characteristic resonance spectra obtained from a microdroplet at two different temperatures. The spectrum drawn with black color is at 27.5°C while the red color drawn spectrum is recorded at 30.5°C. From the spectra, one can clearly see the shifting of the WGM at the two respective temperatures. This shifting indicates

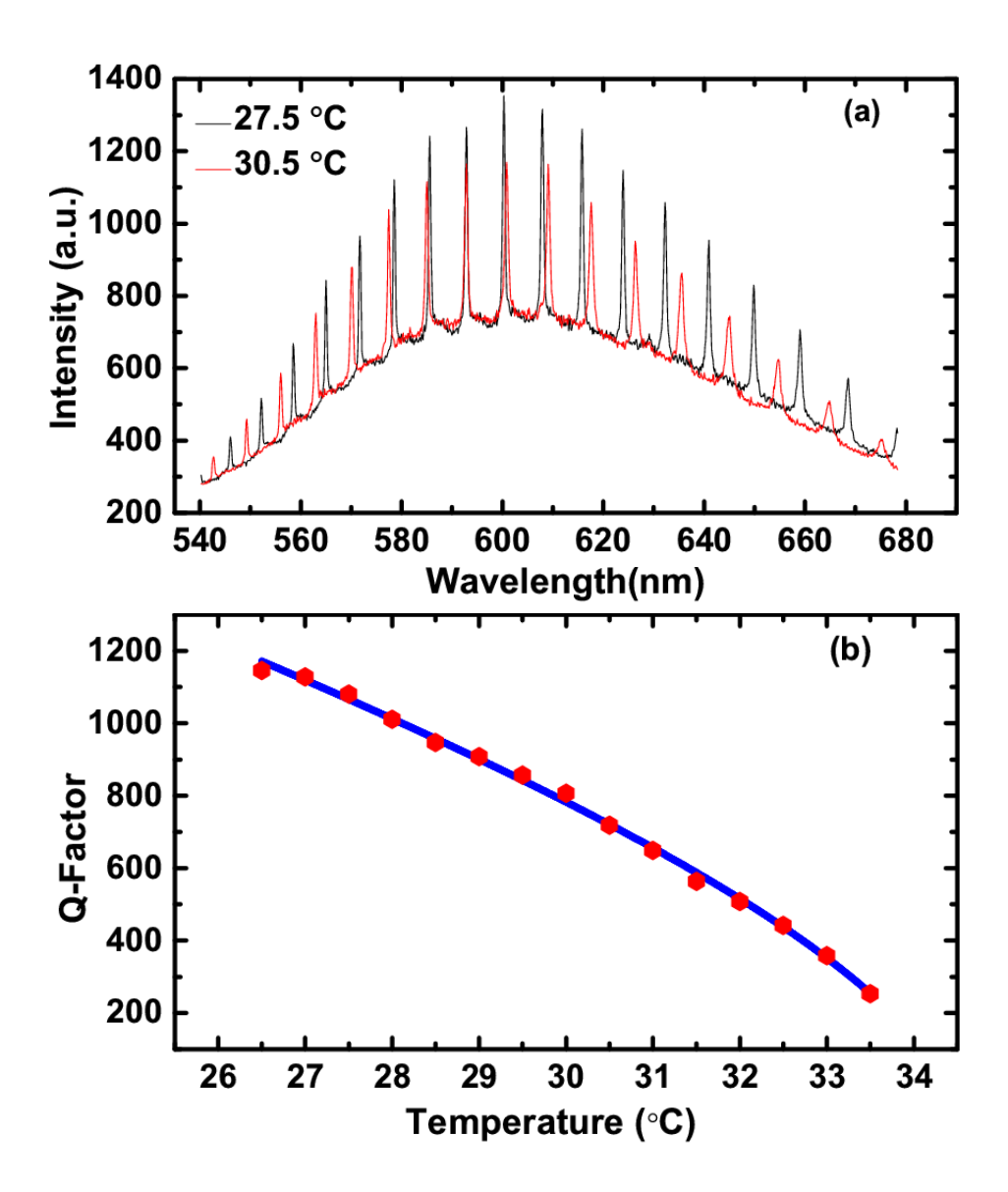


FIGURE 3.4: (a) Representative WGM spectra recorded at two different temperatures namely, at 27.5°C (Black) and 30.5°C (Red). (b) Variation of Q-factor with temperature for the mode with the highest intensity. The continuous line is the best fit to Eqn.(3.5). Droplet diameter: 9μ m.

thermal sensing application of the microdroplets by virtue of WGM optical resonance. Further, it is observed that the peak intensity of the modes is decreased and the full-width half-maxima is increased with the temperature. The separation between any two consecutive modes is also increased at higher temperatures. Liquid crystals being bire-fringent possess different refractive indices (ordinary and the extraordinary) for different polarizations of the light (section 1.5). Hence, the TE mode senses the ordinary (n_o) and TM mode senses the extraordinary (n_e) refractive indices. 5CB is a positive bire-fringement liquid crystal compound with $n_e > n_o$ and they show opposite temperature

dependence i.e. n_e decreases whereas n_o increases as the temperature is increased towards the isotropic-nematic phase transition. On the other hand, due to the negligible change in the refractive indicx of PDMS with temperature, especially for around 5-6°C range, it remains constant and is reported to be $(n_s = 1.43)$ at the room temperature. For a smaller microdroplet size (diameter $< 15\mu$ m), it can be shown that only TM modes with radial mode number q = 1 are supported [15,19].

To characterize the resonance spectra quantitatively, we measured the Q-factor as a function of temperature from the resonance linewidth of the mode with the highest intensity. It is given by

$$Q = \lambda/\Delta\lambda \tag{3.1}$$

where $\Delta \lambda$ is the full-width half maxima corresponding to the resonant wavelength λ .

Figure 3.4(b) shows the variation of Q-factor as a function of temperature. The Q-factor at room temperature is large (1150) and decreases rapidly as the temperature is increased towards the nematic-isotropic phase transition. The lower value of Q-factor is mainly attributed to the resolution limit of the spectrometer used in the SNOM set up. For a spherical liquid crystal microresonator, the Q-factor can be expressed as [15,20]:

$$1/Q_{tot} = 1/Q_{mat} + 1/Q_{rad} + 1/Q_{LC} + 1/Q_{ss} + 1/Q_{coupling}$$
(3.2)

where Q_{mat} refers to the intrinsic material loss due to the absorption and scattering in the dielectric medium of the resonator. It is given by

$$Q_{mat} = 2\pi n_r / \lambda \alpha_{mat} \tag{3.3}$$

where α_{mat} is the absorption decay constant and n_r is the refractive index of the resonator. The radiation loss Q_{rad} is due to the curvature of the spherical microcavity. Q_{ss} refers to the surface scattering loss due to either roughness or impurities, Q_{LC} refers to the loss due to the thermal fluctuations of the director and $Q_{coupling}$ refers to the optical losses involved in light coupling into the external optical devices like prism, fibre, etc. The contribution of the intrinsic material loss Q_{mat} is directly proportional to the refractive index of the resonator and hence strongly depends on the temperature. The loss (Q_{LC}) due to the thermal fluctuations of the director is also expected to increase slightly with increasing temperature. Since the size of the microdroplet is very small and it supports only TM modes corresponding to the radial mode number q = 1, we consider, $n_r \simeq n_e$. The temperature dependence of n_e is given by:

$$n_e = A_e - B_e T - C_e (1 - T/T_c)^{\beta}$$
(3.4)

Where A_e , B_e , C_e and β are constants and T_c is the isotropic to nematic phase transition temperature of the liquid crystal. The exponent β is about 0.2 for 5CB [21]. Assuming the major contribution to the temperature variation of Q comes from Q_{mat} , we can write:

$$Q \approx A - BT - C \left(1 - \frac{T}{T_c}\right)^{\beta} \tag{3.5}$$

The fitting of the Q-factor with the temperature is shown in Fig. 3.4(b). The fit parameters obtained from the best fit are: A = 19776, B = 67, C = 3129 and $\beta = 0.2$. Interestingly, the value of exponent (β) is comparable to the exponent of the temperature dependence of the extraordinary refractive index of 5CB [21]. It further confirms that the major contribution to the temperature dependence of Q comes from the change of extraordinary refractive index. While the excitation energy of the continuous laser beam is at fixed value, we also note that a very small change in the extraordinary refractive index can give rise to substantial change in the Q-factor (e.g., $\Delta n_e/\Delta Q \sim 3 \times 10^{-5}$ at room temperature).

We further studied the effect of a sinusoidal electric field on the Q-factor of the WGM optical resonance. The electric field creates elastic distortion of the director in the microdroplets beyond a particular value [15,22-24]. The typical distortions of the director with normal boundary condition at zero, low and high electric fields are shown schematically in Fig. 3.5. The change in the internal structure is expected to reflect on the optical

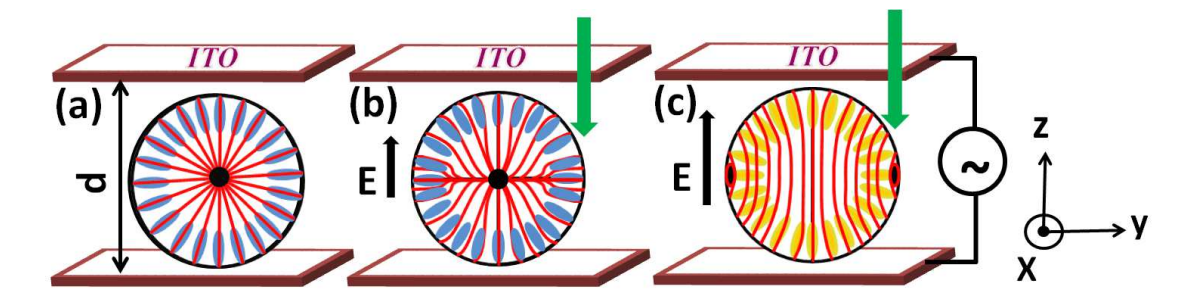


FIGURE 3.5: Schematic diagram showing the director field and resonance modes in a microdroplet at (a) zero, (b) small, and (c) large electric fields. The blue, yellow ellipsoids and red lines represents modes and director respectively.

resonance properties. We kept the temperature fixed in the nematic phase and collected the spectra at various voltages in a sequential order. The Q-factor was estimated from

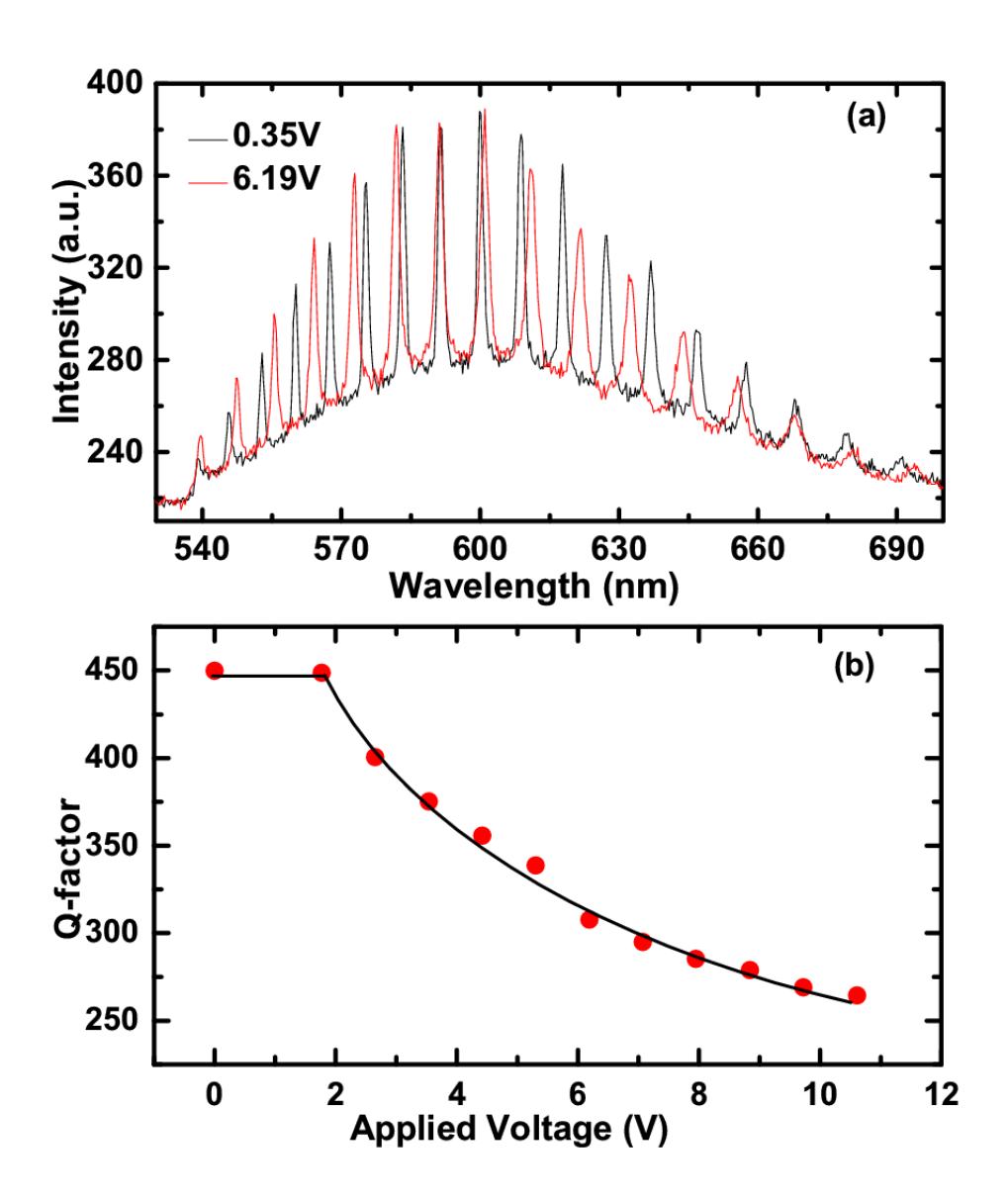


FIGURE 3.6: (a) WGM resonance spectra at two different voltages 0.35 V (Black) and 6.19 V (Red). (b) Variation of Q-factor with the applied voltage for the highest intensity mode. The continuous line is a guide to the eye. Droplet diameter: 8 μ m.

the linewidth of the mode with the highest intensity using equation 3.1. Figure 3.6(a) shows typical spectra obtained at two different voltages. Figure 3.6(b) shows the variation of Q-factor with respect to the applied voltage. The Q-factor remains unchanged up to a certain value and decreases rapidly with the increasing voltage. The decrease of Q-factor can be understood based on the effective refractive index seen by the light due to the elastic distortion of the director. It is known that the liquid crystal director deforms inside the microdroplets beyond a particular voltage [15,22], which is known as the Fredricksz threshold. The effective refractive index of the nematic liquid crystal is given by [24]:

$$n_{eff} = n_r = \sqrt{\frac{n_e^2 n_o^2}{n_o^2 sin^2 \theta + n_e^2 cos^2 \theta}}$$
 (3.6)

where θ is the angle between the propagation direction and the director (optic-axis). This relation is usually appropriate for the uniform director field but this can be adapted to the present situation specially near the equator where the modes are located (blue ellipsoids in Fig. 3.5). Using equation (3.6) we have at zero field $\theta = 90^{\circ}$ and $n_{eff} = n_r \simeq n_e$. In this case, the director (near the equator of the microdroplet where the modes are located) tilts towards the direction of the applied electric field and thus n_{eff} ($\simeq n_r$) decreases. Since Q_{mat} is linearly proportional to n_r , it is expected to decrease with the increasing electric field.

The careful observation of Fig. 3.4(a) and Fig. 3.6(a) shows that the free spectral range i.e., the separation of wavelengths between two consecutive modes ($\delta\lambda_{SM}$, denoted by FSR) of the resonance is also changing with the increasing temperature and the applied voltage. To quantify this behaviour of WGMs, we measured $\delta\lambda_{SM}$ as a function of the temperature and the applied voltage respectively. The behaviour of FSR with respect to the applied field and temperature respectively is presented in Fig. 3.7. It is observed that the FSR increases linearly with the applied voltage and at the highest applied voltage (i.e., 11V), the increment is about 2 nm (Fig. 3.7(a)). Figure 3.7(b) shows the variation of FSR with the temperature. It also increases almost linearly with temperature and changes slope at $\approx 30^{\circ}$ C. The increase of FSR with increasing temperature and voltage can be expected due to the change of the effective refractive index of the microresonator assuming the size remains unchanged. The FSR of a spherical microresonator is given by the following equation [2]:

$$FSR = \delta \lambda_{SM} = \frac{\lambda^2}{2\pi n_r R} \tag{3.7}$$

where R is the radius of the microresonator and λ is the resonant wavelength. When the temperature or the voltage is increased, the effective refractive index (n_{eff}) decreases as discussed previously. Since n_{eff} (= n_r) is inversely proportional to the FSR, it is expected to increase in both the cases.

A quantitative estimation of FSR can be made from equation (3.7). For example, at $T=26.5^{\circ}\mathrm{C}$ and $T=33.5^{\circ}\mathrm{C}$, the effective refractive indices of 5CB are given by n_{eff} (= n_e) = 1.702 and n_{eff} (= n_e) = 1.672 respectively [25]. The radius of the microdroplet is $4.5\mu\mathrm{m}$ and the resonant wavelengths at these two temperatures corresponding to the highest peaks are 603.3 nm and 602.3 nm respectively (see Fig. 3.4(a)). The calculated FSR at these two temperatures are 7.5 nm and 7.65 nm respectively. Thus the increase

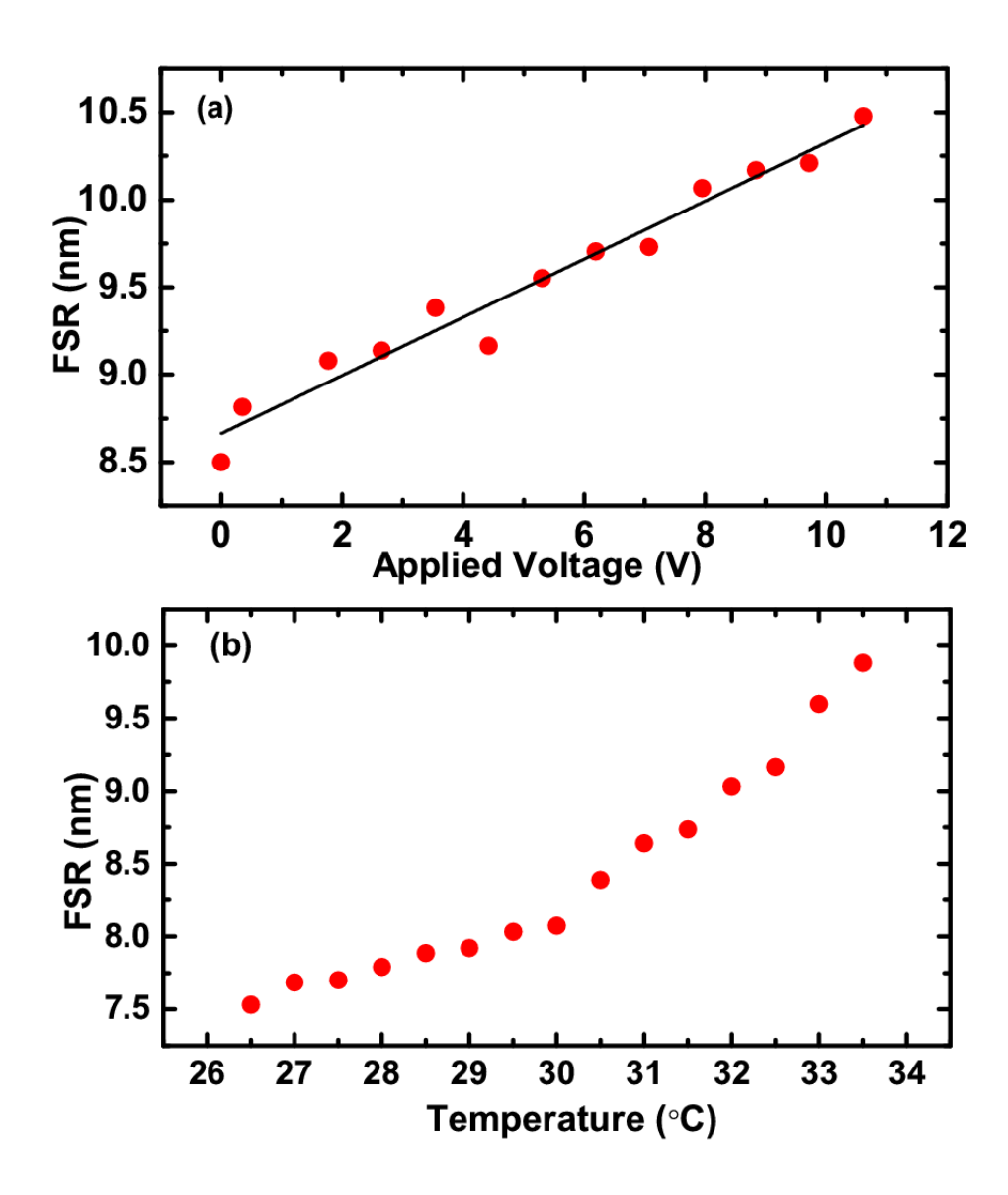


FIGURE 3.7: (a) Variation of the FSR with the applied voltage. The straight line is the best fit (linear) with a slope 0.17nm/V. (b) Variation of the FSR with temperature.

of FSR due to the increase of temperature (from 26.5°C to 33.5°C) is about 0.15 nm. But experimentally we find the increase of FSR is about 2.3 nm (Fig. 3.7(b)). Similarly, we estimate the FSR at zero and at the highest applied voltage. At zero voltage $\theta = 90^{\circ}$, and from equation (3.6) we get $n_{eff} = n_e = 1.702$ [25]. Assuming the director on the equator is completely reorientated along the field direction (i.e., $\theta = 0^{\circ}$, see Fig. 3.5(c)) at the highest voltage we get, $n_{eff} = n_o = 1.53$ [25]. The radius of the microdroplet is 4.0 μ m and the resonant wavelengths are 604.3 nm and 598 nm respectively (see Fig. 3.6(a)). The estimated corresponding FSR at the two voltages are 8.54 nm and 9.3 nm respectively. Hence, the maximum increase of FSR due to the electric field is about 0.75

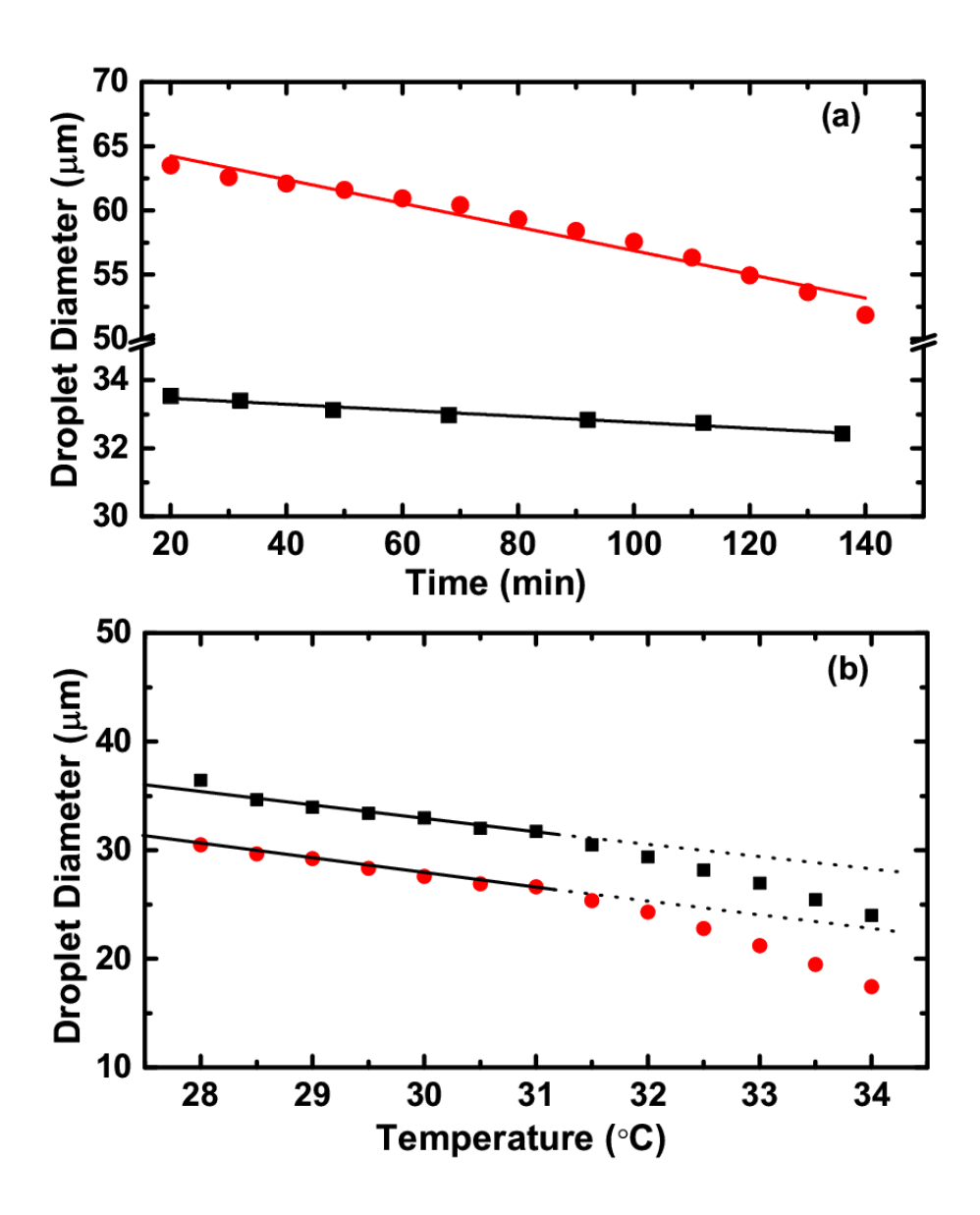


FIGURE 3.8: (a) Variation of diameters of the microdroplets with respect to (a) time and (b) temperature. The lines in (a) are the linear best fits. The slope of the smaller droplet $(33.5\mu\text{m})$ is 9nm/min. The dotted lines in (b) shows the deviation from the linear variation.

nm. But from the experiment we notice that the FSR is increased by about 2 nm (Fig. 3.7(a)). Therefore, the experimentally observed enhancement of FSR in both the cases cannot be understood from the decrease of the effective refractive index alone. This discrepancy motivated us to check the size of the microdroplets with time as FSR is inversely proportional to the microdroplet radius (R). For this purpose, we measured the diameters of a few microdroplets as a function of time and temperature. Figure 3.8(a) shows the variation of diameters of two different microdroplets with respect to time. It is observed that the diameter of the microdroplets is decreasing with time and

the rate is larger for the bigger microdroplets. For example, the initial diameter of a microdroplet with $D=33.5\mu\mathrm{m}$ decreases to 32.5 $\mu\mathrm{m}$ over the time duration of 140 minutes. Hence, the radius (R=D/2) of the LC microdroplet decreases at a rate of nearly 3.5 nm/min (from the slope). With the same rate, the microdroplet of radius $4\mu\mathrm{m}$ (Fig. 3.6(a)) is expected to decrease to 3.42 $\mu\mathrm{m}$ during the experiment. Taking the reduced size into account (i.e., $R=3.42\mu\mathrm{m}$) and the average refractive index $\overline{n}=1.587$ (i.e., $(n_e+2n_o)/3$), the estimated FSR from equation (3.7) is about 10.5 nm which is similar to that observed in Fig. 3.7(a). Therefore, the size reduction during the course of the experiment has significant effect on the FSR. Figure 3.8(b) shows the variation of the diameters of two different microdroplets with temperature. Initially the diameter decreases linearly with temperature and beyond 30°C it decreases much faster. The effect of this rapid size reduction beyond this temperature has been reflected clearly in the temperature dependence of FSR (Fig. 3.7(b)). In particular, the FSR initially increases linearly with temperature and at 30°C it changes the slope and it then further increases.

3.4 Conclusion

In conclusion, we have studied the effect of temperature and electric field on the quality factor and the free spectral range of nematic liquid crystal microdroplets embedded in PDMS polymer. The quality factor decreases significantly with increasing temperature due to the decrease of extraordinary refractive index. With the increasing electric field, the quality factor also decreases beyond a particular voltage due to the subsequent decrease of the effective refractive index. The free spectral range increases with the increasing temperature and the voltage due to the reduction of the effective refractive index of the LC microdroplet as a whole. Thus, both the quality factor and the free spectral range can be tuned electrically and thermally. We find that the size reduction with time has a significant effect on the free spectral range. The experimental change of the free spectral range is in good agreement with the quantitative estimation based on the time dependent size reduction of the microdroplets.

Bibliography

- [1] S. Arnold, S. Holler, and S. D. Druger, Optical Processes in Microcavities.
- [2] Kerry Vahala, Optical Microcavities, World Scientific, (2004).
- [3] R. K. Chang and A. J. Campillo, eds., Advanced Series in Applied Physics, Vol. 3, Singapore: World Scientific (1996).
- [4] A. B. Matsko and V. S. Ilchenko, Quantum Electronics, 12, 3 (2006).
- [5] A. B. Matsko and V. S. Ilchenko, Quantum Electronics, 12, 15, (2006).
- [6] F. Vollmer, and S. Arnold, Nat. Methods 5, 591 (2008).
- [7] S. Arnold, S. I. Shopova, and S. Holler, Opt. Express, 18, 281 (2010).
- [8] X. Fan, I. M. White, S. I. Shopova, H. Zhu, J. D. Suter, and Y. Sun, Anal. Chim. Acta 620, 8 (2008).
- [9] S. Arnold, M. Khoshsima, I. Teraoka, S. Holler, and F. Vollmer, Opt. Lett. 4, 272 (2003).
- [10] F. Vollmer, S. Arnold and D. Keng, Proc. Natl. Acad. Sci. USA, 105, 20701 (2008).
- [11] M. Loncar, Nat. Photonics 1, 565 (2007).
- [12] H. Wang, L. Yuan, C-W. Kim, Q. Han, T. Wei, X. Lan, H. Xiao, Opt. Lett. 37, 94 (2012).
- [13] J. J. Yang, M. Huang, X. Z. Dai, M. Y. Huang, Y. Liang, Europhysics Lett. 103, 44001 (2013).
- [14] L. He, S. K Qzdemir, J. Zhu, W. Kim and L. Yang, Nat. Nanotechnology 6, 428 (2011).
- [15] M. Humar, M. Ravnik, S. Pajk and I. Musevic, Nat. Photon., 3, 595 (2009).
- [16] T. Arun Kumar, M. A. Mohiddon, N.Dutta, Nirmal K, Viswanathan, and Surajit Dhara, Appl. Phys. Lett. 106, 051101 (2015).

- [17] Y. Wang, H. Li, L. Zhao, Y. Liu, S. Liu and J. Yang, Opt. Express 25, 918 (2017).
- [18] M. Marusa, J. A. Sofi, I. Kvasic, A. Mertelj, D. Lisjak, V. Niranjan, I. Musevic and Surajit Dhara, Opt. Express 25, 1073 (2017).
- [19] C. C. Lam, P. T. Leung and K. Young, J.Opt. Soc. Am. B 9, 1585 (1992).
- [20] M. L. Gorodetsky, A. A. Savchenkov, and V. S. Ilchenko, Opt. Lett. 21, 453 (1996).
- [21] J. Li, S. Gauza, S. T. Wu, J. Appl. Phys. **96**, 19 (2004).
- [22] H. S. Kitzerow and P.P. Crooker, Liq. Cryst., 13, 31 (1993).
- [23] A. V. Koval Chuk, M.V. Kurik, O. D. Lavrentovich and V. V. Sergan, Sov. Phys. JETP 67, 1065 (1988).
- [24] L. C. Khoo, Liquid Crystals, Wiley-Interscience, Canada (2007).
- [25] Ph. D thesis of P. Karat, Raman Research Institute, Bangalore, India (1977).

Chapter 4

Stability of liquid crystal based optical microresonators

4.1 Introduction

In the previous chapter, we realized the importance of stable surrounding medium for liquid crystal (LC) microdroplets based optical microresonators. The surrounding medium that supports the smooth and spherical LC micrdroplet formation is very vital for their long lasting photonic applications [1-2]. In addition to being optically transparent, the medium has to support the larger life time sustainability of the LC microdroplets as well. In polymer dispersed liquid crystals, appropriate amount of polymers and liquid crystals are mixed through any of the droplet making methods discussed in Sec.2.4 of Chapter 2. In the immiscible mixture, tiny droplets ranging from a few tens of nanometer to micrometer size LC microdroplets are phase separated from the polymer matrix [3]. The dispersed LC microdroplets exhibit variety of director structures depending on the bulk elasticity and surface anchoring (Sec. 1.3, Chapter 1) [4-5]. In case of nematic LC microdroplets, if the surface anchoring is strongly homeotropic, commonly a radial director structure with a hedgehog defect at the centre of the microdroplet is observed [2,6]. In case of strongly planar surface anchoring two boojums at the interface are usually observed. A variety of other complex structures can be observed in cholesteric and smectic-C liquid crystal microdroplets [7-10].

In most of the previous studies on LC microdroplets suspended in various media, either glycerol or polydimethylsiloxane (PDMS) were used as supporting media [2-3,6,11-13]. It was found that the LC microdroplets in these dispersing media are not highly stable in the sense that the diameter decreases with time [2]. This is disadvantageous as far as the application point of view is concerned and hence it is important to find a suitable

supporting media with desired properties. Till date, no study has been carried out that aims to address the size stability of the liquid crystal microdroplets. In this chapter we present some experimental studies on LC microdroplets dispersed in several dispersing media.

4.2 Experimental

In the experiment, we have used two liquid crystals namely, 5CB and MLC-6608. 5CB was obtained from Sigma-Aldrich and it exhibits room temperature nematic phase. MLC-6608 was obtained from Merck and it exhibits a wide temperature range of nematic phase, extending from -30°C to 90°C. The dielectric anisotropy of MLC-6608 is negative, i.e. $\Delta \epsilon = -4.2$ and the elastic constants at ambient temperatures are $K_{11} = 16.7 \times 10^{-12} \text{N}, K_{22} = 7.0 \times 10^{-12} \text{N} \text{ and } K_{33} = 18.1 \times 10^{-12} \text{N}, \text{ respectively}$ [14,15]. All the experiments are performed at ambient temperature. The extraordinary and ordinary refractive indices of 5CB at room temperature are given by $n_e = 1.702$ and $n_o = 1.55$ [16]. In case of MLC-6608, $n_e = 1.56$ and $n_o = 1.477$ [17]. We used three polymers as supporting media namely, PDMS, a mixture of glycerol-lecithin and Cytop. Cytop was obtained from Asahi Glass Co. Ltd, Japan. The refractive index of PDMS and glycerol are 1.38 and 1.47 respectively [18]. PDMS provides homeotropic whereas glycerol provides planar liquid crystal anchoring. A small amount of lecithin (about 5 to 10 wt%) mixed with glycerol provides homeotropic anchoring. The refractive index of Cytop is 1.34 and is smaller than that of both the PDMS and the glycerol, respectively. It is worth mentioning that all the chosen supporting media in this work were used in experiments preferentially due to their lower refractive indices than the liquid crystals. Cytop is highly transparent over a wide wavelength range (200 nm to 2μ m) and is used as an antireflective coating in organic light emitting devices [19,20]. It has high solubility in perfluorinated solvents and is highly resistant to chemical and thermal stimuli [21]. Cytop has been used as an alignment layer in case of liquid crystals and in this direction, several experimental findings showing the discontinuous anchoring transition have been reported [21-30]. Emulsion method (Sec. 2.4.2, Chapter 2) was used to form LC micrdroplet dispersion in the respective media. No curing agent was added to the polymers because it often changes the surface anchoring of the liquid crystals and thus results in the morphology breakage of the LC microdroplets. The optical set up as discussed in section 2.6 of the Chapter 2 was used to carry out the experiments and recording the WGM spectra. Argon-ion laser with a wavelength of 514nm was used to excite Nile red dye doped LC microdroplets and the optical resonance was observed within a range of 540-700nm. In the electric field experiments, cell with parallel plate electrodes and cell with in-plane electrodes (Sec. 2.2.3, Chapter 2) were used. Microdroplets with uniform

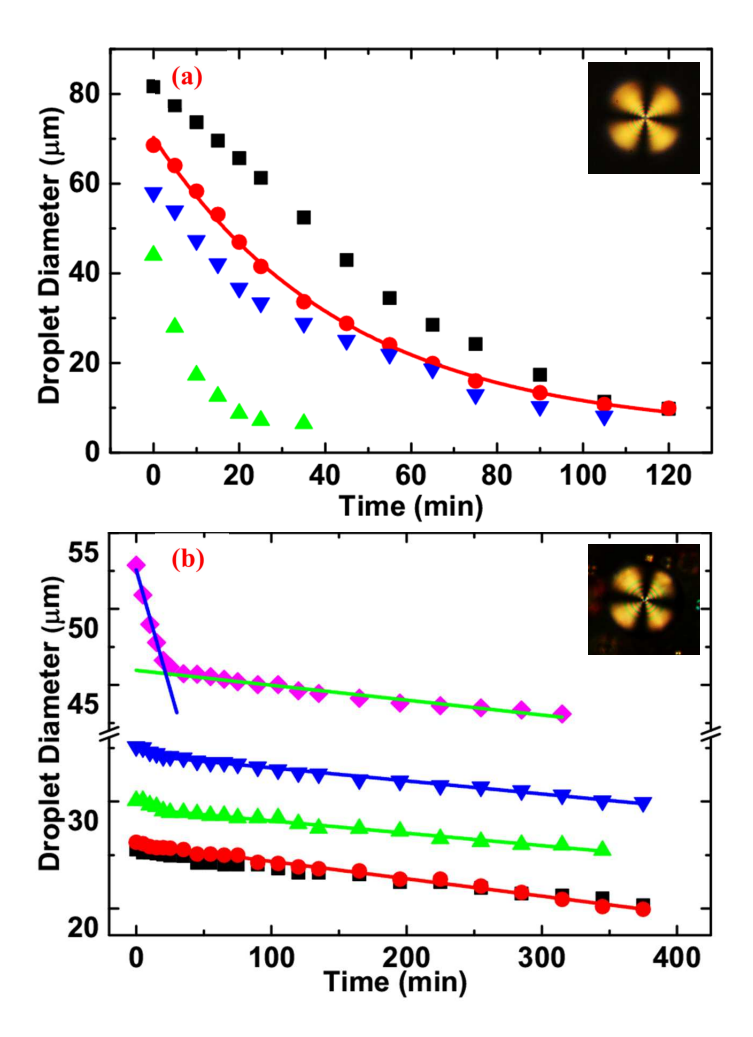


FIGURE 4.1: Variation of diameter of 5CB microdroplets with time, dispersed in (a) PDMS (b) glycerol (90%) lecithin (10%) mixture. The continuous red line in (a) is a best fit to the equation; $D(t) = D(0) + Ae^{-t/\tau}$. Continuous lines in (b) are linear best fits. The measurements are made directly from the optical microscope at room temperature. Polarising optical microscope images of microdroplets with defects (Inset).

radial director structure were selected and excited with a focused beam of Argon-ion laser through the objective of the microscope. The light emitted by the dye-doped LC microdroplets is collected by the same objective and is sent to the spectrometer as per the optical path shown in the schematic diagram in Fig 2.12 in Chapter 2 [31]. Sinusoidal voltage was applied across the cell with the help of a function generator which is fixed at 5 kHz frequency and connected to a voltage amplifier.

4.3 Results and discussion

We studied the time dependent size of the LC microdroplets using a polarising optical microscope. Figure 4.1 shows the time variation of the diameters of a few 5CB microdroplets in PDMS (see Fig. 4.1(a)) and in glycerol (90%) lecithin (10%) mixture (see

Fig. 4.1(b)), respectively. 5CB in PDMS shows radial anchoring of the LC molecules whereas in pure glycerol, they usually show planar anchoring with a pair of boojum defects situated diametrically opposite to each other (Fig. 1.7 (d,e,f), Chapter 1). We find that a small amount of lecithin in glycerol induced homeotropic anchoring to the liquid crystal molecules and give rise to the radial director structure in the microdroplets. In PDMS, the microdroplet diameter decreases rapidly in a nonlinear manner. For example, the diameter of 70μ m 5CB droplet decreases nearly to 10μ m within two hours (see Fig. 4.1(a)). In fact, sometimes the LC microdroplets disappear and completely mix with the PDMS over a short period of time, typically around half an hour or so. An empirical equation; $D(t) = D(0) + Ae^{-t/\tau}$ is fitted to get the decay constant for a particular LC microdroplet, where A is a constant. The decay constant $\tau \simeq 50$ minutes, suggesting 63% of the size is shrunken within 50 minutes after the LC microdroplet formation. In case of glycerol-lecithin mixture, the LC microdroplet diameter decreases linearly but the rate is much slower than as observed in PDMS (see Fig.4.1(b)). For example, the diameter of a $26\mu m$ droplet decreases to about $21\mu m$ after about 6 hours. Beyond about 50 minutes, the LC microdroplet size decreases by about 100nm/minute. For bigger LC microdroplets $(D > 40\mu m)$, initially the decay is faster (about 350nm/minute) and there is a clear slope change at about 30 minutes. Therefore, glycerol lecithin mixture is comparatively better dispersing medium than PDMS. However, the glycerol-lecithin mixture appears yellowish and the scattering as well as absorption losses are relatively higher than PDMS. These shortcomings motivated us to look for an alternative supporting medium. We have chosen Cytop as a supporting medium for studying the stability and the director orientation of the liquid crystal microdroplets.

Figure 4.2(a) shows microdroplets of MLC-6608 liquid crystal dispersed in Cytop. This polymer almost stabilises the spherical LC microdroplets with radial anchoring. Four orthogonal dark brushes as seen under crossed polarizers, with concentric rings around the centre suggests the director to be orthogonal onto the Cytop surface and thus the director is radially symmetric in the LC microdroplets. A radial hedgehog point defect is seen at the centre of the LC microdroplets. Figure 4.2(b) shows the variation of the diameter of a few LC microdroplets with time at room temperature, measured using optical microscope. It is observed that the LC microdroplet diameter decreases very slowly with time and beyond about three hours of formation, their size is completely stabilised (time shown by vertical dotted line in Fig.4.2(b)). Thus, Cytop is much better supporting medium in terms of LC microdroplet longevity than PDMS and glycerollecithin mixtures at ambient temperature. We also looked at the effect of temperature on the LC microdroplet size and found a small decrease of the same at higher temperatures (see Fig.4.3).

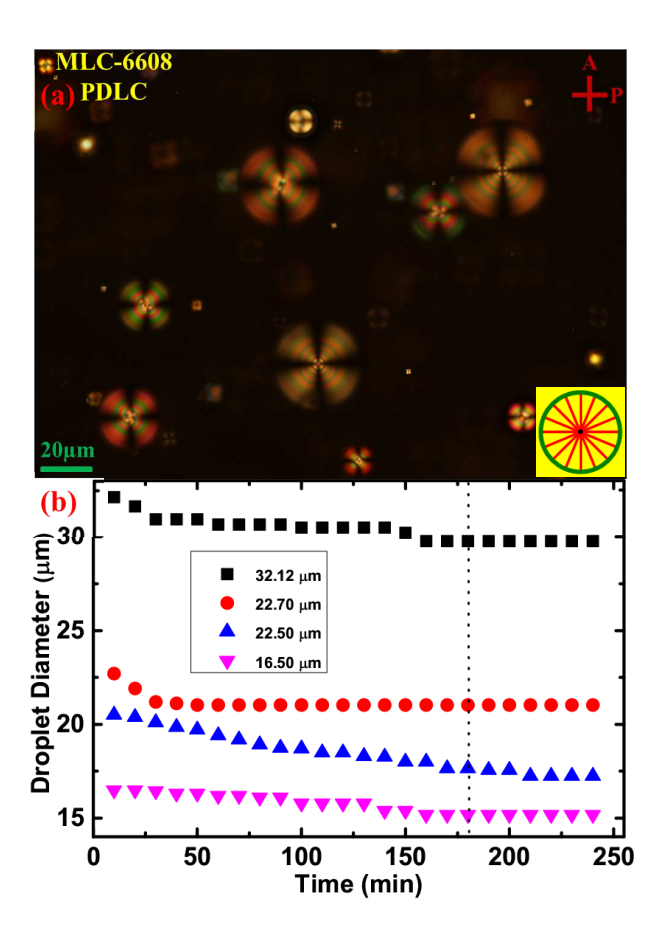


FIGURE 4.2: (a) Polarising optical microscope images (POM) of MLC-6608 microdroplets of various size suspended in Cytop. Inset shows a schematic diagram of radial director structure (b) Variation of microdroplet diameters with time at room temperature measured by using optical microscope. The vertical dotted line indicates the time beyond which the LC microdroplets are highly stable and used for optical resonance studies.

The size decreasing rate is approximately equal to 85 nm/°C. Comparatively, it is more than one order of magnitude slower than that previously reported values in case of PDMS [2]. The perfluoropolymer has a large number of fluorine atoms. The fluorine has a small atomic radius and the largest electronegativity among the atoms, so that it forms a stable covalent bond with carbon and thus effective in lowering the surface energy. Hence, the liquid crystal molecules are not soluble in to the perfluoropolymer and consequently the size remains stable with time. In addition, perfluoropolymer is also highly resistant to chemical and thermal stimuli [23] owing to the high bonding energy of C-F (485 kJ mol⁻¹) and C-C (360 kJ mol⁻¹) bonds [32].

We selected a microdroplet of MLC-6608 of diameter 10.6μ m for studying optical resonance. Figure 4.4(a) shows the polarising optical microscope image. Figure 4.4(b) shows spherical LC microdroplet with sharp interface of the droplet-Cytop. Figure 4.4(c) shows excitation of WGM in the dye doped LC microdroplet when illuminated

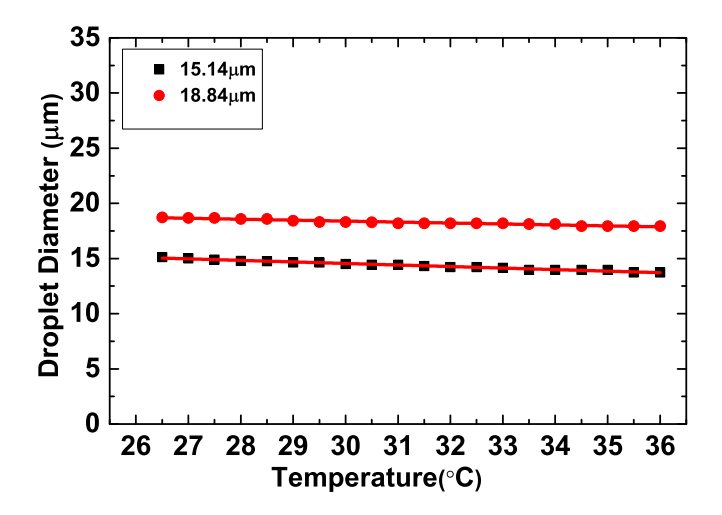


FIGURE 4.3: Variation of diameter of two MLC-6608 microdroplets, $15.14\mu m$ and $18.84\mu m$ with temperature in Cytop.

by a tightly focussed 514 nm laser beam through a 60X objective. A light stripe running diametrically across the LC microdroplet suggests the localisation of the modes around it. Figure 4.4(d) shows a typical WGM resonance spectrum emanated from the illuminated LC microdroplet. The resonance modes are observed on the overlay of the fluorescence intensity of the LC microdroplet. Liquid crystals are birefringent and hence possess different refractive indices for different polarisations. As discussed in Chapter 1 (Sec. 1.6), for transverse magnetic mode (TM), the electric field oscillates along the longer molecular axes (optic axis) while as for the transverse electric mode (TE) case, the electric field oscillates perpendicular to the molecular axis. In spherical LC microdroplets, the refractive index sensed by the former polarisation is extraordinary index (n_e) and the latter one experiences ordinary index (n_e) .

For an LC microdroplet of diameter $10.6\mu\text{m}$, we find that only TM modes with radial mode number q=1 are supported. From the analytical solutions as discussed in section 1.6 of chapter 1, the angular mode numbers (l) for the same microdroplet are calculated using $n_s=1.557$ [33] and $n_a=1.34$ [23]. In the wavelength range of 540-680nm, l varies from 71 to 89, which are labeled in Fig.4.4(d). The stability of the LC microdroplets was further studied by measuring the free spectral range (FSR). For spherical microdroplets, it is defined as:

$$FSR = \delta \lambda_{SM} = \frac{\lambda^2}{n_{eff}\pi D} \tag{4.1}$$

where, $1/n_{eff}^2 = \sin^2\theta/n_e^2 + \cos^2\theta/n_o^2$ and $\delta\lambda_{SM}$, D, n_e , n_o and θ are spacing between two successive modes, the diameter of the microdroplets, extraordinary refractive index, ordinary refractive index of the liquid crystal and the angle between the optical axis

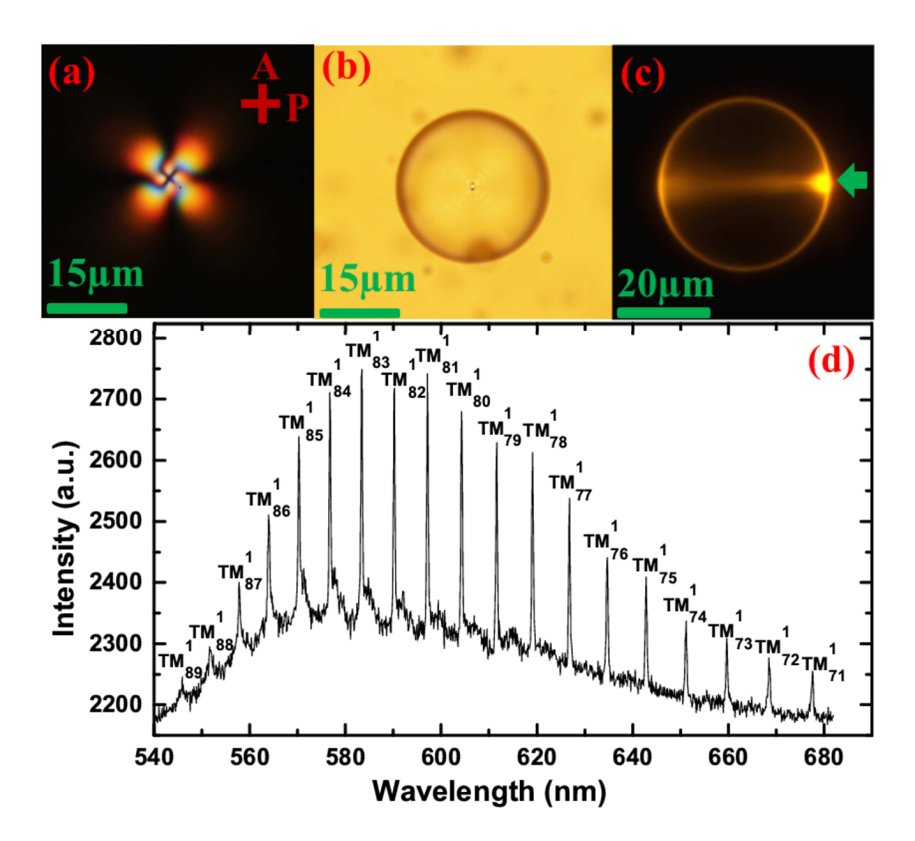


FIGURE 4.4: (a) Optical polarising micrograph of an MLC-6608 micro-droplet dispersed in Cytop at room temperature. (b) Droplet as seen without polarisers. (c) A Nile-Red dye-doped LC microdroplet illuminated by a focused 514 nm laser beam. The irradiation point is marked by green arrow. (d) Optical resonance spectrum recorded by the spectrometer from an illuminated LC microdroplet with calculated TM modes.

and the light propagation direction respectively [34]. Figure 4.5(a) shows the variation of FSR with time for a few LC microdroplets. The measurements were made after 3 hours from the formation of the LC microdroplets. It is observed that the FSR for all the microdroplets is independent of time. Figure 4.5(b) shows the variation of FSR for several LC microdroplets with varying diameter from 7 to 45 μ m. The FSR is inversely proportional to the microdroplet diameter (D). The best fit to the data (FSR $\propto 1/D$) is also shown in Fig. 4.5(b).

The WGMs displayed by the LC microdroplets are highly morphology dependent. In case of liquid crystals, the director inside the microdroplets is distorted by the external electric and magnetic fields and consequently WGM resonance properties are expected to get affected. In our previous studies we showed the effect of electric field on the WGM resonance properties of a microdroplet made up of liquid crystal compound possesing positive dielectric anisotropy ($\Delta \epsilon > 0$) [2]. In the present experiment, the dielectric anisotropy of MLC-6608 is negative ($\Delta \epsilon < 0$). The effect of electric field on the LC microdroplets and defects in liquid crystal microdroplets with $\Delta \epsilon < 0$ has been studied [35], however its subsequent effects on the optical resonance properties have not been

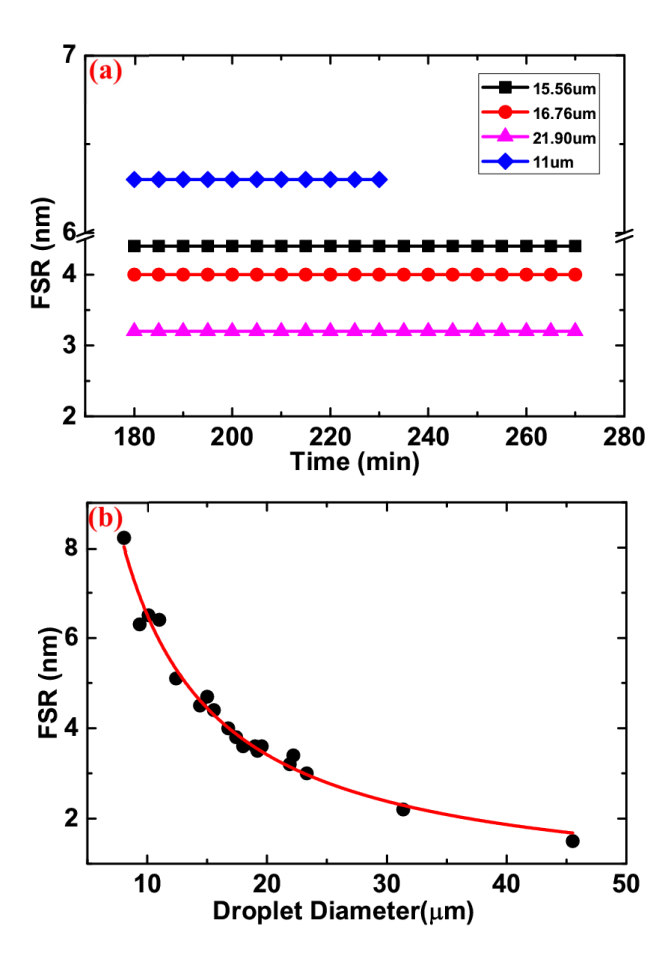


FIGURE 4.5: (a) Time dependence of FSR of different size LC microdroplets dispersed in Cytop. (b) Variation of FSR with microdroplet size. The red line is the best fit to FSR $\propto 1/D$. The error bar in (a) is almost equal to the point size. All the measurements are made at room temperature.

studied so far. Figure 4.6 (a-c) shows the typical elastic distortion in an MLC-6608 microdroplet when the applied electric field is parallel to the direction of the light propagation ($\mathbf{E}||\mathbf{k}|$). The director configuration is mostly radial with a slight azimuthal twist near the central region that encompasses a radial hedgehog defect. The structure becomes complex with increasing field and the distortion from the central region expands toward the boundary (see λ -plate images). It has been suggested that the hedgehog defect undergoes a continuous transition into an escape nonsingular line defect with s=1 [35]. It appears that the line defect is well within the central region and no significant or noticeable distortion of the director is observed very close to the inner boundary wall. The WGM spectra of a 10.6 μ m droplet at two representative fields namely 0.12 $V/\mu m$ and 0.56 $V/\mu m$ are shown in Fig.4.6(d). The resonance intensity decreases slightly with the increasing field. The modes above 635 nm shift slightly towards higher wavelength and below, they shift towards lower wavelength side.

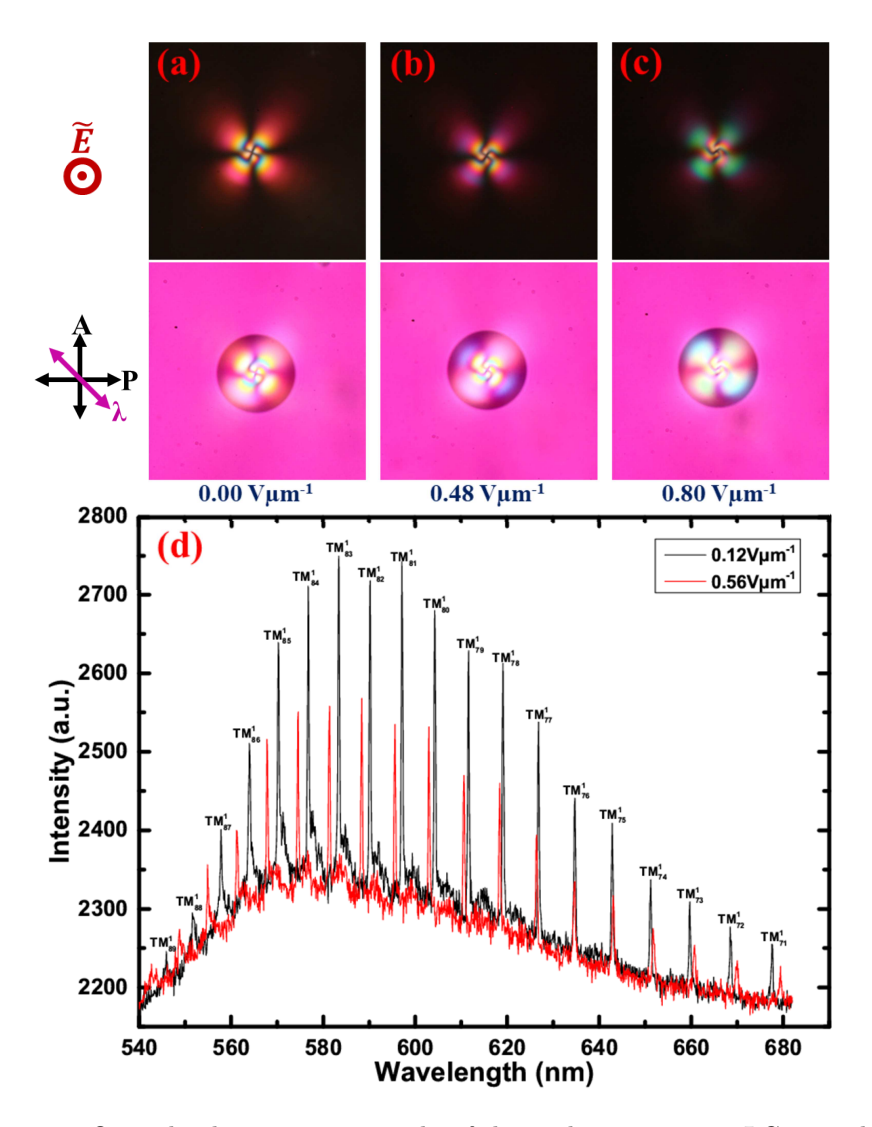


FIGURE 4.6: Optical polarising micrographs of elastic distortion in an LC microdroplet at (a) zero electric field (b-c) increasing electric field. Corresponding λ -plate images are shown underneath. (d) Representative WGM spectra of an LC microdroplet below (0.12 $V/\mu m$) and above (0.56 $V/\mu m$) Freedericksz threshold field. The direction of electric field and the orientation of the slow axis of the λ -plate with respect to the crossed polarisers is shown on the left side.

We measured the Q-factor and FSR at different fields of a few modes. Figure 4.7(a,b) shows electric field dependent Q-factor and FSR. We used a grating of 300 lines/mm to observe and analyse many modes over a larger wave length range. It is observed that the Q-factor is found to be about 1.5×10^3 and it remains almost unchanged with the increasing applied electric field. This is in sharp contrast with the resonance properties of LC microdroplets with $\Delta \epsilon > 0$, where a substantial decrease in Q was reported beyond Freedericksz threshold field [2]. The Freedericksz threshold field for MLC-6608 is about $0.3V/\mu m$. This unaltered Q-factor in case of MLC-6608 microdroplets means that just inside the liquid crystal-Cytop boundary where the light is circulating, there is no elastic deformation to the director. In other words, the circulating light is confined within

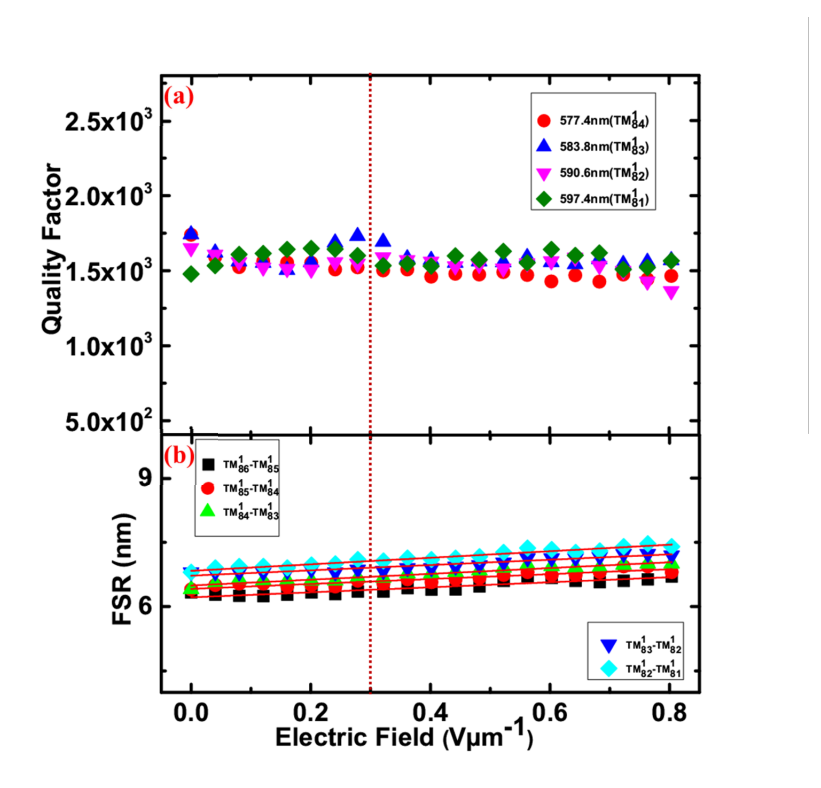


FIGURE 4.7: (a) Variation of Q-factor $(\lambda/\Delta\lambda)$ of a few TM modes with applied electric field of an MLC-6608 microdroplet with diameter $10.7\mu\mathrm{m}$ using a grating of 300 lines/mm (b) Variation of FSR with applied electric field of a few TM modes. Vertically dotted line represent the Freedericksz threshold field.

the extrapolation length ($\sim 100nm$) inside the interface. This is consistent with the observation (see λ -plate images in Fig.4.6(a-c)), where the elastic distortion is mostly confined near the central region. Figure 4.7(b) shows the variation of FSR with the applied electric field. It is observed that FSR of the modes is about 7 nm and is almost independent of the applied electric field. FSR depends mainly on two parameters namely; the diameter (D) and the effective refractive index (n_{eff}) of the droplet. Thus both the droplet diameter and the effective refractive index at the interface does not change with the applied electric field.

The perfluoropolymer Cytop is highly transparent and hence the absorption is very low [23] and in addition, it has lower refractive index than the PDMS or the glycerol or any other polymers reported so far in WGM resonance studies. Hence quality factor is expected to be larger owing to the optically less lossy nature of the Cytop as well. We used high resolution grating (2400 lines/mm) which gives a spectral resolution of 0.021 nm within a small wavelength range. Figure 4.8 shows a few highly narrow TM modes of a 10.6μ m microdroplet. The estimated quality factor of these modes is about $Q \simeq 1.2 \times 10^4$. It is the highest Q-factor reported so far in case of liquid crystal microdroplets dispersed in other mediums and is larger by about 2000 than the previously reported

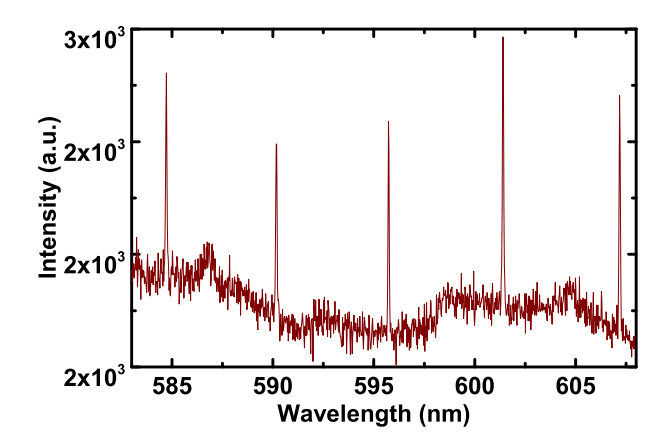


FIGURE 4.8: Optical resonance spectrum recorded by the spectrometer using a high resolution grating of 2400 lines/mm in the absence of external applied electric field. Droplet diameter 10.6μ m.

value [6].

We also tried to design our experiment in a way to apply in-plane field to the liquid crystal microdroplets. For this purpose, we employed various electrodes like aluminum foil, copper tape etc. Figure 4.9 shows optical polarising images of a $20.1\mu m$ MLC-6608 under increasing in-plane field strength. The director distortion observed in the microdroplets is not of much stark contrast. Consequently, we did not observe any effect on WGM optical resonance properties. The thickness of the cells was fixed at $410\mu m$.

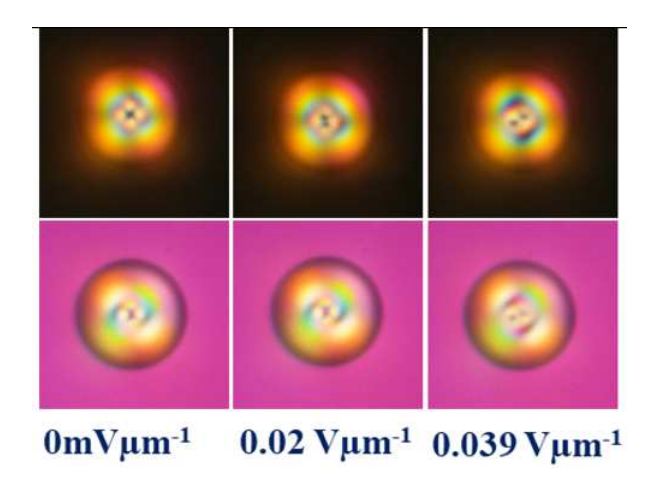


FIGURE 4.9: In-plane electric field induced structural distortion in MLC-6608 microdroplets. Droplet diameter is $20.1\mu m$.

4.4 Conclusion

In summary, we find that the Cytop is one of the best supporting media for forming stable LC microdroplets, which is very crucial for the successful realisation of the LC based microresonators. This is the first optical resonance study on negative dielectric anisotropy LC microdroplets. FSR is inversely proportional to the diameter of the microdroplets in accordance with the prediction and hence smaller microdroplets are of greater importance. The circulating light is confined within the extrapolation length at the boundary region where the resonant modes are located. Consequently the quality factor remains unaffected inspite of the elastic distortion observed in the LC microdroplet director under the influence of the external electric field. The highest quality factor is attributed to the low refractive index and high transparency of the supporting medium Cytop. Finally, we showed a new application of Cytop in liquid crystal based microresonators with superior performance. The resonance properties when the applied electric field is parallel to the direction of exciting laser beam is not encouraging for electrical tuning of the resonance. The in-plane electric field i.e. when the applied electric field direction is perpendicular to the director, is expected to be more effective in tuning and controlling the optical WGM properties of negative dielectric anisotropy LC microdroplets.

Bibliography

- [1] K. Vahala, Optical Microcavities, World Scientific, 2004.
- [2] J. A. Sofi, M.A. Mohiddon, N. Dutta and Surajit Dhara, Phys. Rev. E. 96, 022702 (2017).
- [3] P. S. Drzaic, Liquid Crystal Dispersions, World Scientific Publishing: Singapore, (1995).
- [4] M. Humar, Liquid-Crystal Microdroplets as Optical Microresonators and Lasers, Ljubljana, Slovenia, February 2012.
- [5] P. G. De Gennes and J. Prost, The Physics of Liquid Crystals (Oxford University, 1993).
- [6] M. Humar, M. Ravnik, S. Pajk and I. Musevic, Nat. Photon., 3, 595 (2009).
- [7] Y. Zhou et al. ACS Nano 10, 6484 (2016).
- [8] M. Urbansk, C. G. Reyes, J. Noh, A. Sharma, Y. Geng, V. S. R. Jampani and J. P. F. Lagerwall, J. Phys.: Condens. Matter 29 133003 (2017).
- [9] G. Posnjak, S. Coper. and I. Musevic, Nat. Commun. 8, 14594 (2017).
- [10] J. Yoshioka and F. Araoka, Nat. Commun. 9, 432 (2018).
- [11] O. D. Lavrentovich, Liq. Cryst., 24, 117 (1998).
- [12] T. Porenta, M. Ravnik and S. Zumer, Soft Matter 7, 132 (2011).
- [13] K. Peddireddy, S. R. Jampani, S. Thutupalli, S. Herminghaus, C. Bahr and I. Musevic, Opt. Express., 21, 30233 (2013).
- [14] X.Nie, Y.H. Lin and S.T. Wu, J. Appl. Phys. 98, 013516 (2005).
- [15] J. Li, Refractive Indices of Liquid crystals and their Applications in Display and Photonic Devices (Tsinghua University, 2005).
- [16] R. G. Horn, J. Physique, **39**, 105 (1978).

- [17] J. Li, C.-H Wen, S. Gauza, R. Lu and S.-T. Wu, J. Disp. Technol., 1, 1 (2005).
- [18] L.F. Hoyt, L. Company, Inc., Buffalo, N. Y., J. Ind. Eeg. Chem., 26, 329 (1934).
- [19] K. Yamamoto, G. Ogawa, J. Fluorine Chem., 126, 1403 (2005).
- [20] S. M. Jeong, F. Araoka, Y. Machida, K. Ishikawa, H. Takezoe, S. Nishimura, G. Suzaki, Appl. Phys. Lett., 92, 083307 (2008).
- [21] J. K. Kim, S. M. Jeong, Surajit Dhara, F. Araoka, K. Ishikawa and H. Takezoe, Appl. Phys. Lett., 95, 063505 (2009).
- [22] Surajit Dhara, J. K. Kim, S. M. Jeong, R. Kogo, F. Araoka, K. Ishikawa and H. Takezoe, Phys. Rev. E. 79, 060701 (2009).
- [23] S. M. Jeong, Y. Shimbo, F. Araoka, Surajit Dhara, N. Y. Ha, K. Ishikawa and H. Takezoe, Adv. Mater. 22, 34 (2010).
- [24] T. Arun Kumar, P. Sathyanarayana, V. S. S. Sastry, H. Takezoe, N. V. Madhusu-dana and Surajit Dhara, Phys. Rev. E 82, 011701 (2010).
- [25] D. Venkata Sai, T. Arun Kumar, Arun Roy, W. Haase and Surajit Dhara, J. Chem. Phys. 141, 044706 (2014).
- [26] T. Arun Kumar, H. Takezoe and Surajit Dhara, Jpn. J. Appl. Phys., 750, 040203 (2011).
- [27] T. Arun Kumar, V. S. S. Sastry, K. Ishikawa, H. Takezoe, N.V. Madhusudana and Surajit Dhara, Liq. Cryst. 38, 971 (2011).
- [28] T. A. Kumar, Khoa V. Le, S. Aya, K. Fukuda, F. Araoka, K. Ishikawa, J. Watanabe, S. Dhara, and H. Takezoe, Phase Transitions 85, 888 (2012).
- [29] V. S. R. Jampani, M. Skarabot, H. Takezoe, I. Musevic and Surajit Dhara, Optics Express 21, 724 (2013).
- [30] M. V. Rasna, K. P. Zuhail, R. Manda, P. Paik, W. Haase, and Surajit Dhara, Phys. Rev. E 89, 052503 (2014).
- [31] J. A. Sofi, A. Barthakur and S. Dhara, Soft Matter, 15, 7832-7837, (2019).
- [32] V. Arcella, P. Colaianna, P. Maccone, A. Sanguineti, A. Gordano, G. Clarizia, E. Drioli, J. Membr. Sci., 163, 203 (1999).
- [33] T. Scharf, Polarized light in liquid crystals, Wiley Online Library, April 2006.
- [34] G. Si, Y. Zhao, E. S. P. Leong and Y. J. Liu, Materials **7(2)**,1296 (2014).
- [35] F. Xu, H. S. Kitzerow and P. P. Crooker, Phys. Rev. A. 46(10), (1992).

Chapter 5

Whispering gallery mode lasing in mesomorphic liquid crystal microdroplets

5.1 Introduction

The quest for the successful realization of flexible and integrated photonic devices has drawn a great deal of interest in the recent years. Such devices require tunable optical microcomponents such as filters, sensors and waveguides. In this context, liquid crystal based optical microcomponents are prospective contenders for future generation tunable microdevices [1-9]. Liquid crystals exhibit variety of mesophases with distinct optical properties and each mesophase might offer unique technological solution for specific devices. Peddireddy et al. demonstrated lasing and waveguiding in Smectic-A liquid crystal fibers [10]. We demonstrated the magnetic field tuning of whispering gallery mode lasing from ferromagnetic nematic liquid crystal microdroplets [11]. Despite rich and diverse structures of liquid crystals, no comparative study has been reported so far with an aim to bring out the relative merits of lasing in the mesomorphic microdroplets. In the previous two chapters, we discussed on electrical and thermal stimuli based whispering gallery mode resonance tunability and on the stable media for liquid crystal microdroplets [12,13]. In this chapter, we present the experimental studies on morphology and WGM lasing properties in the Nematic (N), Smectic-A (SmA) and Smectic-C (SmC) microdroplets of a liquid crystal compound dispersed in Cytop solution.

5.2 Experimental

We used a pyridine derivative liquid crystal compound that exhibits the following phase transitions: I 68°C N 64.5°C SmA 57.7°C SmC 33.2°C Cr. It exhibits a first order I to N and a second order SmA-SmC phase transitions [14]. A small amount of Nile Red fluorescent dye (0.7% wt) was doped in the liquid crystal compound for inducing fluorescence. The transition dipole moment of the dye molecule is along the long axis [15,16]. Cytop solution is used as supporting medium due to its better stability as discussed in Chapter 4. The Cytop solution containing microdroplets, prepared through modified emulsion method (Sec. 2.2.), is inserted in a cell prepared by two glass plates which are separated by a spacer of thickness $240\mu m$ (Chapter 2). The LC microdroplets are formed in the nematic phase and cooled slowly to the SmA and SmC phases respectively. The experimental setup discussed in section 2.6 of chapter 2 is used for conducting the WGM experiments. A temperature controller and a heating stage mounted on the microscope is used to control the temperature with an accuracy of 0.1 °C.

5.3 Results and discussion

For the sake of the stable liquid crystal microdroplet suspension, we explored many transparently isotropic media to figure out an appropriate dispersing medium for liquid crystal microdroplets that provides radial anchoring to the LC director and sustains for considerable time. We tried forming LC microdroplets in several polymers such as Polydimethylsiloxane (PDMS), Glycerol-Lecithin mixture and the Cytop solution. From the comparative study with N, SmA and SmC phase microdroplets, it is found that the Cytop-solution provides a perfect radial anchoring of the director. The radial anchoring is strong and retained over several weeks, without any observable change in the texture. To check the mechanical stability, we applied mild physical stress on the LC microdroplets with the help of a mechanical tweezer. It is observed that the textures of N and SmC microdroplets are changed irreversibly whereas the SmA microdroplets remain intact after the stress is removed. We did not observe any diffusion of liquid crystal or dye molecules across the interface except in the isotropic phase. In addition, there is no sedimentation of microdroplets and also no noticeable change in the diameter of the microdroplets is observed across the phase transitions. Thus, SmA microdroplets in Cytop-solution are chemically stable and mechanically robust than N and SmC microdroplets. Figure 5.1 (a-c) shows the POM micrographs and corresponding λ -plate (530 nm) images of the microdroplets. Four intensity extinction brushes and a hedgehog point defect at the centre indicates that the director is radial (homeotropic) to the interface. This also means that the smectic layers are concentric in both the SmA and SmC

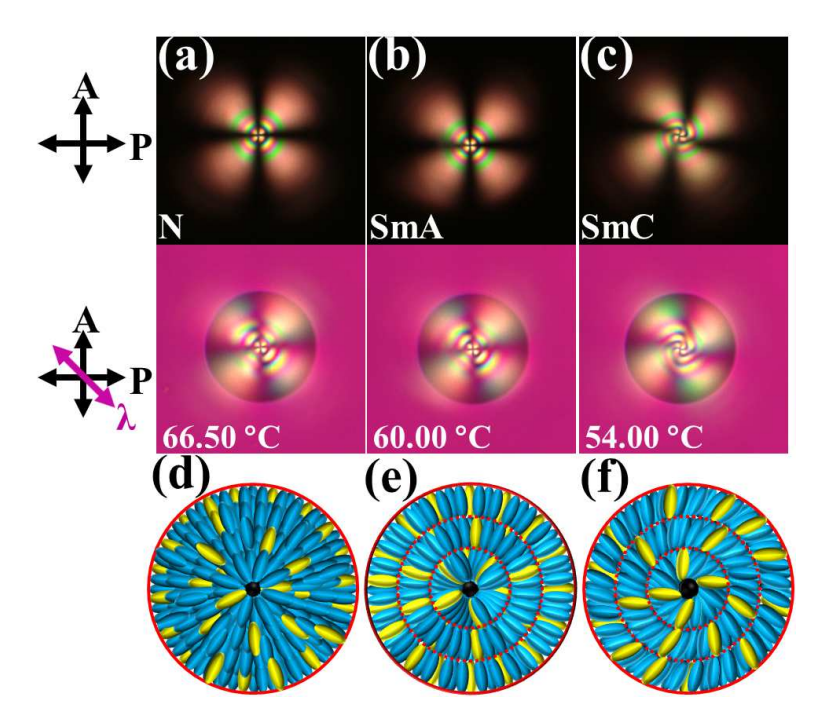


FIGURE 5.1: (a-c) Polarizing optical micrographs (POM) of a microdroplet of diameter 14.5 μ m in the N, SmA and SmC phases. λ -plate images of the respective microdroplets are shown underneath. Temperatures of the microdroplets are shown on the λ -plate images. Crossed polarisers and λ -plate orientation are shown on the left side. (d-f) Schematic director profiles in N, SmA and SmC microdroplets. Yellow ellipsoids represent Nile red dye molecules (doped).

microdroplets as shown schematically in the figures 5.1 (e-f). We noticed that the radial anchoring is partially broken close to the SmC to Cr. phase transition (33.2°C) and eventually no lasing is observed. Hence, the experiments on the SmC microdroplets are performed just 5°C below the SmA-SmC phase transition (which is about 20°C above the SmC to Cr. phase transition temperature).

In SmC microdroplet (Figure 5.1(c)), the extinction brushes rotate clockwise due to the collective tilting of the molecules in the layers. We have measured the approximate tilt angle (θ) from the POM textures at different temperatures below the SmA-SmC phase transition. Figure 5.2(a) shows that the tilt angle increases gradually from $\theta = 0^{\circ}$ to about $\theta = 18^{\circ}$ as the temperature is decreased from 58 °C to 53 °C. We also measured the birefringence (Δn) of the sample using a phase modulation technique [17-19]. Figure 5.2(b) shows that Δn increases with decreasing temperature and changes slope discontinuously at the I-N and N-SmA phase transitions. A small but measurable change in Δn is also observed across the SmA-SmC phase transition temperature.

In what follows, we investigate the WGM lasing of the mesomorphic microdroplets. For this purpose about 0.7wt% Nile Red dye was dissolved in the isotropic phase of the liquid crystal before dispersing it in the Cytop solution to form microdroplets. We choose

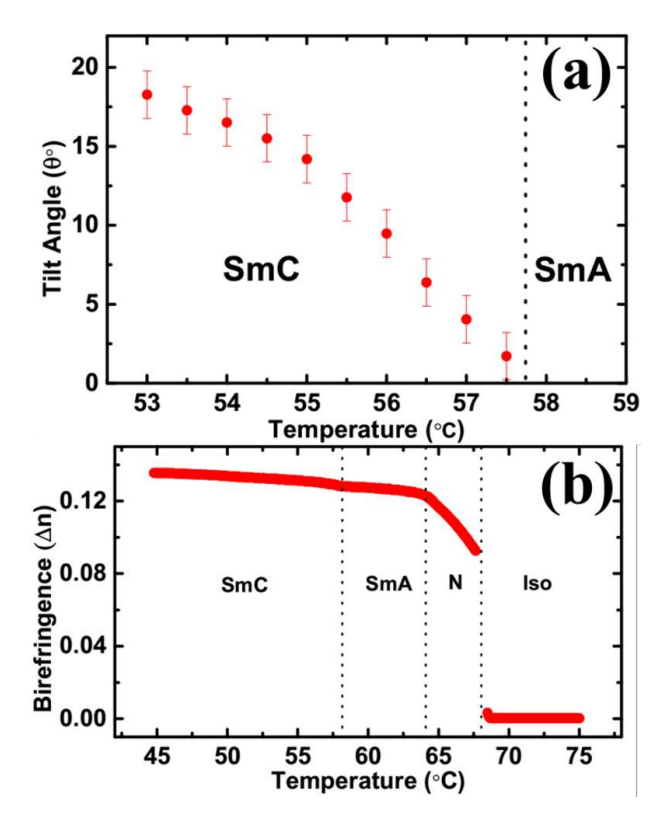


FIGURE 5.2: (a) Temperature dependent tilt angle (θ) measured from the texture of a SmC microdroplet of diameter $33\mu m$. (b) Temperature dependent birefringence (Δn) measured in a planar cell.

an isolated microdroplet and illuminate its edge with the tightly focused laser beam to induce fluorescence. The emitted light is coupled and circulates within the microdroplets due to the total internal reflection, consequently the WGMs are excited. A representative spectrum of a typical WGM resonance (below the lasing threshold pump energy) from a microdroplet of diameter 10μ m is shown in Figure 5.3. When the pumping energy exceeds a certain threshold value, some of the modes start lasing. Figures 5.4(a-c)

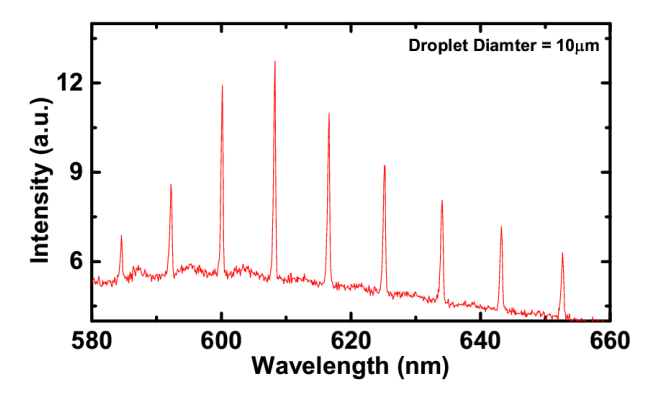


FIGURE 5.3: A typical WGM spectra at a pumping energy of 20 nJ (below the lasing threshold) from a SmA microdroplet of diameter $10\mu m$.

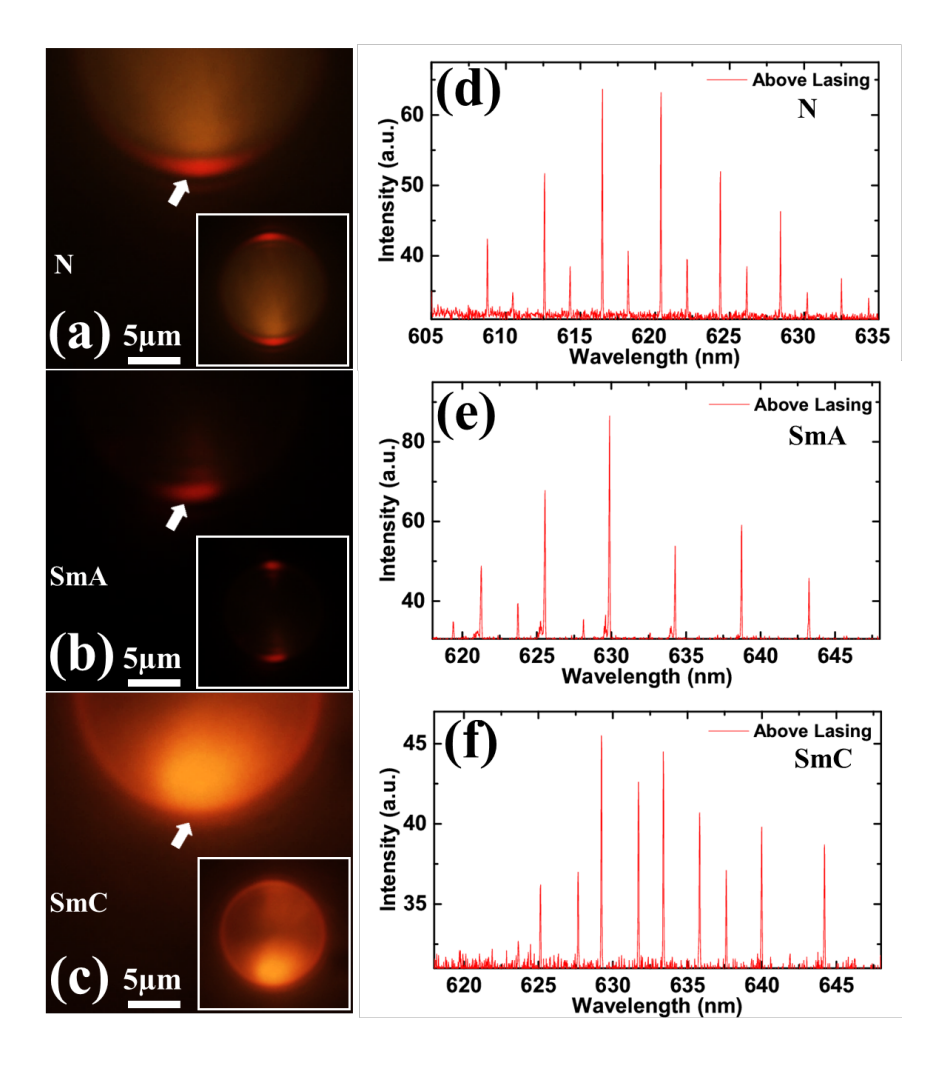


FIGURE 5.4: (a-c) Fluorescence images of illuminated edges of N, SmA and SmC microdroplets with pump energy of 115 nJ. Insets of images (a), (b) and (c) show the respective emission patterns of the whole microdroplets. The N, SmA and SmC microdroplet diameters are 21, 22 and 22.4 μ m respectively. (d-f) Emission spectrum from the respective microdroplets. White arrows indicate the excitation edges of the microdroplets.

show fluorescence images of microdroplets (diameter > 20μ m) illuminated by pumping energies much above the lasing threshold values. In each microdroplet, we see a brighter light spot on the diametrically opposite side of the excited edge and a thin ring of light within the microdroplet circumference, suggesting the WGM excitation. In addition, a speckle formation is also observed above the lasing threshold pump energy, suggesting the emitted light is coherent. It is observed that at the illumination point which is just inside the interface, the scattering of light from the SmC microdroplets is comparatively larger than that of N and SmA microdroplets (inset to Fig.5.4(c)). The emission spectrum of the respective microdroplets in the lasing regime are also shown in Figs. 5.4(d-f). It may be noted that the linewidths (FWHM) of the laser lines are much narrower than that of the WGM resonance (Fig. 5.3). The cavity quality factor of a resonator is given

by $Q = \lambda/\Delta\lambda$, where $\Delta\lambda$ is the full-width at half maxima. The quality factor above the lasing threshold pump energy for a fixed droplet size is found to be $Q \sim 10^4$. Two types of peaks with higher and lower intensities are observed in Figs. 5.4(d-f). They are considered to be TM and TE modes corresponding to the electric field of the light being either parallel or perpendicular to the director. The long axes of the Nile Red molecules and hence the emission transition dipole moments are aligned along the director (yellow ellipsoids in Fig. 5.1(d-f)). Consequently, the TM modes are strongly coupled to the transition dipole moment and have higher intensities than TE modes in N and SmA microdroplets. However, in SmC the situation is complicated because of the molecular tilt. The transition dipole moments have a projection on to the TE modes and as a result TE modes are enhanced and TM modes are reduced as the temperature is decreased across the SmA to SmC transition.

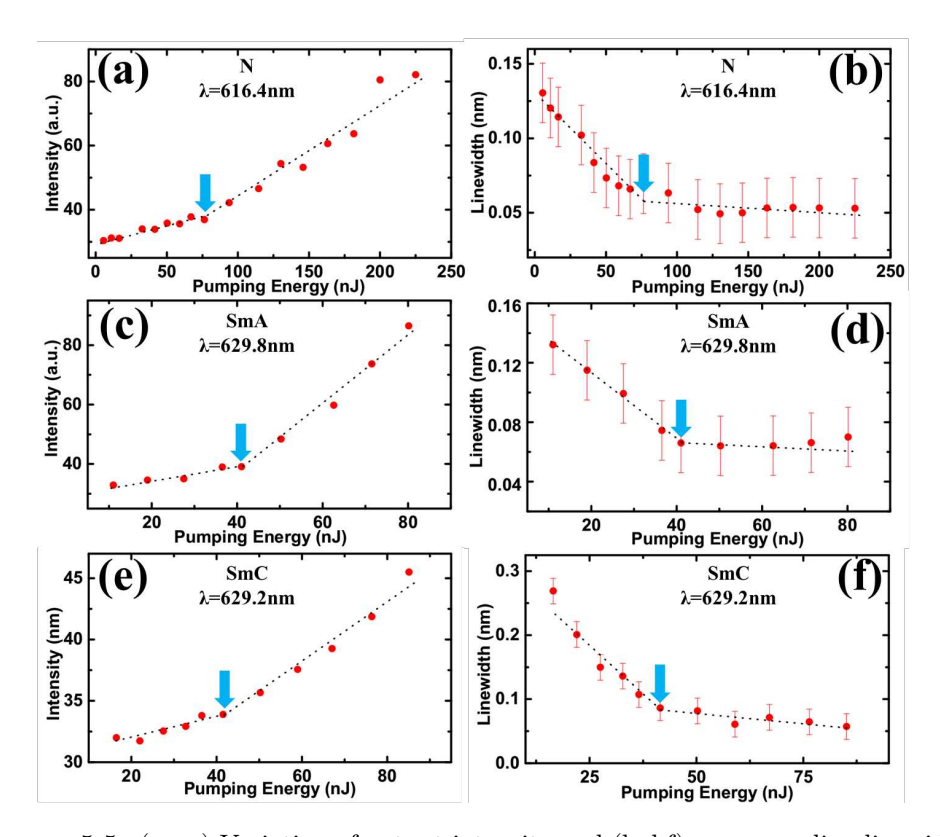


FIGURE 5.5: (a,c,e) Variation of output intensity and (b,d,f) corresponding linewidths as a function of pumping energy. The wavelengths of selected highest intensity modes are 616.4nm, 629.8nm and 629.2nm for the N, SmA and SmC microdroplets respectively. N, SmA and SmC microdroplets' diameters are 21, 22 and 22.4 μ m respectively. Threshold pump energies are marked by arrows. Dotted lines are drawn as guide to the eyes.

To investigate the lasing properties, we analysed the most intense modes in three mesomorphic microdroplets. Figure 5.5 shows the quantitative differences of the lasing characteristics of N, SmA and SmC microdroplets. In all microdroplets, a typical two-slope curve for intensity and linewidth as a function of pumping energy is observed. The

lasing intensity increases and the linewidth decreases with the increasing pump energy. The change of slope occurs at the threshold energy, which suggests the onset of the stimulated emission of the gain medium. During such an emission transition, the gain of the active medium supersedes the optical losses in the microdroplets on account of the attainment of the population inversion between the ground and the excited state energy levels of the dye molecules. In the nematic microdroplet (diameter $21\mu m$), the lasing threshold pump energy for the highest intensity mode (λ =616.4 nm) is 75 nJ (Fig. 5.5(a)). For the SmA and SmC microdroplets (diameter $\simeq 22\mu m$) the threshold energies are almost the same i.e., nearly 42 nJ (Fig.5.5(c,e)). The variation of corresponding linewidths is also shown in Fig.5.5(b,d,f). A clear change of slope is observed at the corresponding threshold pump energies. Figure 5.5(a,c,e) also shows that the lasing intensity from the SmA microdroplet is larger than both the N and SmC microdroplets. For example, at a fixed pump energy of 80 nJ (above the threshold pumping energy) the output intensity of the SmA microdroplet is 55 (a.u) (Fig.5.5(c)), whereas in N and SmC microdroplets it is about 10 (a.u) and 13 (a.u) respectively (Figs. 5.5(a,e)). Thus, intensity of SmA microdroplets is almost 5 times larger than that of the N and SmC microdroplets. In the SmC phase the lasing intensity depends on the tilt angle θ

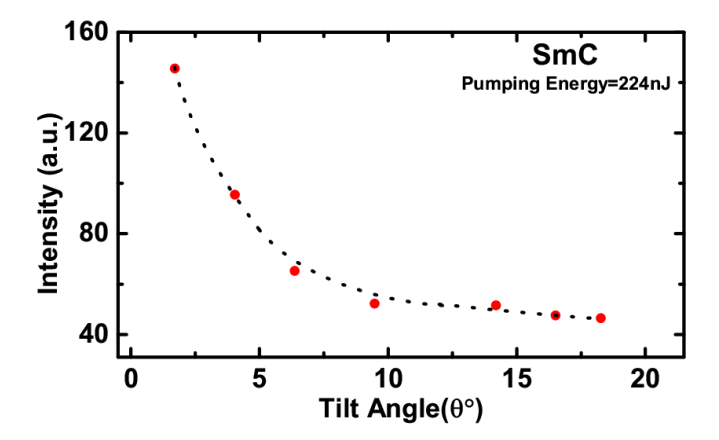


FIGURE 5.6: Variation of lasing intensity of the mode corresponding to emission line $\lambda = 629.2$ nm with tilt angle θ in the SmC phase for a pumping energy of 224 nJ. Dotted line is drawn as a guide to the eye.

as shown in Fig.5.6. The intensity decreases with increasing tilt angle. We also studied the effect of the droplet size on the lasing threshold and the results are shown in Fig.5.7(a). The radiation loss due to the curvature in smaller microdroplets is larger than that of the bigger microdroplets as a result of which the threshold energy decreases with increasing diameter. The lasing threshold pumping energy of the N and SmA decreases faster than the SmC microdroplets. The threshold pump energy of larger SmA microdroplets (diameter $> 25\mu$ m) is smaller compared to both the N and SmC microdroplets. Uniaxial liquid crystals possess extraordinary (n_e) and ordinary (n_o) refractive

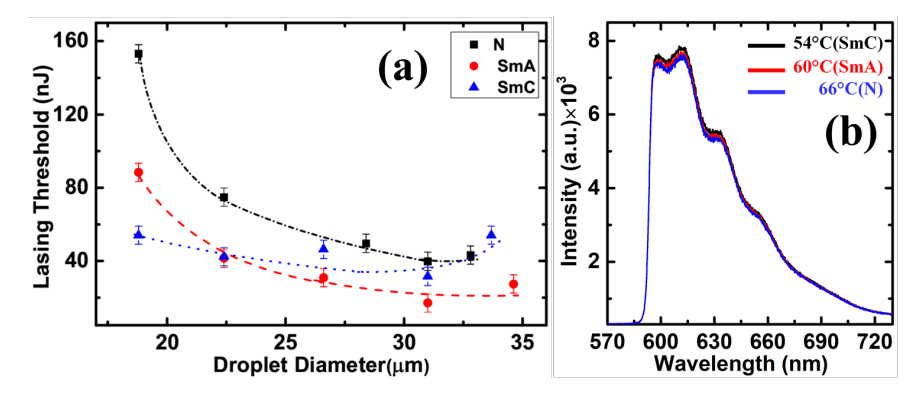


FIGURE 5.7: (a) Dependence of lasing threshold pump energy on microdroplets diameter. Dotted lines are drawn as guide to the eye. (b) Fluorescence intensity measured from a thin film of sample confined between two glass plates at different temperatures. The bandwidth of the excitation filter is 510-560nm. Small oscillations overlaying the emission are due to the finite thickness of the cell.

indices which are temperature dependent and in the calamitic liquid crystals, $n_e > n_o$. In mesomorphic compounds, usually n_e increases and n_o decreases while decreasing the temperature across the N-SmA-SmC phase transitions. Hence, the refractive index difference $(n_e - n_p)$, where n_p is the refractive index of the Cytop-solution) across the SmA-SmC phase transition is increasing. But the SmC phase has monoclinic symmetry and thus weakly biaxial due to the tilting of the molecules in the layer. With decreasing temperature, θ increases and the intensity of TM modes (peaks with higher intensities) decreases. The director fluctuations in the N microdroplets cause scattering losses in the microcavity. In the SmA microdroplets, the fluctuations are suppressed and hence the scattering losses are reduced. Thus, the lower threshold energy and higher lasing intensity of SmA microdroplets could be attributed to the larger refractive index contrast with respect to the Cytop-solution and the lower scattering losses due to the suppression of the director fluctuations. The quantum yield of the fluorescent dye is usually solvent and temperature dependent and this could also contribute to the lasing properties. To see this effect, we have measured the fluorescence intensity from a thin film of the sample confined between two parallel glass plates at different temperatures. However, no noticeable change in the spectrum is observed (Fig. 5.7(b)). Hence, quantum efficiency of the dye is not responsible for the difference in the lasing properties of the mesomorphic microdroplets.

5.4 Conclusion

In summary, we have made a comparative study of the morphology and lasing properties of the N, SmA and the SmC microdroplets dispersed in Cytop-solution. We find that

the SmA microdroplets are chemically stable and mechanically robust compared to the N and the SmC microdroplets. The SmA microdroplets have in general lower lasing threshold pump energy than the N and the SmC microdroplets. The lasing intensity of the SmA microdroplets is almost five times larger than that of the N and the SmC microdroplets. Thus, SmA microdroplets are superior optical microcavities for lasing. The refractive index contrast with respect to the surrounding medium, director fluctuations, orientation of the transition dipole moment of the dye molecules and the director tilt have important contributions on the properties of WGM lasing of the mesomorphic microdroplets. We hope this study will encourage in investigating the unexplored lasing properties of several liquid crystal phases.

Bibliography

- [1] M. Humar, M. Ravnik, S.Pajk and I. Muševič, Nat. Photonics 3, 595 (2009).
- [2] M. Humar, I. Muševič, Opt. Express 18, 26995 (2010).
- [3] M.Humar and I. Muševič, Opt. Express 19, 19836 (2011).
- [4] J. D. Lin, M. H. Hsieh, G. J. Wei, T. S. Mo, S. Y. Huang, C. R. Lee, Opt. Express 21, 15765 (2013).
- [5] M. Humar, Liq. Cryst. 43, 1937 (2016).
- [6] J. A. Sofi and S. Dhara, Appl. Phys. Lett., 114, 091106 (2019).
- [7] K. Vahala, Optical Microcavities, World Scientific, 2004.
- [8] T. Arun Kumar, M. A. Mohiddon, N. Dutta, N. K. Viswanathan, and S. Dhara, Appl. Phys. Lett., 106, 051101 (2015).
- [9] P. V. Shibaev, B. Crooker, M. Manevich and E. Hanelt, Appl. Phys. Lett. 99, 233302(1-3) (2011).
- [10] K. Peddireddy, V. S. R. Jampani, S. Thutupalli, S. Herminghaus, C. Bahr, and I. Muševič, Opt. Express 21, 30233 (2013).
- [11] M. Maruša, J. A. Sofi, I. Kvasic, A. Mertelj, D. Lisjak, V. Niranjan, I. Muševič and S. Dhara, Opt. Express 25, 1073 (2017).
- [12] J. A. Sofi, M. A. Mohiddon, N. Dutta and Surajit Dhara, Phys. Rev. E 96, 022702 (2017).
- [13] J. A. Sofi and S. Dhara, Liq. Cryst., 46, 629 (2019).
- [14] M. Rasi, K.P. Zuhail, A. Roy and S. Dhara, Phys. Rev. E 97, 032702(1-6) (2018).
- [15] A. Kawski, P. Bojarski and B. Kuklinski, Chem. Phys. Lett., 463, 410 (2008).
- [16] M. C. A. Stuart, J. C. Van de Pas, J. B. F. N. Engberts, J. Phys. Org. Chem., 18, 929 (2005).

- [17] P. Sathyanaraya, M. Mathews, Q. Li, V. S. S. Sastry, B. Kundu, K. V. Le, H. Takezoe and S. Dhara, Phys. Rev. E 81, 010702 (2010).
- [18] P. Sathyanarayana, M. C. Varia, A. K. Prajapati, B. Kundu, V. S. S. Sastry and S. Dhara, Phys. Rev. E 82, 050701 (2010).
- [19] P. Sathyanarayana, V. S. R. Jampani, M. Skarabot, I. Muševič, K. V. Le, H. Take-zoe and S. Dhara, Phys. Rev. E 85, 011702 (2012).

Chapter 6

Electrically switchable whispering gallery mode lasing from ferroelectric liquid crystal microdroplets

6.1 Introduction

Whispering gallery mode (WGM) optical resonance have small mode volumes and high quality factors [1-20]. With dye as an active medium, WGM optical resonance emanating from the liquid crystal microdroplets could be used for lasing studies [1,7,11]. Pedireddy et al. has studied lasing in smectic A liquid crystal optical microfibers [21]. We also reported on the magnetic field tuning of lasing in ferromagnetic nematic droplets [7]. Further to the extension, we also explored multimode lasing from nematic, smectic A and Smectic C microdroplets [22]. Among the liquid crystals, the ferroelectric liquid crystals (FLCs) stand outstanding for fast electro-optical applications due to the spontaneous polarisation of the smectic layers. FLCs are specially attractive for the low voltage operability, better optical contrast, bistability and faster electro-optical response [23-32]. At the backdrop of efforts on producing tunable and miniaturised lasers for diverse applications, in this chapter we discuss experimental studies on the electrically switchable lasing from the room temperature ferroelectric liquid crystal microdroplets.

6.2 Experimental

We used a room temperature ferroelectric liquid crystal namely KCFLC7S which was procured from Kingston Chemicals Limited. It is a multi component mixture and exhibits the following phase transitions: Cry. 5°C SmC* 73°C SmA* 100.5°C 114.5°C Iso. Its helical pitch at room temperature is about 2.8 µm. Details about the mixture can be found in the references [25,26]. We used Cytop as a suspending medium owing to its greater stability for LC micrdroplet dispersion. Due to the surface tension and desired anchoring, polydisperse FLC microdroplets with different director dynamics are formed at a fixed elevated temperature of 80°C through modified emulsion method (Sec. 2.4.2 in Chapter 2) [8]. CYTOP has low refractive index (n=1.34) and provides shock free homeotropic alignment of smectic liquid crystals in cells [33-39]. The FLC microdroplets dispersed in the polymer solution were confined in an electro-optic cell with parallel plate electrodes (Sec. 2.2.3, Chapter 2). Before the dispersion, about 0.7 wt% Nile red dye was mixed with the FLC to act as an active medium for the lasing experiments. An isolated dye doped microdroplet of desired size is chosen for lasing study at a time in the experiment. The light emitted from the selected microdroplet is collected by the high resolution spectrometer. A schematic diagram of the cell used in this research work is shown in Fig.6.1(a). The details of the experimental setup is presented in the second chapter of the thesis (Sec. 2.2, Fig. 2.9). For electric field studies, the dc field is provided from a high voltage supply. A λ -plate retarder (530nm) was used to study the optical textures of the different size microdroplets. All the experiments were performed at room temperature.

6.3 Results and discussion

Our study begins with the observation of microdroplets under polarising optical microscope (POM) in the absence of any electric field. Images on the top row of Fig. 6.1 show POM micrographs of a few FLC microdroplets dispersed in CYTOP solution. The images underneath are taken with an additional λ -plate inserted at an angle of 45° with respect to the crossed polarisers. In smaller microdroplets (diameter $\lesssim 5.4\,\mu\text{m}$), four clear brushes are observed suggesting smectic layers are concentric and the layer normal is perpendicular to the interface. Thus CYTOP solution provides homeotropic surface anchoring to the smaller FLC microdroplets. For larger microdroplets (diameter $\gtrsim 5.4\,\mu\text{m}$), the radial structure is not stable and a numeral 8 like defect line is formed near the central region (see λ -plate images in Fig. 6.1(d,e)). With increasing size, the defect appears like a hair pin and evolves from the centre towards the boundary (Fig. 6.1(f,g)). The defect looks somewhat similar to that reported in cholesteric microdroplets, where

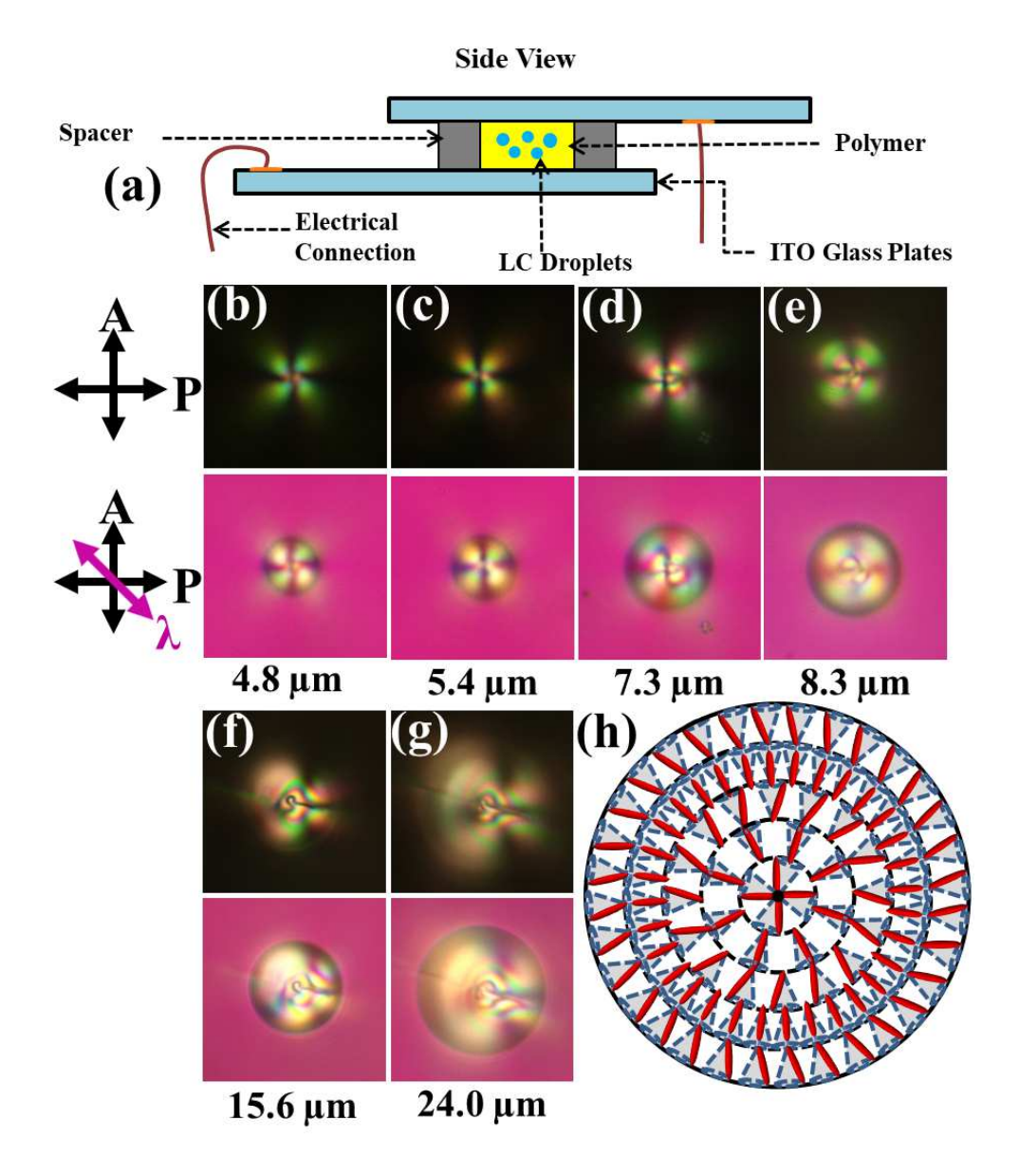


FIGURE 6.1: (a) Schematic diagram of the cell made of two indium-tin-oxide (ITO) coated glass plates. Textures of FLC microdroplets of different diameters. (b-g) Images in the top row show polarising optical micrographs of droplets while the bottom row shows images taken using an additional λ -plate. The orientation of the slow axis of the λ -plate with respect to the crossed polarisers is shown on the left side. (h) Schematic diagram of the cross section of a smaller droplet showing concentric smectic layers with radial helical axis. The red ellipsoids represent molecules within the cone rotating along the helical axis.

two cores of +1 disclination lines forming a double helix structure are fusing together in the center of the microdroplets and appears as hair pin [40-45]. The λ -plate images suggest that the textures of the larger FLC microdroplets are very complex. The equilibrium microdroplet structure results from the competition between the elastic forces that determines the layer orientation of the FLC in the bulk and the surface anchoring, which becomes dominant when the FLC is confined. For smaller microdroplets, the surface

energy dominates and the radial structure becomes stable (Fig. 6.1(b,c)). A schematic diagram of the cross section of a microdroplet with concentric smectic layers is shown in Fig.6.1(h). The molecules rotate in the layers along the helical axis that is orientated radially. The defect in the bigger FLC microdroplets is due to the geometric frustration of chiral ordering and similar to that is observed in cholesteric microdroplets, which essentially depends on the ratio of the pitch and the diameters of the microdroplets.

In what follows, we study the WGM resonance and lasing of the microdroplets under the excitation of the pulsed laser. Although smaller FLC microdroplets appear radial and uniform, no WGM resonance is observed when the microdroplet diameter is lesser than about 8 µm. This is presumably due to the dominant curvature losses that results from the unfulfilled requirement of the critical angle for light to travel through the total internal reflection. Bigger FLC microdroplets exhibit many modes and are often indistinguishable. Hence, in order to avoid the crowding of many modes we confined our studies on isolated FLC microdroplets with diameters in the range of 20-30 µm. Fig-

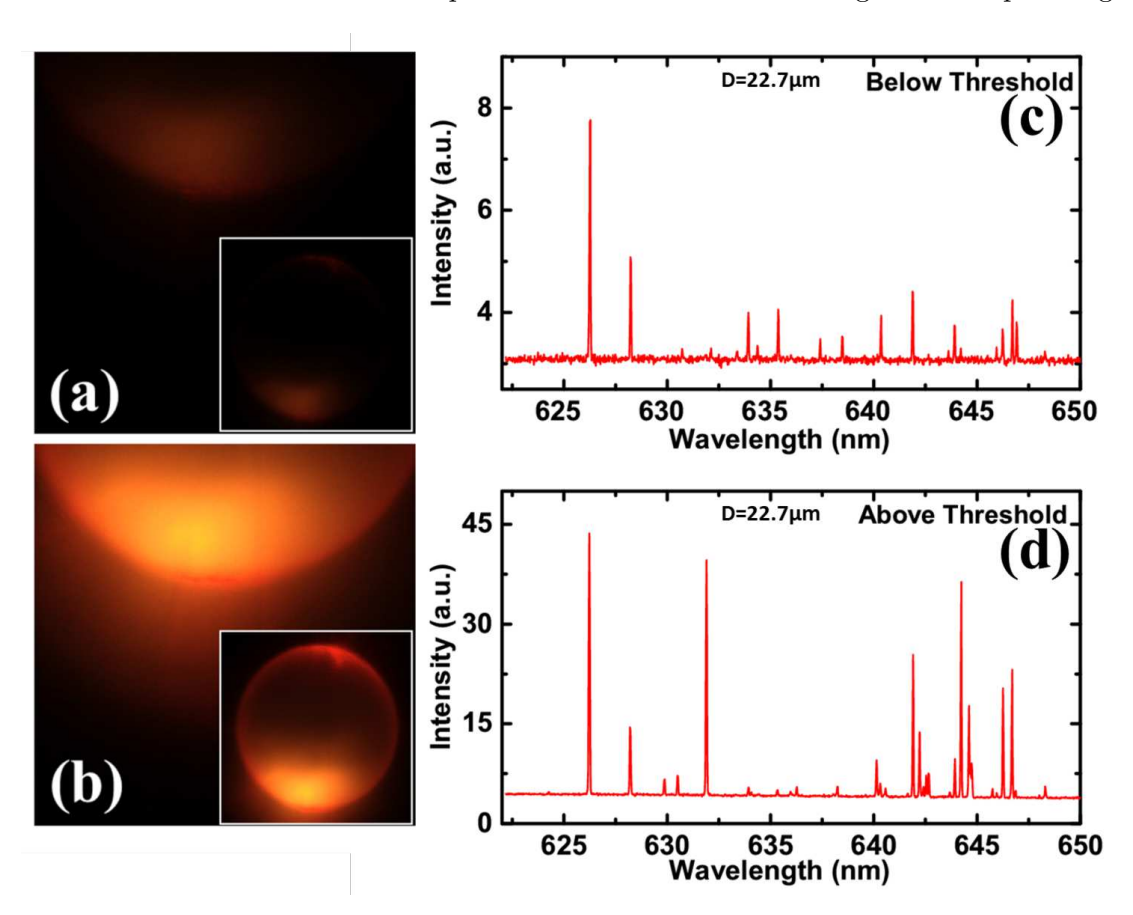


FIGURE 6.2: WGM lasing of a Nile red dye doped FLC microdroplet of diameter, D =22.7 µm. Fluorescence images of the emission pattern at the microdroplet edge (a) at input energy of 5nJ (below lasing threshold energy, discussed later) and at (b) 60nJ (above lasing threshold energy). (c) Typical WGM spectrum below threshold energy. (d)Corresponding spectrum above the lasing threshold energy. The insets show the whole images of the two illuminated microdroplets.

ure 6.2(a) shows the fluorescence image of an isolated droplet of diameter 22.7 µm when pumped by the pulsed laser of energy 5 nJ. A faint light ring is observed surrounding the microdroplet, suggesting the excitation of WGMs. Corresponding spectra is presented in the Fig.6.2(c). It is observed that the WGM spectrum of FLC is significantly different than usually observed spectrum in case of nematic or smectic-A LC microdroplets [2,6,8]. The modes have lower linewidth and are not equally spaced. This is attributed to the inhomogeneity in the refractive index of the cavity that occurs due to the complex elastic deformation of the smectic layers. When the pump energy is increased sufficiently, we observe a clear bright ring with speckle formation (see Fig. 6.2(b)). Corresponding spectra is also shown in Fig. 6.2(d). It is noted that the peak intensities of the modes are increased significantly and some new modes are also visible. For example, the intensity of the dominant mode occurring at $\lambda = 626.27$ nm, is increased from 7.8 to 44 (a.u.) when the pump energy is increased to 60nJ. The speckle formation at the edge of the microdroplets is an indication of coherent light emission in the microcavity [7].

To characterise the WGM spectrum, we measured the output intensity as well as the line-width of the modes as a function of input energy of a microdroplet of diameter $D=23.8\,\mu\text{m}$.

Figure 6.3(a) shows that there is a clear threshold at 22nJ, beyond which the output intensity of the mode ($\lambda = 626.3$ nm) increases linearly. Figure 6.3(b) shows that the linewidth of the same mode decreases and becomes constant at the same threshold input energy. The threshold pump energy and line-width narrowing are important characteristics of laser emission. It is noticed that the threshold energy of the FLC is much smaller than the typical threshold values of the nematic and the cholesteric liquid crystal microdroplets of comparable size and dye concentration. For example, the threshold pump energies for ferromagnetic nematic and cholesteric microdroplets are about 7 to 8 times higher than that of the FLC microdroplets studied in this experiment [4,7]. The linewidth of the lasing in FLC microdroplets is close to 0.06nm and this is smaller compared to that reported (about 0.1nm) in the two referred systems. These are attributed to the absence of strong director fluctuations in the FLC and also to the low absorption of light by the FLC compared to the nematic and the cholesteric liquid crystals. Threshold pump energy also depends on the refractive index of the liquid crystals and the quantum yield of the dye, which depends on the medium, hence it may be more appropriate to compare the threshold values in liquid crystals having the same refractive index.

As a next step, we studied the effect of dc electric field on the morphology and lasing

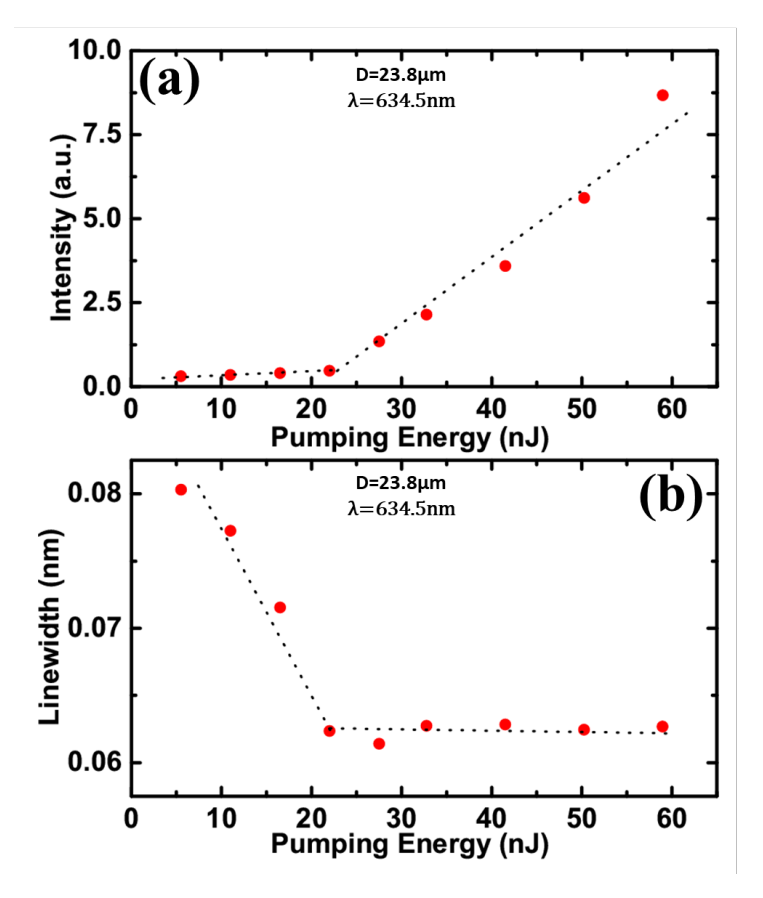


FIGURE 6.3: (a) Intensity of a WGM peak ($\lambda = 634.5$ nm) as a function of the input energy. A typical 2-slope lasing curve is observed. The dotted lines are added as guides to the eye showing lasing threshold at 22 nJ (b) Linewidth of the corresponding spectral peak as a function of input-pulse energy showing reduction to the linewidth below the threshold energy. Droplet diameter, $D=23.8\,\mu\mathrm{m}$.

of the FLC microdroplets. Figure 6.4 shows a sequence of POM micrographs and corresponding λ -plate images with increasing electric field strength. The field is applied between two confining electrodes along the viewing direction. The textures of the FLC microdroplets due to the applied field is very complex and harder to figure out. However, it is evident that the spontaneous electric polarisation of the layer is coupled to the external electric field and consequently the helix should unwind. The unwinding of helix in the confined FLC microdroplets is expected to deform the smectic layer orientation, which can increase the inhomogeneity of the refractive index. Figure 6.5(a) shows the effect of electric field on the lasing spectrum from an FLC microdroplet of diameter, D=20.1 µm. The experiments were conducted at a fixed pumping energy of 60nJ, which is much above the lasing threshold. Only a few lasing modes are observed and corresponding intensities decrease with increasing field. The mode corresponding to the wavelength of λ = 615.8nm is dominant compared to others. The intensity of this mode is shown as a function of field in Fig. 6.5(b). It decreases almost linearly upto a field of 0.12V/ μ m and reaches to a constant value by changing the slope and eventually

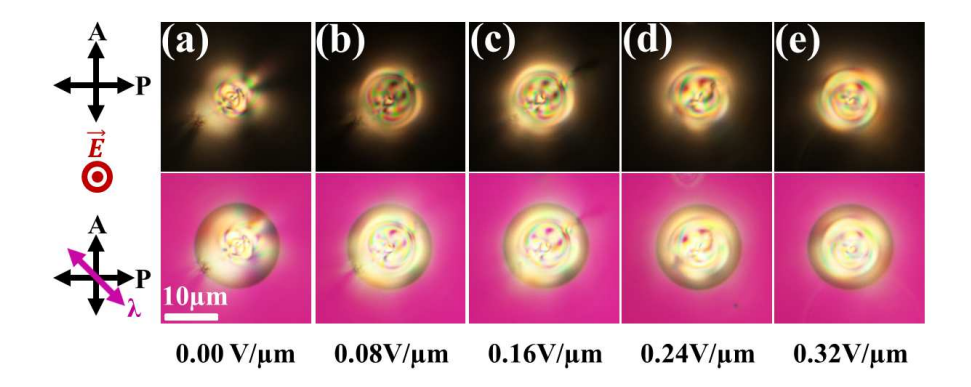


FIGURE 6.4: Textures of an FLC microdroplet of diameter, $D=15.3\mu\mathrm{m}$ at various applied dc electric field strength. Corresponding λ -plate images are shown underneath. The field direction is out of the plane.

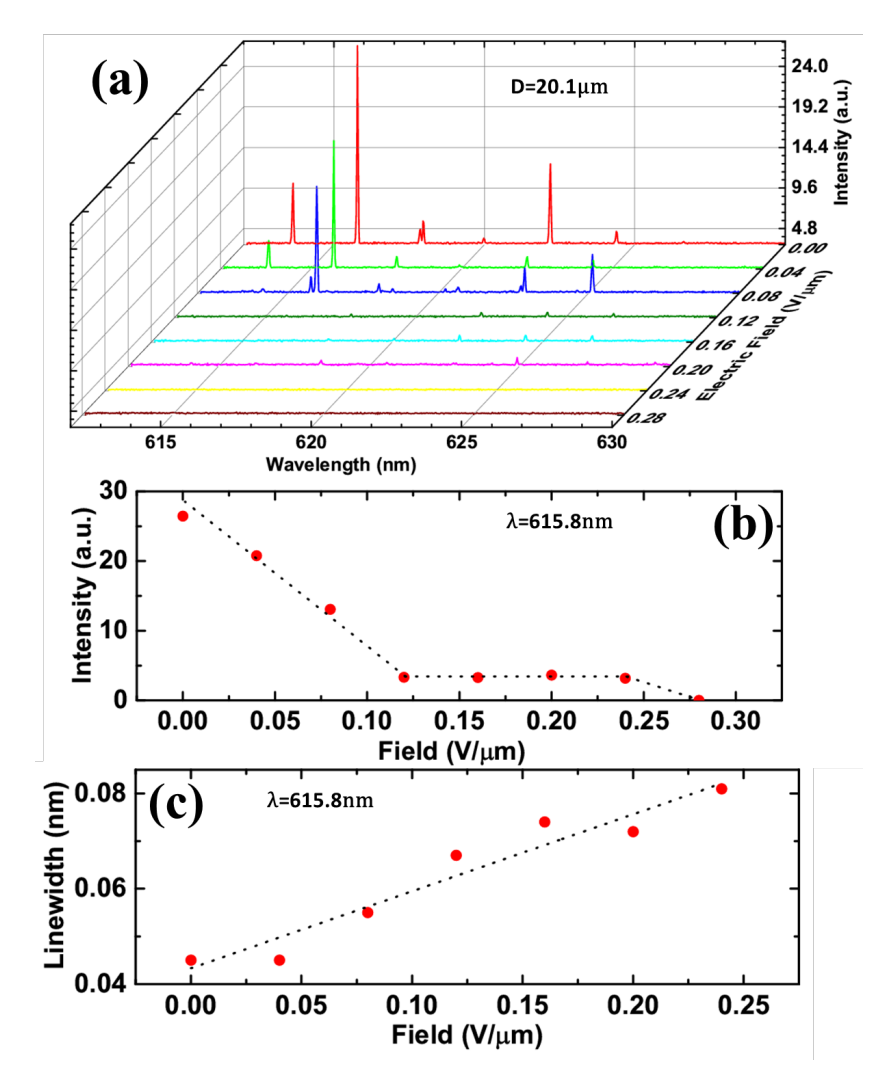


FIGURE 6.5: (a) Effect of dc electric field on the spectrum from an FLC microdroplet of diameter D=20.1 µm. The intensity of the modes is decreasing with increasing field. (b) Variation of emitted intensity corresponding to the dominant mode at $\lambda = 615.8$ nm and (c) linewidth as a function of field strength. The dotted line is drawn as a guide to the eyes.

becomes zero beyond $0.28\mathrm{V}/\mu\mathrm{m}$. The lasing resumes again when the applied field is reduced to zero. The slope change at $0.12\mathrm{V}/\mu\mathrm{m}$ indicates that the lasing is switched off at this field but the WGM modes are still present and eventually disappears beyond $0.28\mathrm{V}/\mu\mathrm{m}$.

For most of the FLC microdroplets with diameters in the range 15-30 µm, the lasing is completely switched off within $0.3V/\mu m$. This is in contrast to the effect of electric field on WGMs observed in the nematic LC microdroplets wherein the modes survive at all fields but shifts towards the lower wavelength with increasing field [2,8]. The switching off lasing from the FLC microdroplets could be attributed to the significant optical energy loss due to the increased inhomogeneity of the refractive index, which occurs due to the enhanced deformation of the smectic layers as observed in Fig.6.4. To get a qualitative notion of the stated phenomenon, we looked at the corresponding effect on the line-width of the lasing of the same mode. It is noticed that the linewidth of the corresponding mode increases almost linearly with the applied field (Fig. 6.5(c)). This confirms that the energy loss in the FLC microcavity increases with the applied field strength.

6.4 Conclusion

In conclusion, we studied WGM lasing from ferroelectric liquid crystal microdroplets at an ambient temperature. The equilibrium structure of the FLC microdroplets is size dependent. In smaller microdroplets, the smectic layers are concentric and almost free from elastic distortions but such microdroplets do not exhibit any WGM resonance. All the bigger FLC microdroplets possess defect loops and the overall structure is complex. As a result the refractive index becomes inhomogeneous. The input threshold pump energy for the WGM lasing of FLC microdroplets is 7 to 8 times lower than that of the nematic and cholesteric LC microdroplets. The external electric field enhances the inhomogeneity of the refractive index further and consequently the optical energy loss in the FLC optical microcavity increases and eventually switches off the lasing. FLC microdroplets could be used as electrically switchable microlaser source in photonic soft-chips. FLC microdroplets could also be used as three-dimensional switchable Bragg type microresonators for omnidirectional lasing, but it is challenging to obtain perfectly radial orientation of the helical axis.

Bibliography

- [1] Kerry Vahala, Optical Microcavities, World Scientific (2004).
- [2] M. Humar, M. Ravnik, S. Pajk and I. Musevic, Nat. Photon., 3, 595 (2009).
- [3] M. Humar and I. Musevic, Opt. Express 19, 19836 (2011).
- [4] M. Humar and I. Musevic, Opt. Express 18, 26995 (2010).
- [5] T. A. Kumar, M. A. Mohiddon, N. Dutta, N. K. Viswanathan and Surajit Dhara, Appl. Phys. Lett., 106, 051101 (2015).
- [6] J. A. Sofi, M. A. Mohiddon, N. Dutta and Surajit Dhara, Phys. Rev. E 96, 022702 (2017).
- [7] M. Marusa, J. A. Sofi, I. Kvasic, A. Mertelj, D. Lisjak, V. Niranjan, I. Musevic and Surajit Dhara, Opt. Express 25, 1073 (2017).
- [8] J. A. Sofi and Surajit Dhara, Liq. Cryst., 46, 629-639 (2019).
- [9] A. Giorgini, S. Avino, P. Malara, P. De Natale and G. Gagliardi, Sci. Rep. 7, 41997 (2017).
- [10] V. S. R. Jampani, M. Humar, I. Musevic, Opt. Express, 21, 20506 (2013).
- [11] M. Humar, Liq. Cryst., 43, 1937 (2016).
- [12] I. Musevic, M. Skarabot and M. Humar, J. Phys. Condens Matter., 23, 284112 (2011).
- [13] C. R. Lee, J. D. Lin, B. Y. Huang, T. S. Mo and S. Y. Huang, Opt. Express, 18, 25896 (2010).
- [14] J. D. Lin, M. H. Hsiegh, G. J. Wei, T. S. Mo, S. Y. Huang and C. R. Lee, Opt. Express, 21, 15765 (2013).
- [15] P. V. Shibaev, B. Crooker, M. Manevich and E. Hanelt, Appl. Phys. Lett., 99, 233302 (2011).

- [16] S. Shivakumar, K. L. Wark, J. K. Gupta, N. L. Abbott, F. Caruso, Adv. Funct. Mater, 19, 2260 (2009).
- [17] S. J. Woltman, G. D. Jay, G. P. Crawford, Nat Mater. 6, 929 (2007).
- [18] I. H. Lin, D. S. Miller, P. J. Bertics, C. J. Murphy, J. J. de Pablo and N. L. Abbott, Science, 332, 1297 (2011).
- [19] D. S. Miller and N. L. Abbott, Soft Matter 9, 374 (2013).
- [20] M. Khan, A. R. Khan, J. H. Shin, S. Y. Park, Sci. Rep., 6, 22676 (2016).
- [21] K. Peddireddy, V. S. R. Jampani, S. Thutupalli, S. Herminghaus, C. Bahr, and I. Muševič, Opt. Express 21, 30233 (2013).
- [22] J. A. Sofi, A. Barthakur and S. Dhara, Soft Matter 15, 7832 (2019).
- [23] M. Hird, Liq. Cryst., 38, 1467 (2011).
- [24] S. T. Lagerwall, Ferroelectric and Antiferroelectric Liquid Crystals, Wiley-VCH Verlag GmbH, Weinheim, Germany (1999).
- [25] T. Joshi, A. Kumar, J. Prakash and A. M. Biradar, Liq. Cryst., 37, 1433 (2010).
- [26] A. Kumar, G. Singh, T. Joshi, G. K. Rao, A. K. Singh and A. M. Biradar, Appl. Phys. Lett., 100, 054102 (2012).
- [27] V. G. Chigrinov, A. K. Srivastava and E. P. Pozhidaev, Journal of the SID, 23(6), 253 (2015).
- [28] S. J. Elston, J. Mod. Opt., **42**, 19 (1995).
- [29] J. Y. Liu and K. M. Johnson, IEEE Photonics Technol. Lett., 7, 1309 (1995).
- [30] A. L. Andreev, Y. P. Bobylev, N. A. Gubasaryan, I. N. Kompanets, E. P. Pozhidaev, T. B. Fedosenkova, V. M. Shoshin and Y. P. Shumkina, J. Opt. Technol., 72, 701 (2005).
- [31] S. T. Lagerwall, Ferroelectrics, **301**, 15 (2004).
- [32] C. Bahr, Ferroelectric Properties and Electroclinic Effect, Springer, New York (2001).
- [33] Surajit Dhara, J. K. Kim, S. M. Jeong, R. Kogo, F. Araoka, K. Ishikawa and H. Takezoe, Phys. Rev. E 79, 060701 (2009).
- [34] S. M. Jeong, Y. Shimbo, F. Araoka, Surajit Dhara, N. Y. Ha, K. Ishikawa and H. Takezoe, Adv. Mater., 22, 34 (2010).

- [35] D. Venkata Sai, T. Arun Kumar, Arun Roy, W. Haase and Surajit Dhara, J. Chem. Phys., 141, 044706 (2014).
- [36] T. Arun Kumar, P. Sathyanarayana, V. S. S. Sastry, H. Takezoe, N. V. Madhusu-dana and Surajit Dhara, Phys. Rev. E 82, 011701 (2010).
- [37] T. A. Kumar, Khoa V. Le, S. Aya, K. Fukuda, F. Araoka, K. Ishikawa, J. Watanabe, S. Dhara, and H. Takezoe, Phase Transitions 85, 888 (2012).
- [38] T. Arun Kumar, V. S. S. Sastry, K. Ishikawa, H. Takezoe, N.V. Madhusudana and Surajit Dhara, Liq. Cryst., 38, 971 (2011).
- [39] J. K. Kim, S. M. Jeong, Surajit Dhara, F. Araoka, K. Ishikawa and H. Takezoe, Appl. Phys. Lett., 95, 063505 (2009).
- [40] T. Orlova, S. J. Abhoff, T. Yamaguchi, N. Katsonis and E. Brasselet, Nat. Commun., 6, 7603 (2015).
- [41] G. Posnjak, S. Copar and I. Musevic, Nat. Commun., 8, 14594 (2017).
- [42] E. Bukusoglu, X. Wang, Y. Zhou, J. A. Martinez-Gonzalez, M. Rahimi, Q. Wang, J. J. de Pablo and N. L. Abbott, Soft Matter 12, 8781 (2016).
- [43] Y Zhou, E. Bukusoglu, J. A. Martinez-Gonzalez, M. Rahimi, T. F. Roberts, R. Zhang, X. Wang, N. L. Abbott and J. J. de Pablo, ACS Nano., 10, 6484 (2016).
- [44] D. Sec, T. Porenta, M. Ravnik and S. Zumer, Soft Matter 8, 11982 (2012).
- [45] O. O. Prishchepa, V. Ya. Zyryanov, A. P. Gardymova and V. F. Shabanov, Mol. Cryst. Liq. Cryst., 489, 84 (2008).

Chapter 7

Summary and outlook

7.1 Aim and overview of thesis

In the introductory chapter, we presented a brief discussion on some liquid crystalline phases and their physical properties. Next, we described the relevant properties of optical resonators. Towards the end of the chapter, we worked out the theoretical background of solutions to the whispering gallery mode waves circulating within an isotropic and anisotopic sphere. We concluded the chapter with the theory of lasing [1–5]. In the second chapter, we discussed various experimental techniques that have been employed for performing different types of experiments. To begin with, different types of cell preparation were discussed alongside their fabrication and usage. All the processes involving cell preparation, dye doping of the liquid crystal compound, sample preparation, optical polarizing microscopy analysis and optimization of laser optics and laser energy were discussed in detail [6, 7].

In the third chapter, we presented the experimental findings on electrical and thermal tuning of quality factor and free spectral range of whispering gallery mode optical resonance in the spherical liquid crystal microdroplets, suspended in polydimethyl silohexanne (PDMS). Next we discussed the effect of temperature and electric field on the whispering gallery mode optical resonance respectively. Finally, the effect of the LC microdroplet size reduction on the optical resonance properties was highlighted and accordingly the need for the suitable dispersing medium was realised [8].

In the fourth chapter, we reported on several dispersing media for suspending stable LC microdroplets at room temperature. The anchoring feature and the longevity of the LC microdroplets were studied in many mediums. The relative merits and demerits of each suspending medium were discussed and it was concluded that Cytop solution is one

of the best media for a stable dispersion of LC microdroplets. Next, the free spectral range of the WGMs of the various sized microdroplets made from a negative dielectric anisotropy liquid crystal compound was studied. Towards the end of that chapter, we finally discussed the effect of electric field on the free spectral range and the Q-factor of the WGM optical resonance. It was observed that for negative dielectric anisotropy liquid crystal both the Q-factor and FSR do not change considerably with respect to the change of the externally applied electric field [9].

In the fifth chapter of the thesis, we reported on the WGM lasing across multiple mesophases. In that comparative study, an attempt was made to bring out the relative merits and demerits of WGM lasing in the mesomorphic microdroplets of a pyridine derivative liquid crystal compound. Under a mild mechanical stress, it was found that among the nematic, Smectic A and Smectic C mesophase LC microdroplets, the Smectic A LC microdroplets are mechanically more robust than the other mesophases. Next, WGM lasing occurrence was studied from the mesomorphic LC microdroplets and was subsequently confirmed from the out put intensity and linewidth of the most emission lines. Lastly, from the lasing threshold comparisons, the Smectic A LC microdroplets were found to incur low lasing threshold with higher intensity and thus merits as a better optical microcavity. The experimental results were discussed based on the orientation dipole moment of the dye molecules, director fluctuations and tilting of the director at the interface [10].

In the sixth chapter, we reported on the electrically switchable whispering gallery mode lasing from room temperature ferroelectric liquid crystal (FLC) microdroplets. We first discussed on the complex morphology of FLC microdroplets with increasing size. In order to envisage WGM lasing, the FLC microdroplets were excited with a suitable pulsed laser beam. It was found that as the pumping energy is increased, the dye doped FLC microdroplets started to emit multimode laser light beyond certain threshold value. Further to the confirmation, the qualitative analysis revealed that, for most of the modes, the emitted intensity started increasing while the linewidth started decreasing rapidly after specific pumping energies. The change in slope occurring at the threshold input energy suggests that the population inversion is achieved within the microdroplet and thus marking the onset of the stimulated emission. It was found that the lasing threshold pump energy of FLC microdroplets is much smaller than that of the nematic and cholesteric microdroplets. Towards the end of the chapter, we demonstrated that for a particular lasing mode with the increasing electric field, the linewidth increases while the lasing intensity decreases and eventually switches off beyond a particular field [11].

The last chapter of the thesis is devoted in summarizing the main experimental findings of the thesis. Finally, we put forward some more innovative ideas that could be worked out as an extension to this thesis.

7.2 Future outlook

With increasing demands of miniaturization of optical circuits, the whispering gallery mode optical resonance based optical micro components could pave the way forward to the photonic technology. In this regard, the following ideas could be explored:

7.2.1 Fabrication of micro biolasers

Many soft living tissues from plants and animals could be studied for whispering gallery mode optical resonance phenomenon. Spherical biological optical microcavities could easily be incorporated into living tissues owing to their specific compatibility with the tissues for various purposes like disease detection. In addition, these soft living tissues based optical microresonators could be used as biological lasers and could very easily find their place in the soft photonic circuits. Such optical microcavities are cheaply available and are biodegradable [4].

7.2.2 Unknown promise of mesomorphic liquid crystal phases

Liquid crystalline phase is exhibited by many compounds with different shape mesogens. We devoted our whole thesis work on liquid crystal microdroplets formed by calamitic shape molecules. However, liquid crystals made up other mesogens like disc shape molecules, banana shaped molecules, hockey shaped molecules, etc. could be used for WGM studies and to fabricate new class of spherical optical microresonators. We anticipate that those optical microresonators may yield new optical properties [1, 12–16].

7.2.3 Diversifying optical microcavity structure

The soft biological materials could be used to form different morphology optical microcavities. For instance, fibers, rings, discs, etc. could be formed and studied for new optical properties. Similarly different liquid crystalline phases made of various mesogen shapes could be used to fabricate various morphology optical microcavities like microfibers, microrings, microshells, etc. Depending upon the type of microresonator

needed in the optical circuits, such different morphologies may fit and serve the requisite options [4, 17].

Bibliography

- [1] P. J. Collings and M. Hird, *Introduction to liquid crystals chemistry and physics*, Taylor and Francis, (1997).
- [2] P. G. de Gennes and J. Prost, The Physics of Liquid Crystals, 2nd Ed., Clarendon Press, Oxford, (1993).
- [3] S. Chandrashekhar, *Liquid crystals*, Cambridge University Press, Cambridge, (1992).
- [4] Kerry Vahala, Optical Microcavities, World Scientific (2004).
- [5] Matjaž Humar, Liquid Crystal Microdroplets as Optical Microresonators and Lasers., PhD Dissertation, Jožef Stefan International Postgraduate School Ljubljana, Slovenia, (2012).
- [6] Paladugu Sathyanarayana, Investigation on the Physical Properties of Unconventional Nematic Liquid Crystals., PhD Dissertation, University of Hyderabad, India (2012).
- [7] Zuhail K. P., Topological Defects Transformation and Structural Transition of Two Dimensional Colloidal Crystals across Nematic to Smectic-A Phase transition., PhD Dissertation, University of Hyderabad, India, (2017).
- [8] J. A. Sofi, M. A. Mohiddon, N. Dutta, and S. Dhara, Phys. Rev. E, 96, 022702, 477, (2017).
- [9] J. A. Sofi, and S. Dhara, Liq. Cryst., 46, 4, 629-639, 477, (2018).
- [10] J. A. Sofi, A. Barthakur and S. Dhara, Soft Matter, 15, 7832-7837, (2019).
- [11] J. A. Sofi, and S. Dhara, Appl. Phys. Lett., 114, 091106 (2019).
- [12] P. S. Drzaic, Liquid Crystal Dispersions, World Scientific Publishing: Singapore, (1995).
- [13] J. W. Doane, N. A. Vaz, B.G. Wu and S. Zumer, Appl. Phys. Lett., 48, 269-71, (1986).

- [14] I. Muševič, Liquid Crystal Colloids, Springer: Cham, Switzerland, (2017).
- [15] S. T. Lagerwall, Ferroelectric and Antiferroelectric Liquid Crystals, Wiley-VCH Verlag GmbH, Weinheim, Germany (1999).
- [16] C. Bahr, Ferroelectric Properties and Electroclinic Effect, Springer, New York (2001).
- [17] Bahaa E. A. Saleh and Malvin Carl Teich, Fundamentals of Photonics, John Wiley and Sons, Inc., (1991).

List of publications:

Thesis publications:

- "Electrical and thermal tuning of quality factor and free spectral range of optical resonance of nematic liquid crystal microdroplets", J. A. Sofi, M. A. Mohiddon, N. Dutta, and S. Dhara, Phys. Rev. E 96(2): 022702, 477 (2017).
- "Stability of liquid crystal micro-droplets based optical microresonators",
 J. A. Sofi and S. Dhara, Liq. Cryst. 46, 4, 629-639 (2018).
- 3. "Electrically switchable whispering gallery mode lasing from ferroelectric liquid crystal microdroplets", J. A. Sofi and S. Dhara, Appl. Phys. Lett. 114, 9, 091106 (2019).
- "Whispering gallery mode lasing from mesomorphic liquid crystal microdroplets", J. A. Sofi, A. Barthakur and S. Dhara, Soft Matter. 15, 3832-3837 (2019).

Other publications:

1. "Magnetic field tuning of whispering gallery mode lasing from ferromagnetic nematic liquid crystal microdroplets", M. Mur, J. A. Sofi, I. Kvasić, A. Mertelj, D. Lisjak, V. Niranjan, I. Muševič and S. Dhara, Opt. Express 25, 2, 1073-1083 (2017)

Conferences and workshops attended:

International:

- Attended International Complex Fluids Conferences (Comp-Flu) at IIIT Hyderbad December 2016, Poster presentation.
- Attended International Workshop on Complex Photonics at TIFR Mumbai
 January 2017, Poster presentation.
- Attended 27th International Liquid Crystal Conference (ILCC) at Kyoto,
 Japan July 2018, Poster presentation.
- Attended Photonics Online Meet-up (POM-20) January 2020, Poster Presentation

National:

- Attended Frontiers in physics-2016 at School of Physics, University of Hyderabad, Hyderabad - March 2016, Poster presentation.
- Attended 23rd National Conference on Liquid Crystals (NCLC) at IIT-ISM Dhanabad - December 2016, Poster presentation.
- Attended National Conference on Physics at Small Scales and Advanced Materials at University of Hyderabad, Hyderabad - September 2017, Poster presentation.
- Attended Workshop on Soft and Active Matter at School of Physics, University of Hyderabad, Hyderabad February 2018, Poster presentation.
- Attended National Laser Symposium (NLS-27) at RRCAT Indore December 2018, Poster presentation.
- Attended National Laser Symposium (NLS-28) at VIT Vellore, Chennai, Tamil Nadu January 2020, Poster presentation.

Contact:

Junaid Ahmad Sofi
Soft matter Laboratory,
School of Physics,
University of Hyderabad,
Gachibowli, Hyderabad, India - 500046
Email: coolsofi14@gmail.com

Awards and achievements:

- Qualified **JEST-2010**
- Qualified GATE-2015 with all India rank 132.
- Qualified CSIR-NET in Physics-2017 with All India Rank 42.
- Awarded UGC-BSR \mathbf{JRF} in April 2015.
- Kaleidoscope for August 2017 for Physical Review E journal.
- Awarded UGC-BSR **SRF** in April 2017.
- Awarded Best Poster Award at "National Conference on Physics at Small Scales and Advanced Materials-2017", UoH, Hyderabad.
- Awarded **Best Poster Award** at "National Laser Symposium-27", RRCAT, Indore.
- Awarded ITS Grant by DST-India for ILCC-2018 held in Japan.

References 114

References:

• Prof. Surajit Dhara

School of Physics,

University of Hyderabad, Hyderabad-500046

Email: dharasurajit@gmail.com, sdsp@uohyd.ernet.in

• Prof. B.V.R. Tata

School of Physics,

University of Hyderabad, Hyderabad-500046

 $Email: \ bvrtata@gmail.com, \ bvrtata@uohyd.ac.in$

• Dr. Venkataiah Gorige

School of Physics,

University of Hyderabad, Hyderabad-500046

Email: vgsp@uohyd.ac.in

Whispering Gallery Mode Optical Resonance and Lasing in Liquid Crystal Microdroplets

by Junaid Ahmad Sofi

Submission date: 12-Jun-2020 03:40PM (UTC+0530)

Submission ID: 1342494686

File name: Junaid_PhD_Thesis.pdf (6.66M)

Word count: 25802

Character count: 132387

Saliara

Dr. Surajit Dhara
Professor
School of Physics
University of Hyderabad
Hyderabad-500 046, INDIA.

Whispering Gallery Mode Optical Resonance and Lasing in Liquid Crystal Microdroplets

ORIGINALITY REPORT

37%

SIMILARITY INDEX

INTERNET SOURCES

PUBLICATIONS

STUDENT PAPERS

PRIMARY SOURCES

Junaid Ahmad Sofi, Surajit Dhara. "Stability of liquid crystal micro-droplets based optical microresonators", Liquid Crystals, 2018

Publication

Dr. Surajit Dhara

Junaid Ahmad Sofi, M. A. Mohiddon, N. Dutta University of Hyderabad-500 Surajit Dhara. "Electrical and thermal tuning of quality factor and free spectral range of optical resonance of nematic liquid crystal microdroplets", Physical Review E, 2017 **Publication**

Dr. Surajit Dhara Professor School of Physics University of Hyderabad Hyderabad-500 046, INDIA.

3

Junaid Ahmad Sofi, Abinash Barthakur, Surajit Dhara. "Whispering gallery mode lasing in mesomorphic liquid crystal microdroplets", Soft

Matter, 2019 **Publication**

Dr. Surajit Dhara Professor

School of Physics University of Hyderabad Hyderabad-50

Junaid Ahmad Sofi, Surajit Dhara. "Electrically switchable whispering gallery mode lasing from ferroelectric liquid crystal microdroplets", Applied Physics Letters, 2019

Publication

Professor School of Physics rsity of Hyderabad abad-500 046, INDIA. Dr. Surajit Dhara

Surajit Dhara

Professor School of Physics University of Hyderabad Hyderabad-500 046, INDIA.

Plagiarism-free statement:

This is to certify that the thesis titled "Whispering Gallery Mode Optical Resonance and Lasing in Liquid Crystal Microdroplets" has been screened by the Turnitin software at Indira Gandhi Memorial Library of University of Hyderabad. The software shows 38% similarity index out of which, 33% came from the candidate's own research articles related to this thesis. Thus, the effective similarity index excluding his research articles is 38 - 33% = 5% which is lower than the 10% stipulated by the University guidelines. Therefore, this thesis is free from plagiarism.

Date: 24-06-2020

Prof. Surajit Dhara Thesis Supervisor School of Physics

University of Hyderabad

Dr. Surajit Dhara Professor School of Physics University of Hyderabad Hyderabad-500 046, INDIA.